Atomic Scale Characterization of Semiconductor Non-Planar Nanostructures

María de la Mata Fernández

Supervisor:
Prof. Jordi Arbiol i Cobos
Tutor:
Dr. Xavier Granados García

October 2015

Instituto de Ciencia de Materiales de Barcelona, ICMAB-CSIC

Physics Department of Science Faculty,
Universitat Autònoma de Barcelona

UAB
Universitat Autònoma
de Barcelona

ICMAB CSIC

Jordi Arbiol i Cobos, ICREA Research Professor at Institut Català de Nanociència i Nanotecnologia and **Xavier Granados García**, Tenured Scientist at Institut de Ciència de Materials de Barcelona

CERTIFY

that **María de la Mata Fernández**, MSc in Materials Science and Technology, carried out the work entitled "Atomic Scale Characterization of Semiconductor Non-Planar Nanostructures" under their direction and qualifies for the degree of Doctor in Materials Science. And for that record, sign this certificate.

Prof. Jordi Arbiol i Cobos   Dr. Xavier Granados García   María de la Mata Fernández

Bellaterra, September 2015

Contents

Acknowledgments

Before going into the matter, I would like to devote few words to all the people involved in the development of this PhD, whose invaluable help has made possible the work presented in the following.

First of all, I would like to deeply acknowledge Prof. Jordi Arbiol, my supervisor, for his guidance and advices along this way, for his endless and contagious enthusiasm, and for his support and confidence in me.

Thanks to the whole GAeN group, where I always felt in a comfortable environment. I kindly appreciate the shared knowledge and experiences, and time spent together with Reza, Roger and Aziz, who have already moved to continue their research, and Francisco, always cheerful and willing to help.

During this period, I had the great opportunity of working with Dr. César Mágen, whom with we have collaborated extensively at the INA-LMA. I really appreciate the many hours he has dedicated to teach and guide me in the aberration-corrected microscopy. I would also like to thank Dr. Rodrigo Fernández-Pacheco and Dr. Alfonso Ibarra who have helped me a lot during my stays at the INA-LMA.

I would like to express my gratitude to Dr. Vincenzo Grillo, who warmly received me in his group in Parma and showed me the secrets of his software for the image simulation.

Thanks to Prof. Silvija Gradečak and Dr. Xiang Zhou from MIT, for the nice CL analyses.

I would also like to thank all the technical stuff and people working at the different facilities, for their support, especially from the Electron Microscopy Division at ICN2

Abstract

Semiconductor nanostructures are building blocks with high potential to be integrated in a wide variety of technological devices, in addition to be ideal platforms for the study of fundamental physical principles. Importantly, understanding the formation and behavior of these structures involves their characterization at atomic scale. Knowing the exact atomic arrangements is highly useful in order to face some questions related to the growth mechanisms promoting the formation of different nanostructures, and thus allowing the smart synthesis of materials with the exact sought properties. Along this thesis, we perform detailed atomic characterizations of binary compound (AB) semiconductor non-planar nanostructures, by means of (Scanning) Transmission Electron Microscopy ((S)TEM) techniques, along with computer simulations when needed, focusing on the visualization and identification of individual atomic columns.

By the identification of the atomic constituents within the lattice crystal in the growing structure, we investigate polarity related issues, as the unidirectional polar growth or the polarity preservation/inversion.

The system analyses at atomic scale becomes especially important when more than one material composes the nanostructures, since the matching among phases has a determining role in the system behavior. Mainly depending on the lattice misfit among the connected phases and the shape and size of the nanostructures, the mismatch strain will be released as plastic and/or elastic lattice distortions, affecting differently the performance of the system.

Moreover, the combination of different materials allows the creation of smaller structures within the nanostructures, achieving quantum confinement under a certain threshold size, and known as quantum structures. The final properties of these architectures rely on the number of dimensions spatially confined, in addition to the nature of the

material and their size, requiring accurate atomic characterizations.

These three points are covered along this dissertation. The manuscript structure is the following: the introductory chapter (Chapter 1), giving an overview about semiconductor nanostructures, focused on nanowires, including heterostructures and quantum structures within nanowires, is followed by a chapter describing the methodology employed (Chapter 2) for the analyses performed, i.e., (S)TEM techniques, aberration correction, strain measurements and image simulation and related computing tools. The results presented are divided in four chapters:
- Chapter 3, focused on the polarity issue in binary compound nanowires, and its implications on other related systems (tripods and tetrapods).
- Chapter 4, which also deals with the polarity, but in 2D-like nanostructures.
- In Chapter 5, the relaxation mechanisms of the mismatch strain in heterostructured nanowires are analyzed.
- Chapter 6 addressed the structural and optical characterization of quantum structures within nanostructures.
Finally, Chapter 7 summarizes the main conclusions of the manuscript, along with a brief outlook.

Resumen

Las nanoestructuras semiconductoras son bloques de construcción con gran potencial para ser integrados en numerosos dispositivos tecnológicos, además de ser plataformas ideales para el estudio de principios físicos fundamentales. Para entender la formación y crecimiento se estas estructuras, deben ser caracterizas a nivel atómico. El conocimiento de las disposiciones atómicas exactas es muy útil para poder afrontar algunos interrogantes relacionados con los mecanismos de crecimiento que impulsan la formación de diversas nanoestructuras y permiten, por tanto, la síntesis inteligente de materiales con las propiedades buscadas. En esta tesis se llevan a cabo caracterizaciones atómicas detallas de compuestos semiconductores, AB, sintetizados bajo morfologías nanométricas no planares, a través de técnicas avanzadas de microscopía electrónica de transmisión, (S)TEM, junto con cálculos computacionales cuando se requieren, con especial hincapié en la visualización e identificación de columnas atómicas individuales.

Identificando las especies atómicas y su posición dentro de la red cristalina del material hemos podido investigar temas relacionados con la polaridad, como el crecimiento unidireccional o la preservación / inversión de polaridad en una nanoestructura y sus implicaciones.

El análisis de sistemas a nivel atómico se hace especialmente importante cuando más de un material compone las nanoestructuras, dado que el acoplamiento entre las distintas fases y la intercara creada entre ambos tienen un papel determinante en el comportamiento final del sistema. Dependiendo, principalmente, de los parámetros de red relativos de las fases cristalinas implicadas, y de la forma y tamaño de las nanoestructuras, la tensión generada en los cristales es liberada en forma de distorsiones plásticas y / o elásticas, que afectan de varias maneras el funcionamiento del dispositivo.

Además, combinando diferentes materiales dentro de una misma nanoestructura se pueden crear arquitecturas más pequeñas, que ofrecen confinamiento cuántico bajo un

determinado umbral dimensional, conocidas como estructuras cuánticas. Sus propiedades dependerán del número de dimensiones espacialmente confinadas, así como de su tamaño y naturaleza del material, por lo que deben analizarse cuidadosamente a escala atómica.

A lo largo de esta disertación, cubrimos estos tres temas principales. La estructura del manuscrito es la siguiente: al capítulo introductorio (Capítulo 1), que plantea una visión general sobre las estructuras semiconductoras, especialmente centrado en nanohilos (incluyendo heteroestructuras y estructuras cuánticas); le sigue un capítulo describiendo la metodología empleada en los análisis en los que basamos los resultados (Capítulo 2), es decir, técnicas de (S)TEM, corrección de aberraciones en el microscopio, cómo medir la tensión estructural en las fases cristalinas y una breve explicación de cómo realizados las simulaciones y el empleo de otras herramientas informáticas. Los resultados se presentan divididos en cuatro capítulos:

- El Capítulo 3 se centra en la determinación de la polaridad en nanohilos semiconductors binarios y sus implicaciones en otros sistemas con morfologías relacionadas (trípodes y tetrapodos).

- El Capítulo 4, que también trata de polaridad pero, en esta ocasión en nanostructuras del tipo 2D.

- En el Capítulo 5 se analizan los mecanismos de relajación de la tensión cristalina inducida al combinar distintas fases dentro de nanohilos.

- El Capítulo 6 aborda la caracterización estructural y óptica de estructuras cuánticas dentro de nanoestructuras.

Finalmente, el Capítulo 7 resume las principales conclusiones del manuscrito, junto con algunas perspectiva de futuro.

Introduction: Non-Planar Semiconductor Nanostructures

The advancement of the present technological age has turned semiconductor materials into essential candidates for achieving the sought working properties, pushing the technological performance of the devices to the limits of physics. In addition to covering wide operative ranges, for instance, by tuning their composition, they allow further functionalization by the creation of tiny structures. In this context, the nanostructuration has emerged as a powerful tool, not only for scaling down the devices while increasing their capabilities, but also representing a tremendous progress through an efficient and smart synthesis of materials with the exact required properties.

1.1 Semiconductor Materials

The interest around semiconductor materials arises from their electronic and optical properties, related to the existence of an energy gap between their occupied (valence band) and unoccupied (conduction band) electronic states (energy band gap, ΔE). There are two main classes of semiconductor materials, classified attending to the nature of their band gaps, as direct or indirect, as illustrated in Fig. 1.1. Whenever the maximum of the conduction band and the minimum of the valence band occur at the same crystal momentum (Fig. 1.1(a)), the gap is said to be direct, and transitions between both electronic states keep the total momentum. Therefore, the electron and hole recombination in these materials results in the emission of a photon (radiative recombination) with same energy than the gap. Contrary, those electronic bands with different momentum at the maximum of the valence band and minimum of the conduction, are indirect, and the radiative recombination process involves the participation of phonons to preserve the momentum (see Fig. 1.1(b)). Otherwise, the excitons are relaxed by non radiative processes.
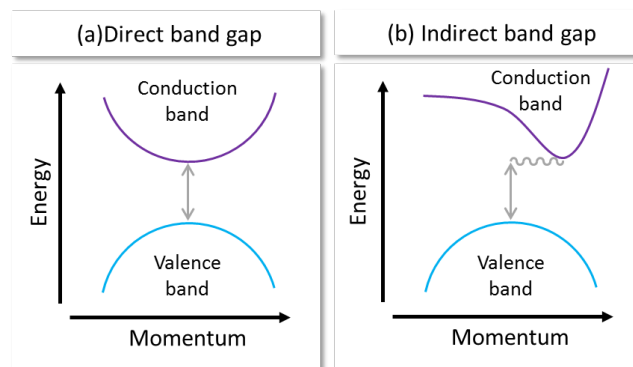
Figure 1.1: Band alignment for a direct band gap (a) and an indirect band gap (b) semiconductor.

The energy value of the band gap is closely related to the material crystal structure

and lattice constant. Indeed, every material has its characteristic band gap value conse-
quence of its composition and lattice dimensions, as illustrated in tables 1.1, 1.2 and 1.3
(only the most stable bulk phase, cubic or hexagonal, is considered for every material in
the tables). It should be noted that the possible ternary compounds derived from the
former binary combinations will have intermediate band gap values. Indeed, the energy
band gap when combining two binary compounds, Y and Z, can be estimated by the
following equation:

$$\Delta E\left(Y_{1-x}Z_x\right) = (1-x)\,\Delta E\left(Y\right) + x\Delta E\left(Z\right) - x\left(1-x\right)C \qquad (1.1)$$

which gives a quadratic dependence on the band gap with the mole fraction, x, ac-
counting also for the deviation of the linear interpolation between Y and Z through the
parameter C [1]. Consequently, the energy band gap can be tailored as function of the
material composition.

Material	AlN	GaN	InN	AlP	GaP	InP
Phase	Hexagonal	Hexagonal	Hexagonal	Cubic	Cubic	Cubic
Lattice constant (Å)	a = 3.111, c = 4.978	a = 3.189, c = 5.185	a = 3.544, c = 5.718	a = 5.464	a = 5.451	a = 5.86
Gap type	Direct	Direct	Direct	Indirect	Indirect	Direct
ΔE (eV)	6.2	3.4	0.7*	2.5	2.7	1.3

Table 1.1: Phase symmetry, cell parameters, band gap type and values (at room temperature) for
several nitride and phosphide binary combiantions, taken from `http://www.semiconductors.co.uk` [2].
*Value taken from [3].

Material	AlAs	GaAs	InAs	AlSb	GaSb	InSb
Phase	Cubic	Cubic	Cubic	Cubic	Cubic	Cubic
Lattice constant (Å)	a = 5.660	a = 5.653	a = 6.050	a = 6.136	a = 6.09	a = 6.47
Gap type	Indirect	Direct	Direct	Indirect	Direct	Direct
ΔE (eV)	2.2	1.4	0.4	1.6	0.8	0.2

Table 1.2: Phase symmetry, cell parameters, band gap type and values (at room temperature) for
different arsenide and antimonide binary combiantions, taken from `http://www.semiconductors.co.uk`
[2].

Moreover, the electrical properties of semiconductors can be tunned by doping the
material, through the incorporation of small amounts of impurities into the structure.

Material	ZnO	ZnS	ZnSe	ZnTe	CdS	CdSe	CdTe
Phase	Hexagonal	Hexagonal	Cubic	Cubic	Hexagonal	Hexagonal	Cubic
Lattice constant	a = 3.250, c = 5.207	a = 3.811, c = 6.234	a = 5.670	a = 6.100	a = 4.135, c = 6.749	a = 4.30, c = 7.020	a = 6.480
Gap type	Direct	Direct	Direct	Direct	Direct	Direct	Direct
ΔE (eV)	3.4	3.9	2.8	2.4	2.5	1.7	1.5

Table 1.3: System symmetry and lattice parameters (given in Å) along with band gap type and values (at room temperature) for several II-VI binary combinations, taken from `http://www.semiconductors.co.uk` [2].

By doing so, we are modifying the number of available free carriers and, thus, changing their conductivity. The doping can be either n-type or p-type, depending on whether the hosted atoms (dopants) increase the number of electrons (donor dopant) or holes (acceptor dopant), respectively. As a consequence, additional electronic states are induced within the band gap, which is shrunk. The incorporation of a donor results in additional energy levels close to the conduction band, while energy levels near the valence band are created due to the presence of acceptors. Apart from the nature of the dopant, the doping concentration is of extreme importance and, indeed, heavily doped semiconductors behave similarly to conductor materials, reason why they are said to be degenerated. Typical doping concentrations are in the range of 10^{13} to 10^{20} dopant atoms for cubic centimeter, corresponding to one doping atom per 10^{10} to 10^3 hosting atoms [4]. The resistivity variation within the doping range of silicon (n-doped silicon) is shown in Fig. 1.2. It can be seen that the resistivity of heavily doped silicon decreases several orders of magnitude compared to pure silicon, approaching the metallic threshold.

Of course, the crystal quality of the materials plays a critical role. Point defects, like dopants or vacancies, introduce extra electronic states within the energy band gap that may modify the electrical conductivity. These defects in semiconductors are cataloged as deep and shallow. The wave function of deep defects is highly localized whereas shallow defects show delocalized wave functions. This distinction can be applied to dopants and it is usually related (although not always) with the location of their energy states relative to the conduction- or valence-band edge. Shallow dopants are those adding extra electronic states at few mili-elctron volts from the edges of the bands, while related electronic states to the presence of a deep dopant will typically lie through the middle of the gap [4].

The presence of other crystalline defects should be accounted, too. Apart from point
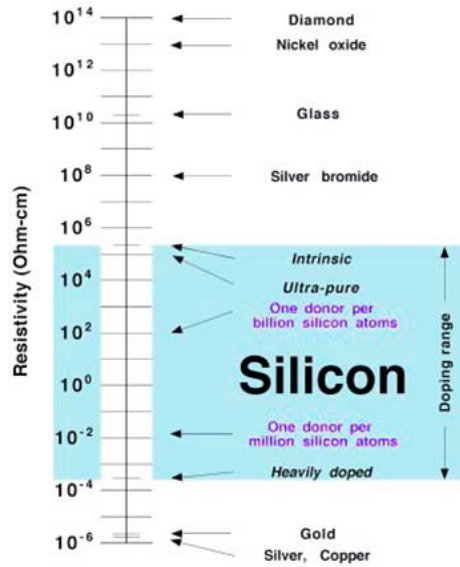
Figure 1.2: Resistivity of pure and donor-doped silicon compared to metals and insulators. Adapted from ref. [4]

defects, crystalline structures may show one and two dimensional lattice distortions. Line defects (1D) involve atomic misalignments along one crystallographic direction, and they are so called dislocations. It is widely known that dislocations act as recombination centers for the charge carriers. They are known to negatively influence the final performance of the devices, since they also create acceptor states in the band gap [5]. In the case of bulk materials, the non-radiative processes are expected to dominate the relaxation events due to the surfaces and defects of the crystals. Fortunately, nowadays the growth of high quality crystals is possible, with really low density of defects. However, as we will see along Chapter 5, dislocations are likely to show up when combining different materials in a heterostructure (misfit dislocations).

In addition, planar defects, such as twin and antiphase boundaries, are intimately related to the electronic properties. The twin boundaries are 2D defects rotating the lattice around or perpendicularly to their location, as it is explained in Section 3.1. Importantly, the periodic repetition of these kind of defects changes the crystallographic phase of the material, and thus, its characteristic band gap. As we will see, semiconductor materials are prone to suffer polymorphism between cubic and hexagonal phases (namely, zinc-blende and wurtzite, respectively), showing each phase different band gap. For instance, GaN usually crystallizes as hexagonal phase with a direct band gap of 3.4 eV, but whenever it acquires cubic symmetry, its band gap is slightly smaller, being about 3.2 eV, in agreement with ref. [2]. Similarly, GaAs ZB has been reported to have a 1.42 eV band gap while in the WZ phase it is 1.52 eV [6]. In addition, periodically twinning has been predicted to turn indirect band gaps into direct ones [7–9].

It is important to note that the presence of rotational defects may break the crystallographic symmetry in terms of the atomic pairs orientation (dumbbells), when dealing with binary compounds, AB. In fact, AB compounds have polar crystallographic directions, defined by the atomic specie facing such direction. In other words, if the $[u\ v\ w]$ direction faces A, $[\overline{u}\ \overline{v}\ \overline{w}]$ will point to B. Linked to the polar character of some compounds, defects reversing the polarity may appear. They are known as inversion domain boundaries (IDB), and they have strong implications on the electronic properties. Chapters 3 and 4 of the present manuscript are devoted to this particular issue, discussing extensively the polar growth at the nanoscale and the implications of a polarity inversion.

The growing materials can be synthesized under a variety of shapes and sizes, affecting also their opto-electronic response. The spatial confinement of charges occurs when the particle sizes are comparable to the Bohr exciton diameter, leading to quantum confinement. In such cases, the radiative process is much likely to occur since the wave function much less delocalized than in the bulk, resulting in almost unity fluorescence quantum yield. As the structures shrink, the band gap increases, meaning that at the quantum confinement regime the optical absorption/emission will occur at higher energies than in bulk materials. Therefore, the miniaturization offers another way of tailoring the band gap, as we will see along Chapter 6.

It should be mentioned that the band gap value is also temperature dependent. The thermal energy promotes the expansion of the material and the corresponding cell parameter. Hence, as a general trend, the higher the temperature, the smaller the band gap. The increased interatomic distances reduces the average potential seen by the electrons, shrinking the gap among the bands. Based on the same working principle, i.e., the larger the lattice constant, the smaller the band gap; any factor affecting the cell size can be intended to tailor the band gap. In this context, strain engineering can be applied to modify the response of the semiconductors, as it is discussed in Chapter 5.

The semiconductor industry is traditionally based on silicon devices. Silicon has an indirect band gap of ~ 1.1 eV, and it can be easily implemented in metal-oxide semiconductor field-effect transistors (MOSFETs), thanks to its native oxide, SiO_2, acting as insulator to create the oxide gate. Its intrinsic properties make silicon a suitable material for the development of integrated circuits and photovoltaic applications. Unfortunately, the indirect nature of the silicon band gap reduces the efficiency of the radiative recombination processes, which can be successfully increased by using binary compound semiconductors with direct gaps. Then, although silicon is relatively abundant on earth and cheap, III-V and II-VI combinations show superior optoelectronic

properties and allow spreading the operation range of the devices expanding over the visible range.

Therefore, along this dissertation, we deal with binary semiconductors, synthesized at the nanoscale, with especial emphasis on nanowires (NWs). The complexity of the studied systems here, follows a linear progression along the manuscript, from binary compound NWs (III-V and II-VI), to sophisticated quantum structures contained within NWs, passing through the analyses of simpler heterostructures (axial and radial/coaxial).

1.2   Semiconductor Nanowires

Objects are considered nanostructures when at least one of their dimensions is below the threshold of few hundreds of nanometers. Following this definition, different types of nanostrucutures can be defined going from nanoparticles, nanodots or nanoislands to nanomembranes, passing through nanowires; having three, two or one dimensions within the nanoscale regime. Fancier nanostrucutures can be also synthesized nowadays as, for listing some of them, nanopores and branched structures, including nanotrees and multipods (like tripods or tetrapods). Some of these nanostructures are reported in Fig. 1.3.

When only one dimension is within the nanoscale regime, we distinguish among thin films and 2D nanostructures laterally confined. Along this manuscript, we will deal only with those cases where the 2D structures have a defined lateral extension, such as nanomembranes (growing vertically outwards from the substrate) or nanoplates (growing as lying structures on the substrate), but not with thin films, which imply "non-confined" surfaces (with infinite planar dimensions for the nanoscale regimen).

Importantly, nanostructures show modified properties compared to bulk materials, mainly due to their enhanced surface-to-volume ratio. Moreover, the band gap of semiconductor materials can be tuned as function of the synthesized shape and size.

Among the different possible morphologies, nanowires (NWs) have been extensively synthesized, reaching a huge control over their growth. Consequently, good quality crystals can be successfully obtained with high yields under the NW morphology. Typical NWs have diameters of few tens of nanometers while show lengths of hundreds of nanometers (even reaching micrometer lengths). Shorter NWs are usually referred as nanorods. The 1D nature of this geometry confines the electrons, holes and/or photons radially allowing their movement mainly along the axial direction. Then, the spatial particle confinement induced by the geometry, along with the high refractive index
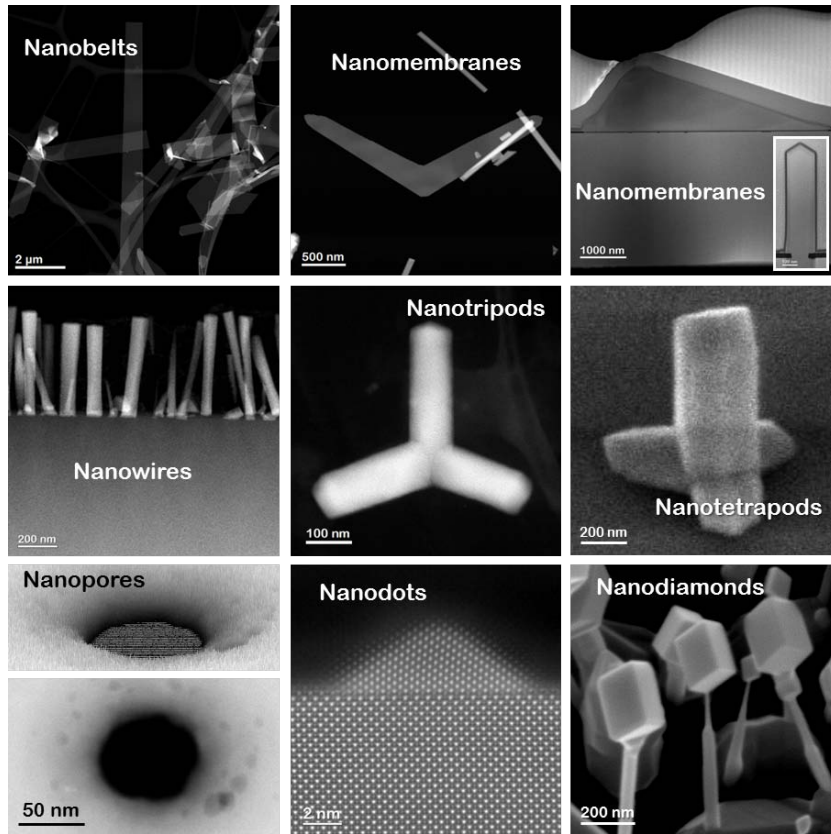
Figure 1.3: Electron micrographs of different types of nanostructures.

of the NW sidewalls, allows the creation of nanocavities, acting as optically pumped lasers [10–12]. Thanks to their capability to guide the light, they have been recently reported to act as optical nanoantennas, too [13]. Many other applications can be found based on their excellent photonic properties, that make them suitable structures for the performance of a variety of devices, including photodetectors [14–16], light-emitting diodes (LEDs) [17–20], solar cells [21–24] and optochemical sensors [25, 26], for listing some of them.

Additionally, NWs are highly useful for the study of fundamental physics phenomena. For example, InSb NWs have been reported to show signatures of Majorana fermions [27, 28], which are particles identical to their own antiparticles.

Apart from the band gap engineering offered by the nanostructuration, the modulation of electronic band alignments can be achieved by the creation of interfaces, where different phases match together, as explained in the following sections.

1.3   Heterostructured Nanowires

An important path through the materials functionalization consists in combining different materials within the same structure. Linked to their filamentary shape, NWs allow the creation of heterostructures under two different configurations:

- Axial heterostructures, whenever the different crystalline phases are piled up along the NW growth axis

- Coaxial (or radial) heterostructures, if the materials are combined around the NW axis, creating shells

These two types of heterostructures are schematically shown in Fig. 1.4, along with experimental examples obtained by means of electron microscopy. Moreover, it is usually possible to switch the material at will, allowing the formation of multi-heterostrutures.
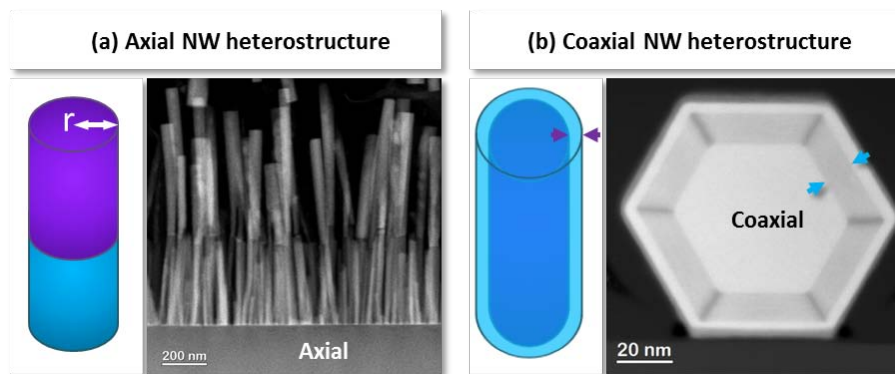
Figure 1.4: Sketches corresponding to two different nanowires heterostructures (a) axial and (b) radial or coaxial, along with experimental images.

Combining different materials allows the creation of heterojunctions or heterointerfaces, advantageous to engineer the band structure of the system. The behavior of the heterostructure is reliant on how the conduction and valence bands are aligned respect to each other, which determines, for instance, the emission intensity and recombination lifetimes. As consequence of the different energy levels of the valence and conduction bands of the materials involved, the potential profile near the heterojunction will show discontinuities. The heterostructures can be then classified as type I, II or III according to the resulting band alignments, illustrated in Fig. 1.5.

The type I alignment is the result of combining two semiconductors, A and B, in which the band gap of one of them (ΔE_B, following the labeling in Fig. 1.5) lies completely within the band gap of the other (ΔE_A), as shown in Fig. 1.5(a), reason why

it is so called stradding. In such cases, $E_{V,A} > E_{V,B}$ and $E_{C,A} < E_{C,B}$, being $E_{V,x}$ the energy of the valence band for material x and $E_{C,x}$ the energy corresponding to the conduction band of x ($x = A$, B). In this situation, electrons and holes tend to localize in the material with the narrower gap (A in our example). As the carriers are confined within the same region, this type of alignment is higly useful for the development of light emitting devices, being the emission energy determined by the material with the smaller energy band gap. Most IV and III-V materials combinations lead to the formation of type I band alignments, as for instance it happens in the GaAs/AlGaAs system [29].

Contrary, if only the conduction or valence band of one of the components of the junction is contained within the energy gap of the other, the junction is classified as type II (see 1.5(b)), also known as staggered. Therefore, type II interfaces are created whenever $E_{V,A} > E_{V,B}$ and $E_{C,A} > E_{C,B}$, or, inversely, $E_{V,A} < E_{V,B}$ and $E_{C,A} < E_{C,B}$. Consequently, electrons and holes tend to be spatially separated at both sides of the interface and the emission energy is determined by the difference between the higher valence band of one material (higher energy valence band, $E_{V,A}$ in the figure) and the conduction band of the other (lower energy conduction band, $E_{C,B}$), $\Delta E = E_{C,B} - E_{V,A}$. The spatial carrier separation of this type of alignment makes these systems ideal candidates for the development of photovoltaic devices and detectors. To give an example, CdSe/ZnTe heterostructures have been reported tow show this type of alignment when both phases crystallize on the hexagonal phase [30].

Finally, the last possible situation, type III junction, accounts for a broken gap where there is not overlapping of the band gaps of both combined materials, as shown in Fig. 1.5(c). Such situation is exploitable to induce the carriers tunneling, allowing the development, for instance, of quantum cascade laser, energy-efficient transistors with applications in multi-junction solar cells [31] or as tunnel field-effect transistors [32]. InAs/GaSb interfaces are an example of these kind of junctions.

A conspicuous issue regards the sharpness of the junction in terms of its composition. The formation of graded interfaces among the two combined materials modifies the band alignments and the offsets of the band discontinuities, even inducing the change from one type to another [33]. As we will see along Section 3.2.2, a common route followed to synthesize nanowires relies on the use of pre-deposited metallic droplets, which may host residual reactants from the growth of the former material when switching the conditions for the growth of the subsequent one. This is known as the reservoir effect and it results in the formation of interfaces [34] with mixed compositions at the junction between the two materials. Although controlling the species solubility in the droplet overcomes the drawback [35], it is not a straightforward issue, especially when switching among binary compounds, where a deep understanding on how the precursor interact
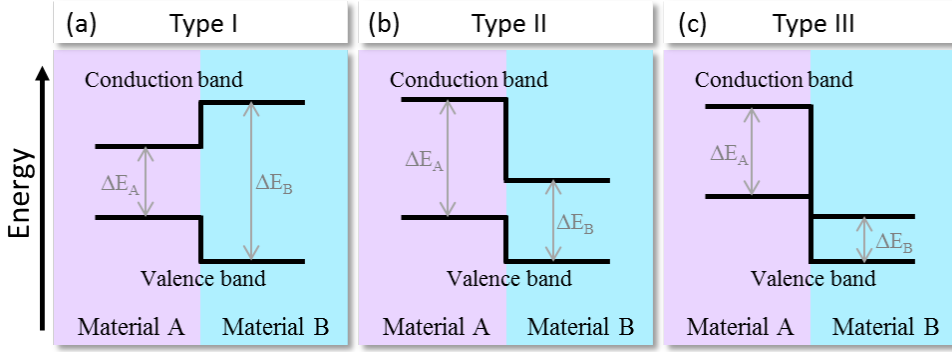
Figure 1.5: Classification of the possible semiconductor heterojunctions attending to their band alignment.

with the alloy is needed. Moreover, the grading is usually stronger in one direction [36], as reported for InAs/GaAs interfaces, where switching from InAs to GaAs results in sharper interfaces than the other way around (from GaAs to InAs) [37]. Hence, the abruptness of the junction should be accurately addressed in order to understand the response of the system and being able to optimize the devices.

As we have mentioned earlier, the band gap can be tuned as function of the crystallographic phase adopted by the material, without inducing any compositional change on the compound. That is the case, for instance, of GaN (showing $\Delta E_{ZB} = 3.2$ eV and $\Delta E_{WZ} = 3.4$ eV) or ZnS (with $\Delta E_{ZB} = 3.7$ eV and $\Delta E_{WZ} = 3.9$ eV). Moreover the different polytypes may have different band off-sets, attractive for the creation of barriers and wells for the carriers. For example, a small insertion of hexagonal Silicon within the cubic matrix, induced by the appearance of a twin boundary, creates a barrier for the electrons. Contrary, case of InP, the same situation (formation of twin within the cubic matrix to create a hexagonal domain) will act as well for the carriers. Indeed, the band off-sets are modified depending on the polytypes combined at both sides of the interfaces [38], meaning that boundaries combining different polytypes will show different band alignments.

In addition, the band gap can be further tune by mechanical strain [39], inducing also changes in the band alignment of combined phases [40].

The band profiles can be also tuned by tailoring the size of the system. Indeed, for the case of twinning superlattices, there is a diameter threshold (material dependent, since it is linked to the compound ionicity), shown in Fig. 1.6, for different materials, at which the valence band off-sets of the cubic and hexagonal phases are coincident. Accounting for this phenomena, it is possible designing type II band profiles for wires with diameters above the calculated critical value, since the conduction band of the

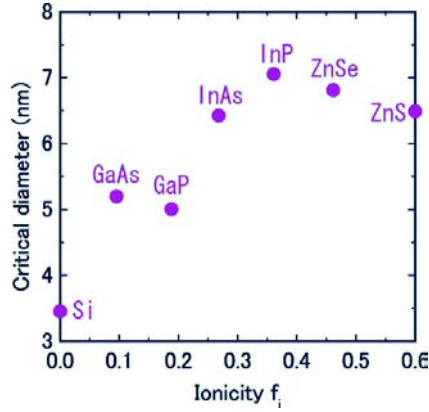hexagonal polymorph is assumed to be higher than the cubic.

Figure 1.6: Calculated critical diameter for different semiconductor NWs, at which the valence band off-set for the hexagonal and cubic phases are coincident, plotted as function of the compound ionicity, f_i. Adapted from ref. [38].

Importantly, the heterointerfaces created between the two combined materials will show interesting properties. It should be noted that, when combining different materials within the same structure, the induced lattice strain will influence the band alignments and thus, it will modify the final material properties. In this context, NWs offer a unique platform for the combination of highly mismatched materials, thanks to their high surface-to-volume ratio. As consequence of their small NW cross-section, the connecting materials have a small contact area and a wide surface that favors an efficient strain release. Accordingly, materials with high relative mismatches can be coherently connected. The materials will be strained by the effect of the different lattice parameters, since the second growing material will try to match the former grown one, distorting the cell dimensions, and thus, changing the material properties. As the lattice parameter is related to the band gap, any optic or electronic property of the material will be modified by the strain. It should be pointed out that the strain can affect in two opposite ways, acting either tensile (lattice expanded compared to the pristine material) or compressively (lattice parameter smaller than expected), which strength will be related to the lattice mismatch and epitaxial relationship.

Additionally, the role of the polarity on the band discontinuities must not be underestimated. As we will see along Section 3.1, certain crystallographic directions in non-centro symmetric phases point either to the A- or to the B-specie of the compound, allowing the distinction between A- and B- polar directions. Interestingly, the different polar combinations when combining two binary materials, are expected to result in different band bending and discontinuities [41].

All together, semiconductor NWs turn into attractive materials for fulfilling the present technological requirements and into excellent building blocks for the study of fundamental physical principles.

1.4   Quantum Structures in a Nanowire

We have already mentioned about the carriers confinement imposed by the miniaturization of the materials. In fact, systems with sizes comparable to the Bohr exciton diameter exhibit spatial charge carriers separation, and the materials are said to show quantum confinement. Although the usual diameter of the NW is typically too large for exhibiting quantum confinement effects, it is still possible to assemble smaller structures within the wires showing those effects. Therefore, insertions of dissimilar crystallographic phases in a NW allow the design of different quantum structures, either axially or radially. Such structures are classified in three main groups attending to their dimensionality, responsible of the type of quantization of their electronic density of states (DOS). Two, one and zero dimensional structures, known as quantum wells (QWs), quantum wires (QWRs) and quantum dots (QDs), confine the carriers in one, two or three dimensions, respectively [42]; which we will comment in the following.

The DOS shows a functional dependence with the energy, that varies as consequence of the dimensionality of the system. Thus, reducing the dimensionality of the systems leads to the transformation of the DOS from parabolic (DOS $\propto E^{1/2}$) in 3D or bulk materials to different quantized levels. In 2D structures, the DOS shows a ladder shape dependence, with DOS at constant energies. Going one step further and inhibiting the carriers movement in an extra dimension gives rise to 1D structures, where the DOS is proportional to $E^{-1/2}$. Finally, the total spatial carrier confinement in 0D structures or dots shows discrete DOS ($\propto \delta E$).

The carriers spatial confinement is reached by the creation of potential barriers, isolating physically the active material. The mastering achieved nowadays on the synthesis of NWs, turns this systems into ideal platforms for the integration of QSs through compositional or phase variations. Moreover, QSs integrated within NW waveguides usually show enhanced brightness compared to those assembled within bulk materials or 2D layers.

1.4.1 Quantum Wells, QWs

The stacking of layers of different crystallographic phases in both configurations, axial or radial, along the NW axis, lead to the formation of 2D quantum structures (QSs) or quantum wells (QWs). Radial coatings on the facets of the NWs, creating shells along the length of the wires, result on the formation of radial or coaxial QWs. Then, NWs are firstly grown as templates to proceed with subsequent depositions of other phases concentrically. Importantly, the thickness and homogeneity of the wells/barriers play a key role on the behavior of the systems. In this context, when using molecular beam epitaxial procedures, the orientation of the template NWs with respected to the material source is crucial for the deposition. While NWs standing normal to the substrate surface allow the formation of homogeneous coatings on their facets (see Fig. 1.7(a,b)), tilted NWs develop asymmetric shells due to shadowing effects (see Fig. 1.7(c,d)).
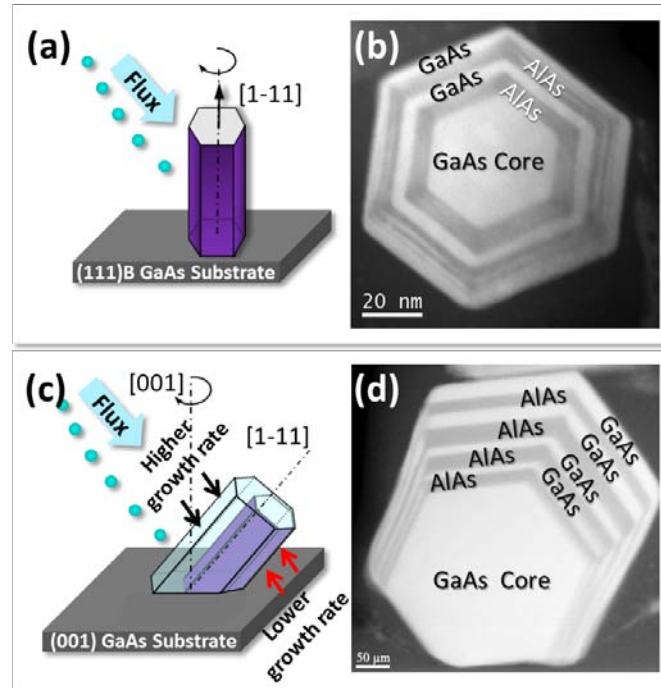
Figure 1.7: GaAs NWs growing along $\langle 111 \rangle$B direction, on (111)B GaAs (a), and on (001) GaAs (c). In both cases the NWs follow the substrate $\langle 111 \rangle$B direction, which is normal to the surface in (a) and 35° tilted in (c). Consequently, (111)B substrates allow the formation of homogeneous shells (in thickness), as shown in (b), while on (001) substrates some facets suffer shadowing effects, resulting in inhomogeneous shells, as shown in (d). Adapted from [42].

As consequence of the epitaxial growth of the wires on the substrate, their tilting angle is controlled by the orientation of the substrate employed. For instance, GaAs NWs synthesized by molecular beam epitaxy (MBE), are known to follow preferentially $\langle 111 \rangle$B directions during their growth. Thus, using (111)B GaAs substrates vertical

NWs are obtained, but other substrate orientations, for example (001) GaAs, lead to the formation of 35º tilted NWs, following one of the $\langle 111 \rangle$B crystallographic directions of the substrate [43, 44].

By modifying either the thickness of the QWs or the barriers composition, the carriers confinement can be tuned. For instance, the thickness dependence emission allow the performance of wavelength controlled laser [45] or photodetectors [46].

Alternatively, axial combinations along the NWs axis are also possible. Such thin axial insertions are sometimes referred as nanodiscs (NDs) instead of wells. Many examples of axial QWs can be found involving GaN NWs, alternated with $Al_xGa_{1-x}N$ acting as barrier and, then, the GaN as active material [47–49], or $In_xGa_{1-x}N$ as emitting material and,thus, GaN conforming the barriers [50, 51].

Playing around with the composition of the $X_xGa_{1-x}N$ alloys (X = Al, In), the related mismatch strain among phases can be tailored at will, offering a useful tool for the band gap engineering. Moreover, in GaN/AlGaN NW axial systems, the axial growth of the barriers is usually accompanied by a slower radial overgrowth. Consequently, the GaN insertions (QWs) will be surrounded by the $Al_xGa_{1-x}N$ barriers, preventing the lateral strain release. If piling up several QWs and barriers, those wells closer to the base will have thicker $Al_xGa_{1-x}N$ shells than those nearer the NW tip, inducing a strain gradient along the NW length [52]. Of course, the strength of the effect is also related to the Al content of the barriers.

1.4.2 Quantum Wires, QWRs

1D spatial confinement is mostly reported for embedded systems within bulk materials or 2D layers [53, 54]. However, there are few cases where QWRs have been reported integrated in NWs, mainly as cores in core@shell systems [55].

Alternatively, self-assembled QWRs have been reported to form along the corners of hexagonal GaN prismatic NWs [56]. The approach requires the creation of GaN NWs working as stems for the later growth of an axial GaN NDs, isolated from the GaN stem by an AlN insertion. The GaN lateral facets of the NW belong to the $\{1\bar{1}00\}$ family plane, while the AlN develops further $\{11\bar{2}0\}$ facets in addition to the GaN ones, truncating the corners of the hexagonal section. These AlN $\{11\bar{2}0\}$ exposed surfaces allow the deposition of GaN while axially growing the NDs, but not on the $\{1\bar{1}00\}$ due to the non-favorable surface energy. Therefore, the truncated corners or edges of the AlN barrier are filled by GaN, giving rise to the creation of up to six QWRs at every NW.

The optical characterization of those systems show two emission bands, one corresponding to the GaN base, slightly blue shifted by effect of the AlN compression (at around 3.5 eV), and another at higher energies (3.85-4.05 eV) related to the presence of QWRs. In fact, analyses performed by means of micro-photoluminescence (μ-PL) on individual NWs show several narrow emission lines corresponding to the different QWRs contained, as consequence of the size spreading of the wires (size effects on the emission energy). Cathodoluminescence (CL) measurements performed on the sample confirmed that the measured emission by PL is mainly centered at the intermediate AlN region, where the QWRs are assembled [57].

1.4.3   Quantum Dots, QDs

Finally, discrete quantized electronic states can be obtained by the creation of 0D structures or quantum dots, QDs. Contrary to the case of QWRs, QDs are extensively reported coupled to NWs. The synthetic routes to achieve the formation of QDs within NWs mainly, rely on one of the Stranskii-Krastanov mechanism or on self-induced diffusion processes.

Stranskii-Krastanov QDs on the NW surfaces

To illustrate those cases following Stranskii-Krastanov QDs formation at the external facets of NWs, we will focus on the case of GaAs NWs containing InAs QDs. Importantly, GaAs NWs show hexagonal cross-sections, laterally bordered by {110} or {112} facets, depending on the synthesis method employed.

Whenever the NW GaAs growth proceed through the Ga-assisted method [58] the resulting wires show {110} lateral facets. As the InAs deposition is highly unfavored on the {110} GaAs surfaces, an AlAs coating the NW sidewalls is needed before the assembly of the QDs [59]. Their preferential distribution on the lateral facets or along the edges, have been theoretically predicted as a function of the NW diameter [60]. For thin NWs only nanorings are created instead of isolated QDs, but, when NWs overcome a critical size, the formation of QDs on the facets it is allowed. Exceeding the next size threshold, the QDs are mainly formed at the edges of the NWs; and, finally, if the NWs are thick enough the formation of QDs in both, facets and edges takes place.

Some other synthesis methods employing metal catalyst, as the metal organic vapor chemical deposition (MOVCD) method, result in the formation of {112} faceted GaAs NWs, that directly allow the InAs QD formation by adatom diffusion [61]. Thus, the InAs deposition time and NW diameter are key parameters on the final coverage of the

facets. In principle, the thicker the NWs, the easier the QDs formation, since less In atoms are needed to conform the wetting shell. However, there is a critical diameter above which the NWs will be partially covered by the QDs.

Self-induced diffusion driving the formation of QDs

Another approach for the creation of QDs contained in NWs relies on the different diffusion lengths of the species involved along certain crystallographic directions. This is case of GaAs/AlGaAs coaxial NWs, where the different mobilities of Ga and Al result on the formation of Al-rich stripes along the six edges of the AlGaAs shell. Interestingly, inhomogeneities on the stripes composition lead to the Al-rich barrier bifurcation, creating confined Ga-rich regions or QDs [62], as shown in Fig. 1.8.
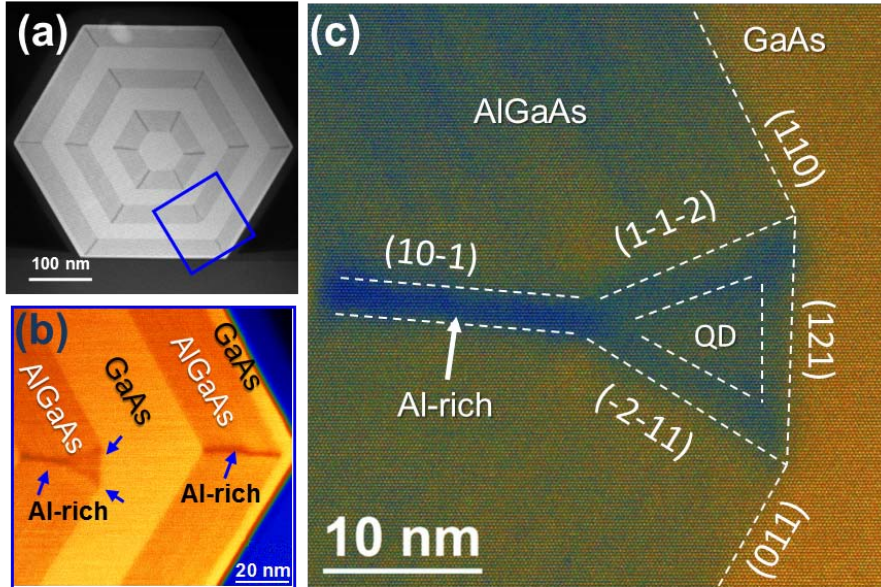
Figure 1.8: Radial GaAs/ $Al_xGa_{1-x}As$ NW system containing GaAs QDs analyzed in cross-section. (a) Low magnification HAADF image of the NW section. The darker areas are Al-richer. (b) Atomic resolution image of the blue squared corner of the wire in (a), further magnified around the QD in (c). Adapted from [42].

In all the cases discussed, photoluminescence and/or cathodoluminescence measurements have been performed, probing the material quality and degree of confinement.

As we have seen, non-planar nanostructures, such as nanowires, nanomembranes, tripods, etc., and related nanoscale systems containing combinations of materials to create heterostructures, or even defining quantum structures, have high potential interest for their application in electronics and optoelectronics. In this way, a precise

characterization of their structure and composition at the atomic scale is needed, to deeply understand their final physical properties. Along this dissertation, we atomically characterize non-planar semiconductor nanostructures, by means of Transmission Electron Microscopy (TEM). Most of the results here presented have been obtained by operating the microscope in scanning mode (STEM), as explained in detail along the following chapter (Section 2.3).

Methodology

Along this chapter, the basic principles of the transmission electron microscopy and related techniques are summarized. Especial emphasis is put into the individual atom imaging in scanning mode thanks to the development of aberration correctors. The concept of spatial resolution and their main limiting factors are introduced in section 2.1, while its improvement by implementing devices to compensate the lenses aberrations is described in section 2.2. An entire section, 2.3, is devoted to the scanning mode (STEM), since the derived techniques established the experimental basis for the present thesis. There, the related imaging and spectroscopic techniques are briefly described. Finally, the two last sections concern the data treatment implemented afterwards. In section 2.3, we introduce the strain concept and how to measure it from atomic resolution images, and lastly, section 2.4 deals with the 3D atomic modeling, image simulation and image improvement for the case of STEM images.

2.1   Few Words about Transmission Electron Microscopy

As the eyesight works within the visible range of the electromagnetic spectrum, our capability to observe objects is limited by visible light wavelength. By assembling different lenses, as in an optical microscope, it is possible to magnify the observed objects but, the ultimate resolution achievable is still limited by the wavelength of the light. Rayleigh criterion establishes the shorter distance resolved by an optical microscope, described in terms of the wavelength radiation, λ, the media refractive index, μ, and the collection semi-angle, β as follows:

$$\delta = \frac{0.61\lambda}{\mu \mathrm{sin}\beta} \approx 0.61\lambda \qquad (2.1)$$

Therefore, smaller distances will be resolved by taking advantage of spectral ranges with higher energies and, hence, shorter wavelengths. In order to achieve the atomic scale visualization, high accelerated electrons are used. λ can be controlled by the accelerating voltage employed, in agreement with de Broglie's description

$$\lambda = \frac{1.22}{\sqrt{E}}, \qquad (2.2)$$

meaning that the higher the power supplied, the better the resolution. Old microscopes are equipped with thermoionic sources to extract the electrons by heating the material (W or LaB_6). The poor brightness and broad energy distribution of the termoionic electron beams, have been greatly improved with the implementation of field-emission guns (FEG). In TEMs equipped with FEG sources, the electrons are extracted by applying a voltage to a sharp tip, resulting in more collimated electron beams with higher

brightness.

Rayleigh's criterion is a practical rule, not governed by any physical principle, giving a rough estimation of the ability to discern images from incoherent self-luminous sources. A more rigorous definition of the resolution can be established as the radius of the Airy disk, emerging while waves pass through an aperture accordingly to Abbé's theory. Even in absence of aberrations a single point will be imagined as a disc, just by the finite size of the lens. In this way, the radius of the Airy disc (described in 2.3) represents the maximum resolution attainable.

$$r = 1.22\frac{\lambda}{\beta} \tag{2.3}$$

Directly looking at the expression, it is clear that the resolution can be improved either by using smaller λ, set through the acceleration voltage, or by increasing the lenses collection angle. However, we are assuming ideal lens, aplanatic, inexistent in practice. The spherical aberration, C_s, is unavoidable in any lens due to the higher bending experimented by those rays passing the lens far away from the optical axis, while rays undergoing the paths closer to the axis will be weakly bended. As a consequence, a point object becomes a disc after crossing the lens, which radius, r_{sph}, scales with the collection angle, as shown in equation 2.4.

$$r_{sph} = C_s\beta^3 \tag{2.4}$$

In addition, the different energies of the electrons after crossing the specimen also contribute to the image blurring. This effect is the result of the different bending induced by the lenses to the electrons depending on their wavelength, since the electrons with higher energies are less deviated than those with lower energies. Therefore, the chromatic spread of the emerging electrons is somehow enhanced while crossing the lenses, turning punctual objects into discs of radius:

$$r_{\mathrm{chr}} = C_c\frac{\Delta E}{E_0}\beta, \tag{2.5}$$

where E_0 is the energy of the incident electron beam and ΔE is the energy lost in the process. Dealing with thin TEM specimens, the influence of the chromatic aberration is negligible compared to the spherical one. Thus, only if compensating the spherical aberration the effect of the chromatic spreading of emerging electrons may be noticed. The changes in an image induced by the lenses aberrations is mathematically represented

by the Contrast Transfer Function (CTF), accounting for the defocus, Δf, C_s and astigmatism, A_1. The phase signal transmitted to the real space in the image plane and, thus, the information translated to the image, is controlled by the CTF. The function is dependent on the spatial frequency domain, k-space, and the useful range is determined by the first zero of the function, known as resolution point. Interestingly, Scherzer noticed that the CTF can be optimized by properly compensating the C_s by a negative defocus as follows

$$\Delta f_{Sch} = -1.2(C_s\lambda)^{\frac{1}{2}} \tag{2.6}$$

And it gives the best performance for a microscope, unless processing the data. The aim of these considerations is achieving the maximum number of beams in phase to create the image, which is the basic principle governing the phase-contrast imaging in high resolution TEM (HRTEM). Under Scherzer considerations, the TEM resolution can be redefined as

$$r_{Sch} = 0.66 C_s^{\frac{1}{4}} \lambda^{\frac{3}{4}} \tag{2.7}$$

Therefore, the resolution is unavoidably limited by the lenses aberrations. For further details and expanded explanation on the TEM image formation and instrumentation the reader is addressed to ref. [63]. Fortunately, nowadays it is possible correcting the spherical aberration of the microscope lenses, improving the spatial resolution down to the angstrom scale. Moreover, compensating C_s leads to the correction of higher order aberrations, as coma or three fold astigmatism, as we will see along the next section. It should be noted that the great benefit offered by aberration correctors is not restricted to the increased spatial resolution in TEM mode, but also has allowed enormous improvement in scanning mode (STEM). As we will see in Sec. 2.3, a transmission electron microscope can be operated in scanning mode by converging the electron beam into a small probe which is scanned over the sample, where its brightness and size play a crucial role in the resulting image.

2.2   Aberration Correctors

The electromagnetic lenses employed to guide the electrons inside the microscope column are intrinsically imperfect and, thus, they distort the image. The lowest order aberration, namely the defocus, is easily compensated by bringing the image to the right height of the optical axis. Apart from that, the correction of the other aberrations is achieved by the employment of dipoles, quadrupoles, hexapoles and octupoles, combined in different ways in order to apply magnetic fields perpendicular to the optical

axis that directly bend the electron beam.

It is noteworthy that the path followed by the electrons traveling down the microscope column is helical, induced by the magnetic field created by the lenses. Inhomogeneities in this magnetic field result in different focal planes for propagating rays along perpendicular directions and thus, asymmetric elongation. This aberration is known as astigmatism. Fortunately, it can be easily compensated with stigmators, consisting on two orthogonal quadrupoles which effect is transforming a point into a line.

Regarding the main axial aberrations, i.e., chromatic and spherical, Scherzer found out that they are unavoidable if the electron optical system employed simultaneously fulfills the following requirements:

a. The system is rotationally symmetric

b. It produces a real image of the object

c. The system has stationary fields

d. There are not electron charges at the optical axis

Meaning that breaking one of them, the spherical and chromatic aberrations could be corrected. Few years after, he predicted their compensation by combining quadrupoles and octupoles and thus breaking the rotational symmetry. Unfortunately, the technological limitations in those times (it was already 1947), hindered its experimental demonstration. In fact, it was not until 1998 when the first system for compensating the spherical aberration of the objective lens was constructed and successfully implemented in a 200 kV microscope [64]. Among all the lenses of the microscope, the objective one is maybe the most important, since is the lens forming the image in TEM mode. Such corrector system consisted of an arrangement of two hexapoles and four lenses alternating as follows: one hexapole - two dipoles - one hexapole - two dipoles. The point resolution was measured to improve from 0.24 to 0.14 nm in a 200 kV FEG microscope (Philips CM 200), and the contrast delocalization was strongly reduced. The working principle of the corrector, based on Rose's suggestions, is to compensate the non-rotationally second-order aberrations of the first hexapole with the second one. Off-axial coma is also minimized with this imaging setup and only higher order aberrations, as fifth order spherical aberration, will remain. Parallel to the apparition of Haider's and co-workers hexapole corrector system, Krivanek et al. [65] developed a similar system but combining quadrupoles and octupoles instead of hexapoles. In this case, the corrector is formed by four quadrupoles and three octupoles alternating. Both prototypes have evolved trough two commercial aberration-correctors, being competitor brands.

The first step before performing aberration-corrected TEM experiments is diagnose and measure the strength of the actual aberrations in our system. The usual way to
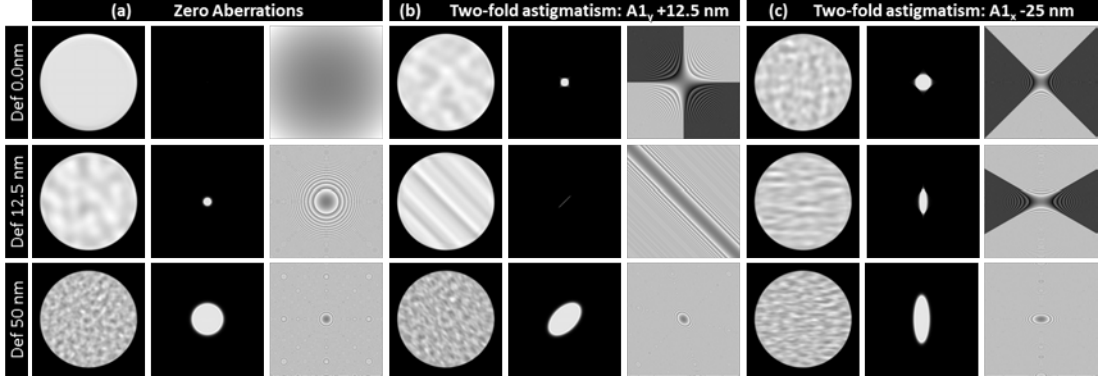
Figure 2.1: Ronchigram, coherent intensity probe and phase plate (left, middle and right columns, respectively) calculated for an amorphous sample under three different focus values (0.0, 12.5 and 50 nm from top to bottom) for an aberration-free system (a) and two examples showing two-fold astigmatism (moderated along y (b) and stronger x astigmatism in (c)).

proceed is acquiring diffractograms (in HRTEM mode) or images of the electron probe (in STEM mode) at different beam tilts, under- and over focus for every tilt value. The collection of resulting diffractograms is known as Zemlin's tableau. The evaluation of the induced defocus and two-fold astigmatism as function of the illumination tilt allows the estimation of the rest of aberrations, that will be compensated by the correction system.

Although the aberration diagnosis and compensation are highly automatized in the commercial available systems, visualizing the aberration effects is highly useful. When working in scanning mode, this can be done by evaluating the Ronchigram. As we will see along the following section, in scanning mode we illuminate the sample with a small electron probe. Therefore, aberrations in that mode are mainly due to the lenses forming the probe rather than from those forming the image (as it happens in HRTEM mode). The Rochigram, defined as the shadow image of the sample (thin object) or, alternatively, as the convolution of the aperture function with the diffraction pattern of the sample, it is a valuable tool for assessing the aberrations affecting the system. Starting by the lower-order aberrations possible, Fig. 2.1 shows the Ronchigram deformations as consequence of astigmatism along perpendicular directions (i.e., x and y), along with the coherent intensity probe and the phase plate. The aberration-free example is also included for comparison. The coherent intensity probe, *J(r)*, represents the squared wave function of the incoming electrons at the object plane ($\phi(r)$). *J(r)* is calculated in the Fourier space by applying the actual aberration function, $\chi(\omega)$, for every beam crossing the condenser aperture, $A(\omega)$ and finally calculating the inverse Fourier transform,

$$J_{(r)} = |\psi(r)|^2 = \left| FT \left[A(w) \, e^{i\chi(\omega)} \right] \right|^2 \tag{2.8}$$
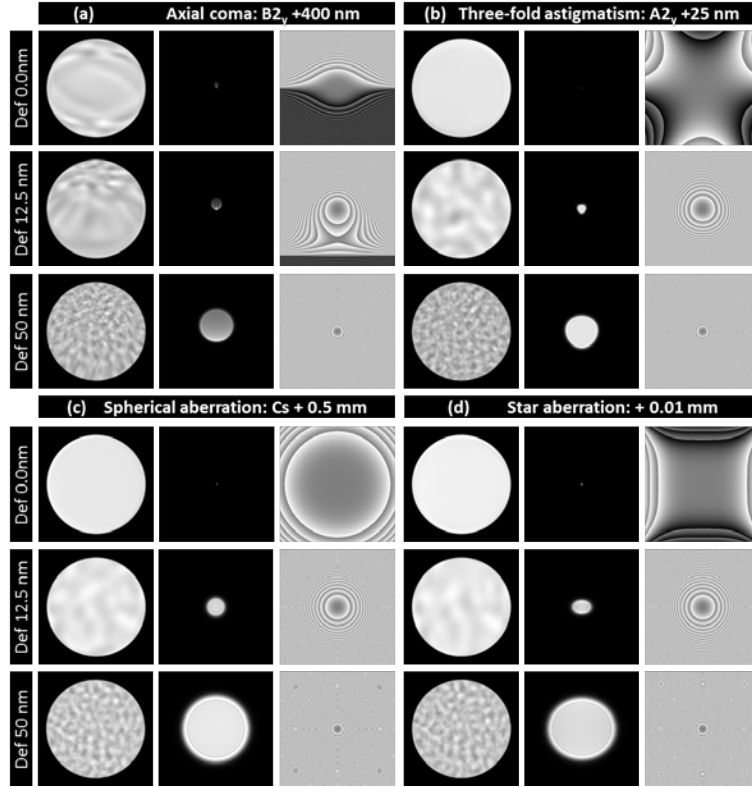
Figure 2.2: Ronghigram, coherent intensity probe and phase plate (left, middle and right columns, respectively) calculated for three different focus values (0.0, 12.5 and 50 nm from top to bottom) different aberrations values: coma (a), three-fold astigmatism (b), spherical aberration (c) and star aberration (d).

The aberration function includes the different geometrical aberrations, meaning that the chromatic aberration is excluded, and the expression can be arranged in different terms related to the different aberrations (given by the coefficients). At this point, it is worth to mention that there are two nomenclature system to refer the aberrations, linked to the two types of correctors. Apart from the deformation induced by the astigmatism on the probe, which is not round but elongated (compare Fig. 2.1(b,c) to (a)), the figure evidences the larger size of the probe as function of defocus. Regarding the phase plate, it shows the induced phase shifts by the aberrations.

The experimental effect of higher order aberrations, such as coma, three-fold astigmatism, spherical or star aberrations can be evaluated in Fig. 2.2. Axial coma, B_2 or $C_{2,1}$, is related to the parallelism of the illuminating system respect to the optical axis, and it makes off-axis objects appearing like if they had tails. Consequently, the center of the Ronchigram is laterally shifted with defocus, instead of wobbling concentrically, as shown Fig. 2.2(a) and the probe intensity is not homogeneous.

The effect of spherical aberration (third order), C_3 or $C_{3,0}$ is bringing off-axis rays to a different focus plane than that of the paraxial rays, broadening the probe and, thus, reducing the spatial resolution. Its effects on the probe intensity and on the Ronchigram are illustrated in Fig. 2.2(c), along with the induced phase shift. Similarly, the figure includes the derived deformations of electrons probes formed by lenses affected by three-fold astigmatism (b), A_2 or $C_{2,3}$, and star aberration (d), S_3 or $C_{3,2}$.

2.3 Scanning Mode, STEM

Transmission electron microscopes are versatile tools that can be operated in different modes. The variety of resulting techniques can be firstly classified attending to the illumination employed, i.e., parallel illumination in convectional TEM or convergent for the scanning mode (STEM). Interestingly, Cowley found that there is an equivalence relationship between HRTEM and BF STEM, based on the Helmholtz reciprocity theorem and, therefore, known as principle of reciprocity. The primary idea is the fact that if a point source, S, placed at A gives rise to an intensity I at the position P, the same intensity would be obtained by translating the source from A to P. Thus, for HRTEM and BF STEM, the reciprocity is referred to similar ray diagram of both techniques, being the electron trajectory the same but oppositely directed (the BF STEM ray diagram is the HRTEM upside down, as schematically illustrates Fig. 2.3).
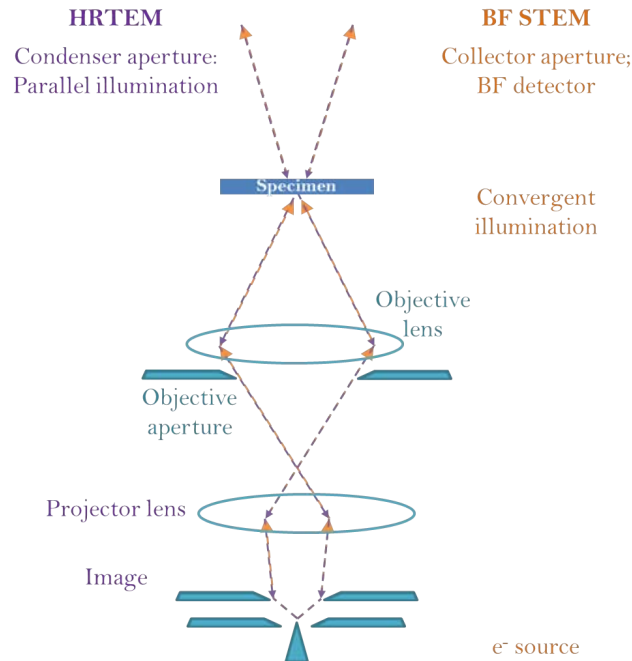

Figure 2.3: Schematic representation of the principle of reciprocity between HRTEM (purple) and BF STEM (orange).

Another useful distinction is related to the signal collected in terms of whether it accounts for the unscattered electrons (direct transmitted beam) or not, giving rise to bright field (BF) and dark field (DF) imaging, respectively. Other important concepts that should be defined before going into detail are the elastic or inelastic electron scattering, depending on the energy lost by the electrons: whenever they keep their initial energy while crossing the sample the process is said to be elastic, otherwise, if electrons loose energy the process is inelastic. Also the coherency, referred to the phase of the collected electrons plays an important role, leading to coherent and incoherent imaging, as we will see.

Therefore, many techniques can be developed within a TEM, depending on the setting parameters and collected signals. Fig. 2.4 schematically shows some meaningful signals emerged as result of the electron-matter interaction, that can be collected giving different structural and chemical information on the analyzed sample.
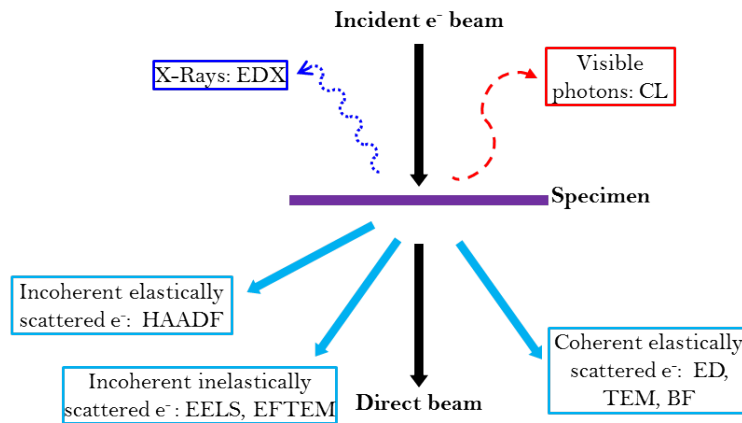
Figure 2.4: Different signals emerging when a coherent electron beam crosses a thin specimen and the related techniques.

Working under conditions of convectional TEM, elastically scattered electrons after crossing the specimen interfere to create a contrast phase image. Therefore, the observed contrast in a TEM image is a consequence of the phase difference among the contributing scattered electrons. The obtained interference patterns gives us lattice information, but the observed fringes are not direct images of the structure. Since the phase contrast is affected by many factors, such as the sample thickness, orientation, variations in focus or astigmatism, the resulting images are hard to interpret, and getting a complete understanding is only achievable by comparing with computer simulations.

STEM related techniques are based on focusing the electron beam into a small probe which is scanned over the sample, leading to multiple signals. By gathering those electrons elastically scattered, several imaging techniques can be performed, as we described in section 2.3.1. In contrast, the processes related to energy losses give rise to spectro-

scopies, either by direct measuring the lost energy by the incident electrons (electron energy-lost spectroscopy, EELS) or by secondary signals emerging as consequence (X-rays, photons, etc), as explained in section 2.3.2. Nicely, the resolution improvement and intensity enhancement provided by the aberration correctors allows the performance of many of these techniques at atomic resolution.

2.3.1   Imaging Individual Atoms: HAADF and ABF

Annular detectors were firstly designed to be combined with spectrometers: while the annular detector gathered the elastically scattered electrons, the spectrometer collected the inelastically scattered ones. Such set up allowed Crewe and co-workers obtaining the first annular dark field (ADF) reported image (1970) [66], though referred as elastic dark field.

The employment of annular detectors in STEM mode is nowadays a common practice, and the different imaging techniques when operating a TEM in scanning mode (or a dedicated STEM instrument) can be classified attending to the angle range of collected scattered electrons. The angular distribution of the scattered electrons is related to the suffered interactions with the specimen, giving distinct information as function of the considered angular range.

For instance, those electrons scattered at high angles are mainly elastically dispersed by interaction with phonons, via Thermal Diffuse Scattering (TDS). Consequently, placing an annular detector at the high angle scattering region, where the arriving electrons have suffered an analogous process to the Rutherford scattering, allows their incoherent interference to produce high angle annular dark field (HAADF) images. The main difference respect to ADF is the negligible contribution of Bragg diffracted beams to the image, still relevant in ADF conditions, by increasing the inner collection angle. In this way, the diffraction contrast contribution to the image formation under ADF conditions is suppressed. The most prominent advantage of the HAADF technique is that it provides chemical information, meaning that the observed contrast scales with the atomic number of the analyzed constituents reason why it is so called Z-contrast. For qualitative purposes it is usually assumed a squared dependence of the contrast (or signal intensity, I) with the atomic number, Z ($I \propto Z^2$). However, the exact exponential factor, α, is slightly smaller, ranging from 1.2 to 1.8 as function of the actual collection angle [67]. The experimental dependence of α with the inner collection angle, θ is illustrated in Fig. 2.5, and it can be described by equation 2.9 (where A and B are the fitting parameters).
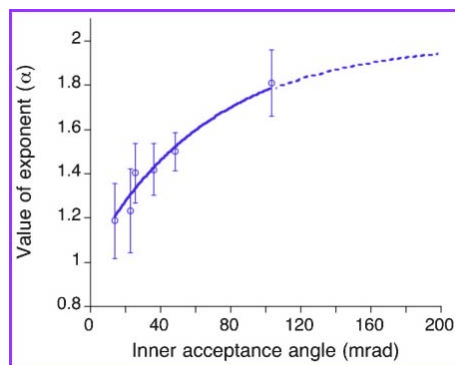
$$\alpha = 2 - Ae^{B\theta} \tag{2.9}$$

Figure 2.5: Dependence of the Z exponent, α, with the inner collection angle of the ADF detector. Adapted from ref. [67].

The resulting HAADF images can be mathematically described as the convolution of the illuminating probe, $P(r)$, and an object function representing the specimen, $O(r)$,

$$I_{incoher}(r) = P_{(r)}^2 \otimes O(r) \tag{2.10}$$

In contrast, for HRTEM and BF conditions, due to the coherently nature of the interference, there is a permanent phase relationship between the different scattered electrons interfering, and the coherent intensity can be expressed as follows,

$$I_{coher} = |P(r) \otimes \phi(r)|^2, \tag{2.11}$$

where $\phi(r)$ is the specimen transmission function.

Another remarkable advantage of the HAADF technique is its robustness against contrast reversals caused by small defocus [68], thickness variations or strain effects due to the inherent incoherent nature, contrary to convectional TEM (where the waves interference is coherent). All together, along with the introduction of spherical aberration correctors, that makes possible forming electron probes of sub-angstrom dimensions with increased beam intensity and, thus, enhancing the signal-to-noise ratio, results in an atomic resolution technique with chemical contrast. Accordingly, the elemental constituents within a material can be identified if the sample is properly oriented along any zone axis where the resulting projected atomic columns only contain one of the constituents. In order to proceed with the assignment, an easy strategy to follow is extracting the intensity of individual atomic columns integrated over their diameter. This is highly useful for the polarity analyses reported in Chapter 2, where we take intensity profiles across individual dumbbell pairs and correlate the peaks intensity with the Z of the constituents. You will note there that elements differing only in two protons; i.e., Ga

and As ($Z_{Ga} = 31, Z_{As} = 33$) or In and Sb ($Z_{In} = 49, Z_{Sb} = 51$), can be distinguished by using this technique.
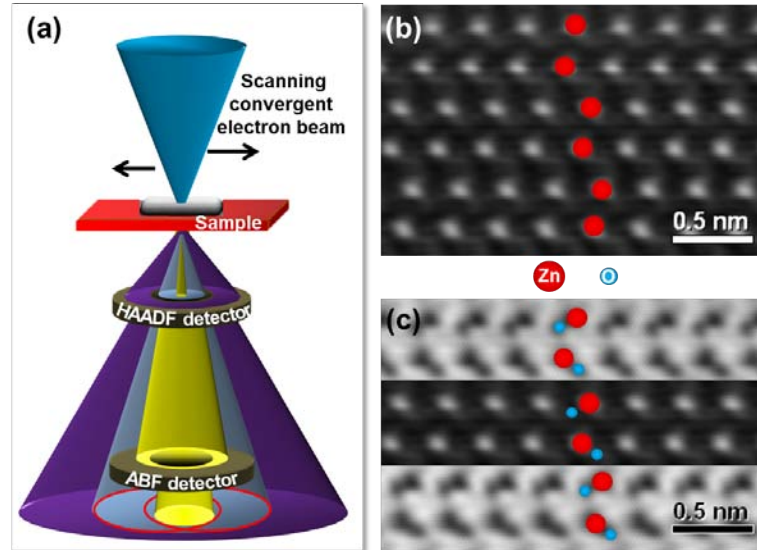

Figure 2.6: (a) Schematic representation of the set up employ for HAADF and ABF imaging . This panel has been adapted from ref. [69] (b) HAADF image of ZnO where only Zn columns are visible. (c) ABF image acquire simultaneously than (b) and at the exact same area.

Unfortunately, the Z dependence of the technique makes the lightest atoms, with weak scattering power, hardly detectable, especially whenever they are combined with heavier ones. This fact is clearly illustrated in Fig. 2.6(b), where an HAADF image of ZnO is displayed, but only the heavier Zn ($Z_{Zn} = 30$) columns are visible while the much lighter O ($Z_O = 8$) are missing. Thus, a more suitable angular range, avoiding the TDS contribution, should be set for the light element visualization. Such range is comprised within the bright field region, but avoiding the unscattered electrons thanks to the use of an annular detector. In fact, the preferred conditions to visualize light elements rely on phase contrast imaging rather than in amplitude contrast. This technique is known as Annular Bright Field, ABF [70], and allows the simultaneous visualization of both, light and heavy atomic columns (see the ABF in Fig. 2.6(c) corresponding to the same region than (b)). In this case, the atomic positions appear as darker features on a bright background, in contrast to the HAADF. The experimental set up (shown in Fig. 2.6) uses either a beam stopper blanking the center of the BF region or an annular detector placed at the adequate angular range by adjusting the camera length [71, 72] to place the detector at the 11-22 mrad angular range. The experimental conditions used along this work, exceed the upper limit of 22 mrad (reaching roughly 60 mrad), but we are still within the region dominated by the coherent interference of elastically scattered electrons, and the light element position is strongly enhanced. Moreover, this factor is

included in the image simulations performed. Anyhow, reaching the ABF conditions in an aberration corrected equipment allows even the visualization of H atomic columns, as reported elsewhere [70].

Note that coherence effects are not negligible under this imaging conditions, implying that the image is only directly interpretable in a narrow range of focus values. Nevertheless, as the HAADF image can be simultaneously acquired over the exact same area, and it will only reflect the heavier constituents localization, the direct comparison between both allows the atomic identification [73].

Moreover, other collection angles can be considered providing further information. For instance, gathering those electrons scattered within the lower limit of the ADF imaging the lattice distortions are enhanced, allowing the detection of strained regions and facilitating the localization of crystalline defects [74, 75]. In addition, this technique, known as low angle annular dark field (LAADF), allows a better visualization of the light elements compared to the HAADF, as we will show in Section 2.4. Another interesting STEM related technique has been developed by collecting those electrons scattered within the bright field region, but limited to an intermediate angular range and, therefore, called middle angle bright field (MABF). The technique provides a compromise between the collection of on-axis electrons, intimately related to the light constituents and the higher angular range within the BF region, which is more related to the heavier ones. Thus, MABF, with an angular limit of 9.4 nm, has been reported to allow the simultaneous detection of both, light and heavy constituents, distinguishable by their contrast [76, 77]. Examples of experimental applications of these techniques to the especial case of nanowires can be found elsewhere [78].

As we have seen above, depending on the detector used (annular or solid) and the final collection angle (inner and outer), we can precisely determine which contrasts to enhance in the atomic imaging. Therefore, there is room for improving STEM techniques, for instance, by developing digital pixeled detectors, able to record simultaneously the whole set of collection angles experimentally achievable. The later data manipulation should allow the digital selection of the desired collection angles to create the image (ex-situ), representing a revolutionary advance in STEM.

2.3.2   Spectroscopies: EDX, EELS and CL

The electron energy transfer while crossing the sample leads to the emergence of many useful signals. Different processes may be related to the inelastic scattering, leading to a variety of spectroscopic techniques. In addition to the energy lost by the illuminating electrons, other related signals, as the emerging X-rays or photon emission can be

detected giving valuable information. Along this section, we give an overview of the spectroscopies related to the three signals.

Importantly, performing spectroscopic techniques, one spectrum will be recorded at every pixel as we scan the electron probe over the specimen. Hence, the set of obtained results is know as data cube. Three different sort of experiments are possible, based on the number of spatial dimensions analyzed within an energy range: punctual analyses, line scans or 2D maps. Moreover, the arrangement of the detectors in the instrument permits acquiring the ADF image simultaneously, giving the exact location where the spectra has been obtained.

Energy Dispersive X-Ray Spectroscopy, EDX

The large energy of the electrons crossing the sample in a electron microscope makes possible their penetration into the inner-shell of electrons (deeper than the conduction/valence outer bands) surrounding the atomic nucleus of the sample constituents. If one of those inner electrons is ejected during the interaction, a hole will be created there and the atom loosing the electron will be ionized and, thus, in an excited state. The energy required to expel the electron is that lost by the scattered electron. In the transition back to the ground state, the hole will be filled with an outer electron, involving the emission of an X-ray or Auger electron. As the energy of the emission is the difference in energy of the electron initial and final states (from the outer shell energy to the inner one), it is characteristic of each element.

Many transitions are possible depending on the initial and final energy levels involved. Therefore, the transitions are named accordingly to the shell that is being filled and the shell from which the electron comes. The nomenclature is based on the classical atom description introduced by Bohr, in which the electrons are distributed within different concentric levels around the nucleus. The different electronic shells are labeled as K, L, M, etc., from the atomic nuclei outwards, and this terminology is used to refer the filling level. Some edges are identified in the EDX spectrum included in Fig. 2.7, corresponding to a InAs nanowire. Greek alphabet is used to indicate the initial electron state referred to the final one. Thus, α is used if the incoming electron arrives from an immediately higher energy shell (e.g., L $\rightarrow$ K, M $\rightarrow$ L), β for those electrons coming from two shells above (e.g., M $\rightarrow$ K, N $\rightarrow$ L), etc. Moreover, as the shells are split into differentiated subshells, the departure subshell can be included in the notation as a number subindex.

Unfortunately, the lighter elements posing only one (partially/) filled shell cannot be analyzed by the technique, imposing its main limitation. The newer microscopes,
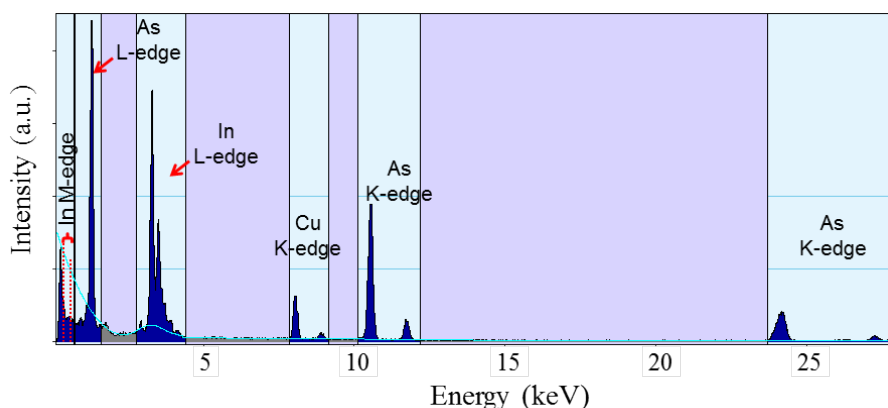
Figure 2.7: InAs EDX spectrum where the different edges are indicated. The Cu signal detected is due to the TEM copper grid.

equipped with probe correctors and the latest generation EDX detectors are capable of getting EDX spectra at atomic resolution. These new devices combine several detectors simultaneously providing larger collection angles. Moreover, the increased collection efficiency allows much faster acquisitions with enhanced signal-to-noise ratio, highly useful for beam sensitive samples.

Electron Energy-Loss Spectroscopy, EELS

The detection of those electrons undergoing inelastic interactions with the specimen is another valuable source of chemical information. The separation of the electrons accordingly to their kinetic energy after crossing the specimen, give rise to electron energy-loss spectra.

EEL spectra are classically divided into two separated regions, the low-loss and the core-loss. The low-loss region extends until energy losses of about 40 eV, including unscattered electrons, elastically scattered ones, electron-phonon interactions and those regarding the outer-shell electrons. At the lower energy limit of the spectra, there is the zero-loss peak, accounting for all the elastic events occurring. This peak is much more strong than any other peak appearing in the spectra. The core-loss comprises the energy range from 40 eV on, and it represents the inner-shell excitations; i.e., the interactions of the electron beam with the inner (or core) electrons. The recorded spectra within this energy range will contain the ionization edges of the constituents, showing a sharp rise at the binding energy of the electronic transition involved, and thus, characteristic of the excited element. A complete description of the technique, physical principles, applications and instrumentation can be found elsewhere [79].
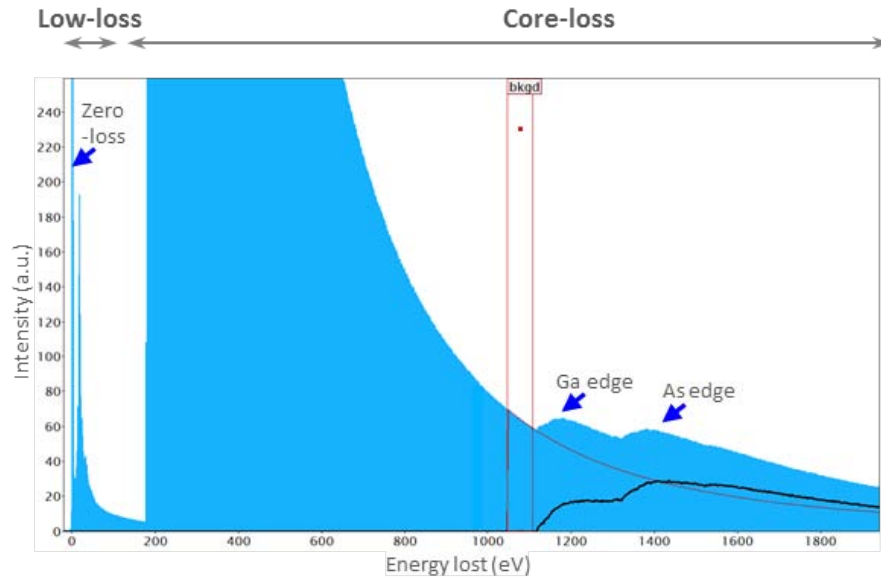
Figure 2.8: EEL spectrum of GaAs. The core-loss region has been magnified by a factor of 50.

In addition to elemental mapping, many useful information can be extracted from the fine structure (shape) of the edges, if performing the technique with enough energy resolution. The actual state-of-the-art achieved thanks to the implementation of monochromators and aberration-corrected probes, reaches the mapping of electronic-state-related properties, such us oxidation state [80], bonding [81, 82] or coordination geometry [83]. Moreover, many advances have been done during the last years within the low-loss region, regarding plasmonic analyses that has become a hot topic in the field of materials science [84, 85].

Cathodoluminescence, CL

Cathodoluminsencence (CL) is an spectroscopic technique regarding the photon emission (visible light) as consequence of electronic excitations. The creation of electron-hole pairs in semiconductors, promoted by the accelerated electrons when crossing the specimen, may result in the recombination process, involving photon emission with energy equal to the band gap. Therefore, the optical properties of semiconductors can be investigated by collecting and recording the emitted photons.

The electronic excitation is commonly induced by the electron probe in scanning electron microscopes (CL-SEM) or, nowadays, in scanning transmission electron microscopes (CL-STEM). The incorporation of CL detectors into (S)TEM equipments improves the spatial resolution thanks to the smaller electron probes with higher energies. Importantly, ADF imaging and EDX analyses can be simultaneously conducted

within the exact same area while performing the CL measurements, resulting in data sets with structural, compositional and optical information.
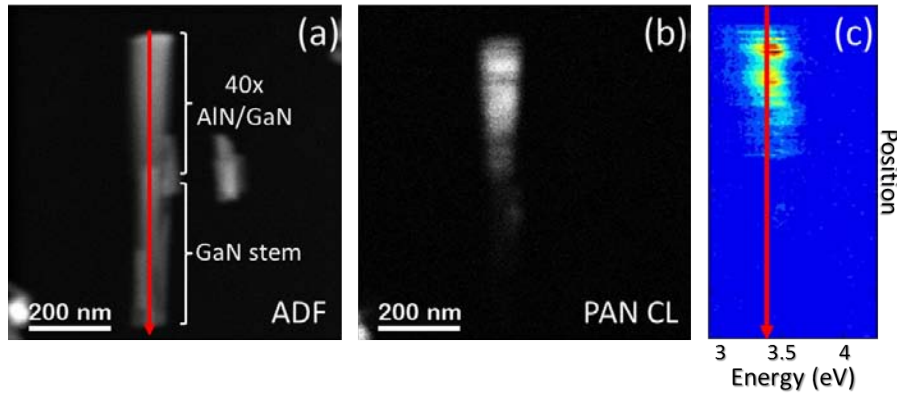

Figure 2.9: Panchromatic spectrum (b) of a GaN NW containing a 40 period AlN/GaN axial superstructure., as indicated in the ADF image in (a). The acquired CL profile along the length of the structure, following the red arrow ,within the energy range of interest is displayed in (c) .

Two main sort of spectra are possible, depending on the spreading of recorded energies. Collecting any photon emitted will lead to panchromatic images, useful, for instance, to identify the emitting areas. Alternatively, a thin energy range of few electron volts can be mapped, pointing the actual band gap of the analyzed material. Examples of both type of CL spectra performed on an individual GaN NW containing 40 GaN insertions spaced by AlN barriers, can be seen in Fig. 2.9.

2.4   Strain Measurements

2.4.1   Strain Measurements: GPA and PPA

In order to analyze the lattice distortions, as those induced by lattice mismatch, we analyze the materials under high resolution conditions. This is done either by conventional HRTEM or by aberration-corrected HAADF techniques, since the only requirement on the image is the presence of Bragg spots in the Fourier transform (therefore, lattice fringes should be visible at the micrographs). Different algorithms have been developed to account for the presence of strain within a crystallographic phase, some working on the Fourier space and some other directly analyzing the real space.

Geometric Phase Analyses, GPA
By studying the reciprocal space, useful information can be extracted from the phase variations. Based on the analysis of the phase modifications across the field of view of any frequency at the reciprocal space, a direct relationship with the presence of stain
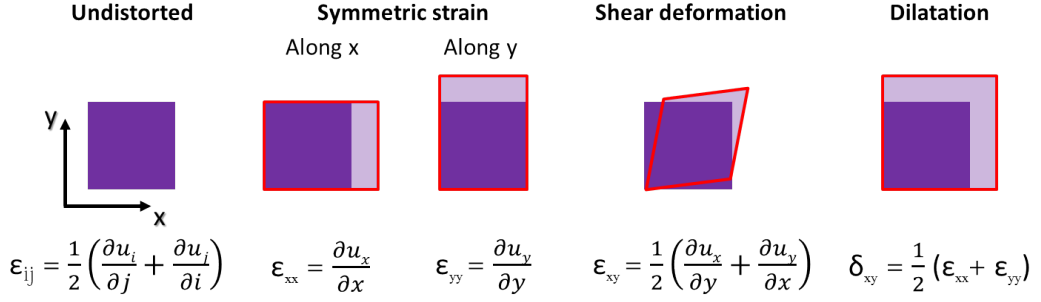
Figure 2.10: Commonly observed lattice deformation along with their mathematical expressions (below). $\vec{u}$ is the displacement field, related to the phase through the expression 2.12.

fields can be inferred, establishing the basic principles of the Geometric Phase Analysis (GPA) [86]. By choosing any frequency or reciprocal lattice vector, **g**, at the Fourier transform of a micrograph, we can obtain the phase image, $P_g(r)$, which corresponds to the position of lattice fringes at the same image. This phase is directly related to the displacement field, **u** as follows:

$$P_g\left(\vec{r}\right) = -2\pi \, \vec{g}\,\vec{u} \tag{2.12}$$

giving the displacement field related to the selected **g** vector. Two non-colinear reciprocal lattice vectors allow the calculation of 2D displacement fields, which gradients will give the local distortions of the lattice along the different coordinates considered, x and y (eq. 2.13). Some of the resulting deformations are graphically illustrated along with their mathematical expressions in Fig. 2.10.

$$\epsilon_{ij} = \frac{1}{2}\left(\frac{\partial u_i}{\partial j} + \frac{\partial u_j}{\partial i}\right) \tag{2.13}$$

Selecting only one lattice vector, **g**, we can analyze its deformation referred to an undistorted area, in terms of the fringe spacing (dilatation maps, accounting for positive and negative dilatations) and the plane rotation, as summarizes Fig. 2.11. The high resolution image in (a) shows the interface between $InAs_{1-x}Sb_x$ (bottom) and InSb (top) lattices, both crystallizing in the cubic $F\bar{4}3m$ space group. The $(\bar{1}11)$ frequency on the power spectra included in (b) is decomposed into amplitude and phase, displayed in (c) and (d) respectively, allowing the additional separation of the phase in terms of the lattice spacing (e) and plane rotation (f).

Peak Pairs Analyses, PPA

Algorithms working on the real space, as Peak Pairs Analyses (PPA), firstly construct
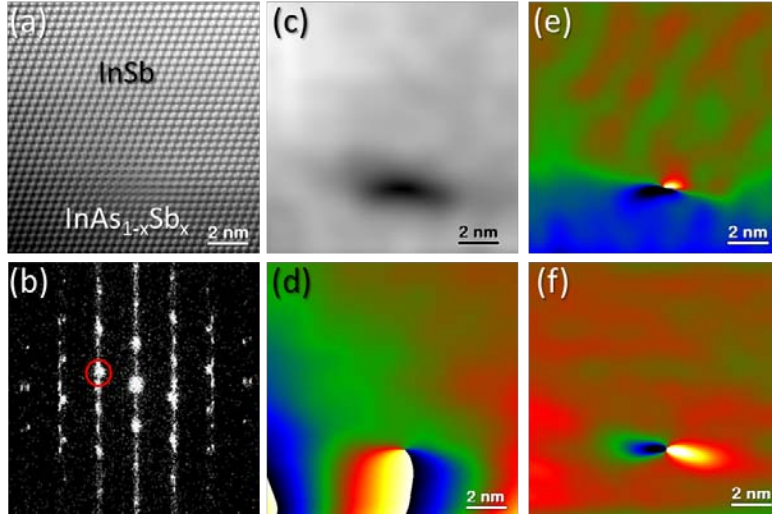
Figure 2.11: High resolution image of the interface between $InAs_{1-x}Sb_x$ and InSb epitaxial layers. (b) Power spectra or Fourier Transform of the image in (a). The selected g vector for the lattice deformation analysis, $(\bar{1}11)$, is red encircled. (c,d) Amplitude and phase images of the $(\bar{1}11)$ reflection within the area shown in (a). (e,f) Dilatation and rotation maps of the analyzed **g** vector.

the Bragg filtered image, by properly masking the desirable reflections on the power spectra. The next step consists on finding the local intensity maxima within the filtered image, corresponding to the atomic column position (see Fig. 2.12(c)). Then, paired peaks are established between neighbor maxima, following the direction of the basis vectors already determined. The basis vectors, $\vec{a}$ and $\vec{b}$, are set as the two first reflections selected before obtaining the Bragg filtered image, if working with the commercial PPA package. Note that, in order to obtain a 2 vector basis, non-collinear reflections must be chosen (g_1 and g_2 in Fig. 2.12(b)). During the process, both vectors are decomposed in x and y components, to later referred the deformations. Within the obtained net of paired peaks it is possible to evaluate their displacement from the ideal positions (in terms of the Cartesian components of the vector base, a_x, a_y, b_x and b_y), giving a precise estimation of the strain field after choosing a suitable undistorted reference area [87].

Examples of displacement and strain maps obtained by using PPA around a grain boundary in an InAs membrane are shown in Fig. 2.12(d,e). The InAs is mainly composed of wurtzite phase, seen along the $[11\bar{2}0]$, but highly twinned. The reference area has been placed at a pure wurtzite region (more details about twinning phenomena and polytypism are given in Section 3.1). Therefore, the presence of twin boundaries altering the stacking sequence are reflected on the maps. Also the two different domains and the merging boundary (the discussion about the present membrane is fully detailed in the corresponding results section, 4.3).
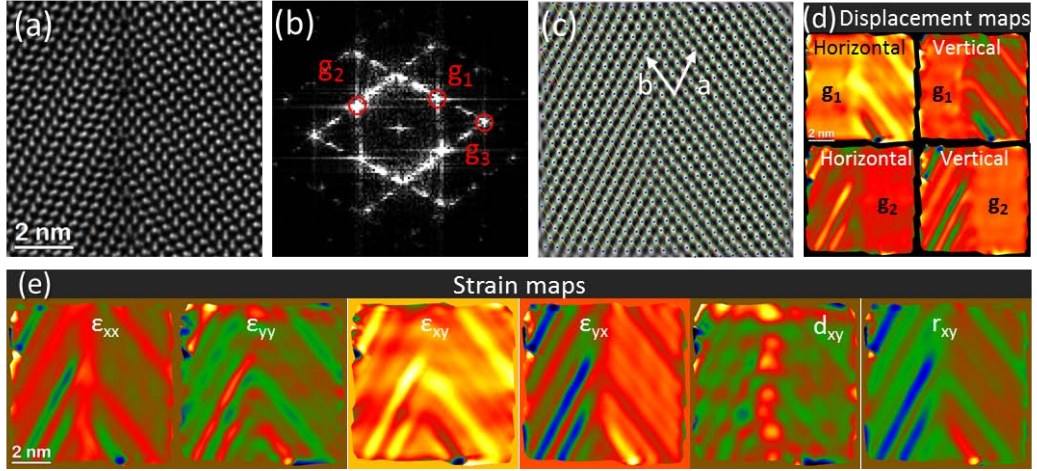
Figure 2.12: (a) Atomic resolution HAADF image of a grain boundary in an InAs membrane. (b) Power spectra indicating the selected reflections to be filtered, resulting in (c). Note that g_1 and g_2 correspond to $\vec{a}$ and $\vec{b}$, respectively. (d) Displacement maps of $\vec{a}$ (top) and $\vec{b}$ (bottom) along the horizontal (left) and vertical (right), directions. (e) Different strain maps, dilatation (d_{xy}) and rotation (r_{xy}).

2.5 Image Simulation, Image Improvement and 3D Atomic Models

The proper contrast interpretation of a coherent image always requires computer simulation, reason why HRTEM simulations have become a routine. In the case of HAADF images, even though the contrast is usually directly interpretable, there are some especial cases where a deep understanding requires computer simulations, too.

Computer simulation methods rely either on the Bloch wave formalism or in multislice routines. The former consider the individual probe interaction with every atomic column, approximated as "s "states. The later, perform mathematically slicing of the specimen and account for the successive interactions of the electron beam with the different slices. In these cases, the projected potential at each slice can be describe by different approximations, such as the absorptive potential or the frozen phonon (or frozen lattice). In order to introduce the TDS contribution and, thus, getting more realistic HAADF simulations, it is possible to "frozen "the thermal vibration of the lattice by averaging random atomic displacements, i.e., different frozen lattice configurations are averaged.

The image simulations presented in this manuscript are calculated by using STEM_CELL software package [88]. Free available, the software is based on the frozen phonon routines developed by Kirkland [89] for the image simulation, while it also includes many tools for the manipulation of the experimental data and the creation of atomic models

as input for the simulations. The program allows to calculate simplified simulations by convolving the squared probe with the atomic potential. The resulting images predict qualitatively the experimental intensity, although they do not account for channeling effects. In addition, the program offers the possibility of including the source size effects, S(r), related to the incoherent contribution while forming the probe, and which blur the image. The size effects are described by a Gaussian function term with customized σ within the mathematical expression for the intensity:

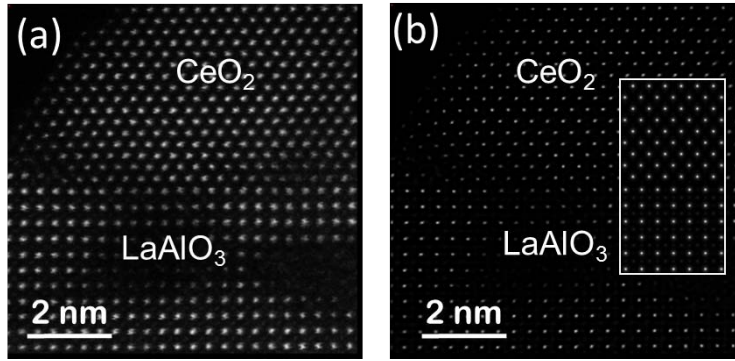$$I\left(r\right) = P_{(r)}^2 \otimes O\left(r\right) \otimes S_{(r)} \tag{2.14}$$

Figure 2.13: The experimental HAADF image of the interface between a CeO_2 nanoisland and the $LaAlO_3$ substrate (a). After filtering the noise by a Wiener filter and deconvolving the probe, including source size effects, by 50 iterations, the simulated image (inset) is almost indistinguishable from the treated image (b).

One of the greatest advantage of the software is the image improvement offered. The concept is the same than for simulated images but calculating the other way around. Hence, instead of convolving the probe and object function, it is possible to deconvolve the experimental image, also accounting for the source size effects. A previous step of filtering the image (Wiener filter) to get rid off the environmental noise is usually required. Proceeding as mentioned a really good agreement between the experiment and simulations is achieved. For instance, in Fig. 2.13 the experimental HAADF image of the heterointerface between a CeO_2 nanoisland (top) and the employed $LaAlO_3$ substrate in (a) is firstly Wiener filtered, and then, the probe and source size effects are deconvolved, resulting in the image shown in (b). Note the good agreement between the simulated image, included as inset overlapping the treated image in (b).

The versatility of the software allows the simulation of different (S)TEM techniques, just by setting the proper experimental parameters. As an example, Fig. 2.14 includes STEM simulated images of the $LaAlO_3/CeO_2$ interface (as illustrates the bottom
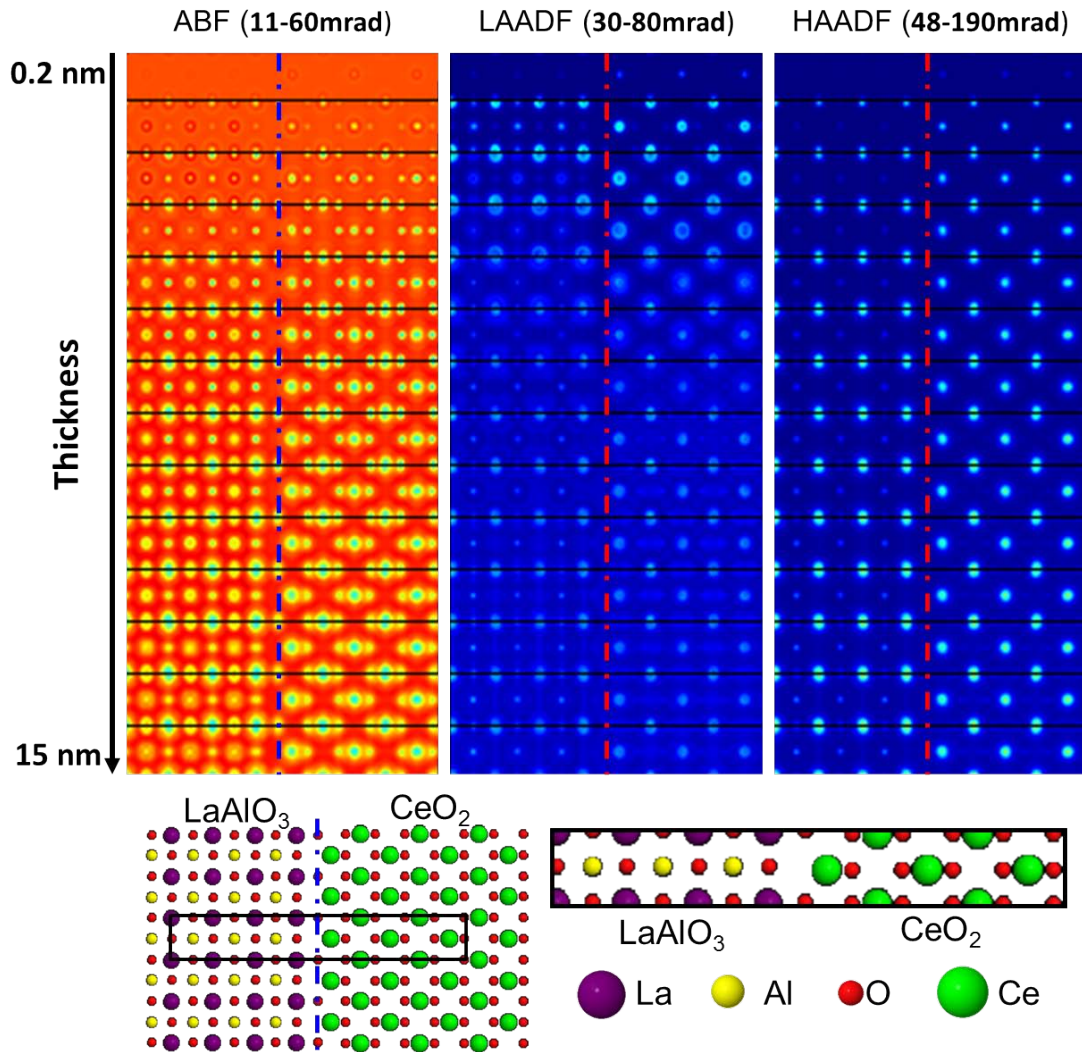
Figure 2.14: STEM simulated images of the $LaAlO_3/CeO_2$ interface shown at the bottom. The sample thickness increases from 0.2 nm at the top to 15 nm at the bottom. The collection angles considered reproduce the ABF, LAADF and HAADF experimental conditions.

model), extending over a wide range of detector angles and thicknesses. The considered collection angles are those corresponding to the ABF, LAADF and HAADF experimental conditions, highly useful for checking the expected O visibility with the different techniques.

It may be noted that the simulations are calculated from previously built atomic models, also called supercells. We create our atomic 3D models by means of Rhodius [90], an on-line software that allows the creation of complex structures with the desired faceting, composed of one of several phases. The crystallographic phases should be introduced in advanced by the *Eje-Z* package, developed by the same group at Universidad de Cádiz (UCA).

2.6   Equipments Employed

The STEM atomic resolution images presented along this manuscript have been obtained in a FEI Titan (60-300 kV) operated at 300 kV and equipped with a third order probe-aberration corrector, a monochromator and an X-field emission gun (X-FEG), which is located at the *Laboratorio de Microscopias Avanzadas, Instituto de Nanociencia de Aragon*. The HAADF imaging was performed by setting the camera length at 128 mm, leading to inner and outer collection angles of 48 and 241 mrad, while for the ABF imaging we have used a nominal camera length of 160 mm, resulting in an collection angular range of 11-60 mrad, as already mentioned in Section 2.3.1; which are the values considered in the simulations. The microscope is further equipped with a Gatan Energy Filter Tridiem 866 ERS which has been used for the EELS measurements. For that goal, we employed the shorter camera length (10 mm) and the most convenient energy dispersion (between 0.5 and 1.0 eV), aperture and exposure time for every experiment.

The supplementary analyses performed by means of HRTEM have been conducted either in a Jeol J2010F, located in the *Serveis cientificotècnics, Universitat de Barcelona*, or in a FEI Tecnai F20, installed at the *Institut Català de Nanociència i Nanotecnologia*, both equipped with field emission guns and operated at 200 kV.

The CL-STEM measurements presented in Chapter 6 have been carried out in a Jeol 2011 TEM/STEM equipped with a Gatan MonoCL3 CL+ system (consisting of a retractable collection mirror and a light guide, a monochromator, and photodetectors), located at the *Massachusetts Institute of Technology*. Those experiments were performed by Xiang Zhou and Aziz Genç, within the framework of a collaboration between our group and the *Laboratory for Nanophotonics and Electronics*, headed by Prof. S. Gradečak.

Polarity Determination and Polar Growth Mechanisms

3.1 Introduction

The charge transfer between constituents in ionic crystals, leads to the formation of atomic couples where the constituents are oppositely charged. As a consequence, the internal electric fields emerging cause the approaching of atomic columns. This fact induces the creation of dipole-like arrangements, that can be seen along certain directions as atomic pairs or dumbbells. In binary compounds; i.e., AB, depending on the dumbbell orientation along a certain direction (mainly the growth one) the material is said to have A or B polarity, influencing their growth and properties.

Most known and employed semiconductor materials crystallize either in the cubic Zinc-Blende (ZB) structure, belonging to the $F\bar{4}3m$ space group, or in the hexagonal Wurtzite (WZ) [91] with $P6_3mc$ space group (both included in Fig. 3.1). Both phases can be thought in terms of closed-packed structures, with a cationic/anionic cubic close-packed or faced-centered packed (ffc) lattice for the ZB, and hexagonal closed-packed (hcp) lattice for the WZ; where half of the tetragonal positions are occupied by the anions/cations. Thus, every A (B) atom within the lattice is surrounded by 4 B (A) atoms in a tetrahedral coordination geometry.
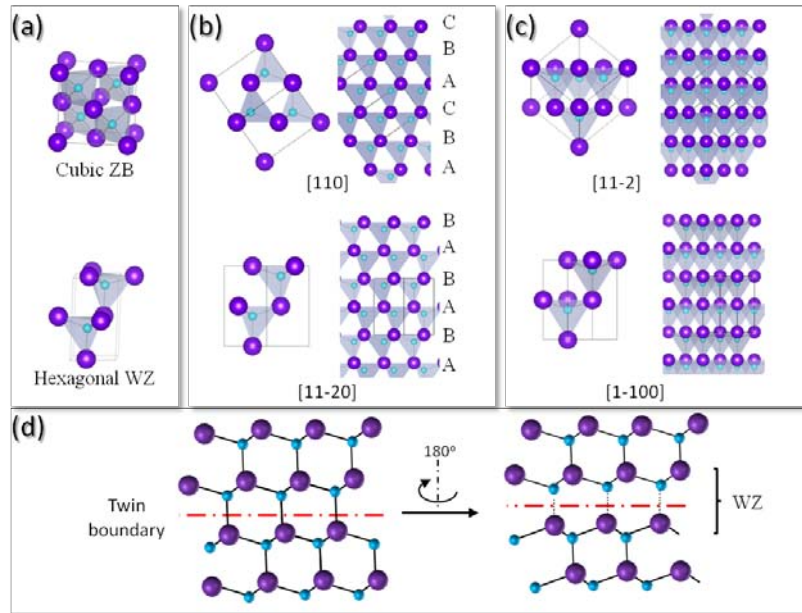
Figure 3.1: (a) Unit cells for the cubic ZB (top) and hexagonal WZ (bottom) phases. (b) 2D projections of the ZB (top) and WZ (bottom) along the [110] and [11$\bar{2}$0] zone axes for the ZB and WZ, respectively. (c) 2D crystal projections along the [11$\bar{2}$] and [1$\bar{1}$00] for ZB (top) and WZ (bottom). (d) Pristine ZB structure (left hand) and twinned ZB (right hand), where the twin boundary is equivalent to a monolayer of WZ.

Despite the symmetrical differences dictated by the different space groups of both

structures, they are quite similar if comparing the growth along one of the $\langle 111 \rangle$ directions in the ZB with the growth along the $\langle 0001 \rangle$ direction in the WZ. Under this consideration both structures are only distinguishable by the bilayer stacking sequence along the growth direction, being $...ABCABC...$ and $...ABABAB...$ for ZB and WZ, respectively. It is especially useful imaging the crystallographic phases along the [110] direction (or, equivalently [$11\bar{2}0$], for the hexagonal phase) where the assignment of the stacking sequence can be unequivocally done. Moreover, this zone axis provides the best direction for visualizing the dumbbells, as shown in Fig. 3.1(b). Other zone axes, as the normal directions to the ones already presented, i.e., the [$11\bar{2}$] for ZB or [$1\bar{1}00$] for WZ, lead to equivalent 2D projections for the ZB and WZ lattices (Fig. 3.1) and the dumbbells constituents appear closer to each other. It can be easily deduced for the ZB phase that dumbbells seen along the [110] direction are $\frac{a_{ZB}}{4}$ apart, corresponding to the (004) interplane distance; whereas along the [$11\bar{2}$] the constituents are seen $\frac{a_{ZB}}{4\sqrt{3}}$ spaced, equivalent to the (444) plane spacing. Considering for instance the GaAs ZB phase, with a $a_{ZB} = 5.6535$ Å, the observed distance between Ga and As within a dumbbell is 1.41 Å along the [110] projection while it is just 0.816 Å along the [$11\bar{2}0$].

These structures are prone to the presence of twin boundaries, which are planar defects involving a lattice rotation of 180º, either perpendicular or around its normal vector. The twin boundaries can be classified into two different types, known as paratwins and orthotwins [92], depending on whether the rotation is around the twin plane (paratwins or mirror twins) or perpendicular to it (orthotwins or rotational twins). Note that both types of twin boundaries are indistinguishable in centrosymmetric crystals, as Si or Ge (with $F\bar{4}3m$ space group), while they have different implications in non-centrosymmetric structures(i.e., partially ionic AB compounds): whereas orthotwins rotate the lattice but preserve the orientation across the boundary and thus, the polarity; paratwins also reverse the lattice orientation, inverting the polarity across the defect. Such polarity inversion involves either A-A boding or B-B bonding, but anyhow strongly modifying the local environment of the atoms around the twin plane, being thermodynamically much less favorable than the orthotwins. Due to the lattice rotation promoted by the twins, the atomic stacking sequence is modified with respect to the pristine phase, creating local domains of one phase inside the other [93]. Lots of intermediated polytypes between the purely cubic ZB and hexagonal WZ have been reported for some materials as silicon carbide [94], but all of them can be understood as ZB or WZ phases where presence of systematic twin boundaries alter the lattice periodicity to produce a crystallographic phase in between the cubic and the hexagonal. However, the phase purity can be achieved by tailoring basic growth parameters [95] and the controlled introduction of these defects can be used to create quantum structures. For instance, taking advantage of the different band alignments of both phases allows

the carriers confinement [96], and leads to the formation of polytypic and twinning su-
perlattices [9, 97–100].

If neglecting any further distortion of the lattices, and only based on geometrical
factors, the WZ lattice constants a_{WZ} and c can be derived from the bulk ZB constant,
a_{ZB}, as follows:

$$a_{WZ} = \frac{a_{ZB}}{\sqrt{2}} \qquad and \qquad c = a_{ZB}\frac{2}{\sqrt{3}} \qquad (3.1)$$

However, these geometrical relationships underestimate the effect of the hexagonal
symmetry vs the cubic on the bonds that leads to tetrahedral distortions, changing the
final lattice parameters since both, in plane and out-of-plane interatomic distances are
modified [101]. The c/a ratio can be used to estimate the strength of such deviation,
which ideally should reach a value of $\sqrt{\frac{8}{3}}$. In fact, these fluctuations induce the for-
mation of non-compensated dipole moments resulting in spontaneous polarization, that
gives rise to the appearance of internal electric fields, the so-called quantum confinement
Stark effect (QCSE) and the piezoelectric behavior.

It must be pointed out that the lack of inversion symmetry in these systems turns
them into polar materials, meaning that they show polar planes where their orientation
becomes relevant. For instance, it is known that the same surface plane with opposite
polarities show really different chemical behaviors [102–105]. Moreover, a polarity de-
pendence on the optoelectronic properties can be addressed. For example, it has been
shown that, in InGaN/GaN quantum wells (QWs), the carrier localization and trans-
port are dependent on the polarity [106].

Remarkably important is also the polarity preservation or its inversion within a
structure, as we will see along Section 4.3. There, it is shown the effect of a polarity
reversal on the transport properties of a nanostructure. It should be mentioned that
to the best of our knowledge, no polarity inversions within pure binary NWs have been
reported. However, polar interfaces with polarity inversion have been observed for NW
heterostructures such as GaN/ZnO NWs [41].

Linked to the different polar behaviors arises the question of whether the polarity
drives the growth or the growth induces a certain polarity. For most III-V and II-IV bi-
nary systems it turns out that the non-planar growth at the nanoscale is highly favored
by a certain polarity. But, until date, a comprehensive study on the polar character
of the most used binary compound NWs is missing. Moreover, a great controversy has

emerged around this issue since despite the trend of almost every binary combination to grow along B-polar directions, discrepancies can be found in few systems [107, 108]. Even though there is a huge bibliography regarding the matter for certain materials, it is hard to establish a systematic comparison due to the many factors affecting the growth. This is partially due to the variety of growth techniques available to produce NWs, including chemical and physical methods, each of them requiring the proper environmental conditions for the growth to succeed. Thus, different substrates, temperatures, fluxes, precursors, doping, catalyst, etc. are involved, and relating their influence to the material polarity is not straightforward.

As we have seen, polarity is an intrinsic property in semiconductor binary systems that may have a great importance on the final performance and properties of the obtained nanomaterials. However, there is a lack of a reliable technique in order to measure it with high precision down to the atomic scale. Until now, several procedures have been established in order to address the polarity in binary compounds.

The simplest approach is known as homoepitaxy, and it is based on the assumption that the substrate polarity is transferred to the growing structure [58, 109–111]. Unfortunately, such procedure can be employed only when working with polar substrates while is useless when using amorphous or non polar ones; and it is insensitive to any polarity inversion at the interface.

A more reliable way to assign the polarity consists on the surface characterization by means of scanning tunnel microscopy (STM) [112], after cleaning or cleaving the sample. This imposes a huge drawback in the case of NWs, which have to be deposited on a conductive substrate or embedded in a matrix for the later cleavage of the substrate in situ [113–115]. In addition to the possible structural damage during cleaving, shorter dumbbells can not be resolved and light elements are invisible to the technique.

Moving to TEM related techniques, spectroscopy measurements are nowadays possible at atomic resolution using either EELS [116, 117] or EDX [118], both performed in scanning mode (STEM). Also, for some materials such as GaN, under channeling-enhanced EELS conditions, the fine structure of the spectra show distinguishable fingerprints for both, the N-polar and Ga-polar direction, allowing the polarity determination [119]. But, depending on the material composition, some constituents will be hardly detectable depending on the technique (i.e., light elements are easily detected by EELS but not by EDX and also the other way around, heavy metals give poor EELS signals but emit lots of x-rays) and data treatment is non trivial. Moreover, high exposure times can be required, which often damage the samples and sometimes involves drift problems.

Another procedure, maybe the most used for the polarity determination is the convergent beam electron diffraction (CBED). In this case, the assignment is carried out by comparison of the experimental data with simulated diffraction patterns, paying attention to the characteristic features present in both [92, 100, 120]. The main limitation from the sample to apply this technique is the size of the analyzed structure that should be big enough to get an accurate diffraction pattern. In addition, this technique would not allow detecting local polarity inversions at the monolayer level.

Instead of studying the reciprocal space as CBED does, we can directly use HRTEM imaging in suitable TEM samples to achieve the highest resolution possible. Specimens must be thin and flat to minimize undesirable artifacts in the images [121–123], and even so computer simulations are needed for a precise data interpretation.

Alternatively to the use of characterization devoted techniques, it is possible to determine the polarity of a nanostructure by taking advantage of the different chemical behavior of the oppositely polarized surfaces by chemical etching [102]. However, a previous knowledge of the material surface reactivity is needed, the procedure is invasive and again, local polarity inversions would not be detected.

To overcome the already mentioned limitations we established an straightforward procedure for the polarity determination in nanometer size structures such as NWs, making use of different imaging techniques in STEM mode [69]. It is worth to be noted that in STEM mode, signals from different scattering events can be collected simultaneously by a variety of detectors, giving complementary information of a certain area at the same time. Thus, in our approach, we combined HAADF and ABF as complementary techniques at atomic resolution. As mentioned in section 2.3.1, HAADF provides chemical contrast, allowing an easy and fast dumbbell constituent identification, but only for medium-high atomic number elements. For the detection of light elements, especially when they are combined with heavy ones, we proposed the use of the ABF technique that allows the detection of individual atomic columns even for the lightest element in the periodic table, H [70]. Although under ABF conditions the image contrast is not dominated by the chemical attributes of the constituents, the atom identification within the dumbbells can be unequivocally done by comparing the ABF image, showing the entire dumbbell, with the simultaneously acquired HAADF image that only shows the heavier constituents. For more details on the techniques the reader is referred to Section. 2.3.1.

Thus, in the following, we apply this combined procedure, involving HAADF and ABF techniques, to address the polarity in the most common III-V and II-IV binary compounds used to synthesize NWs. Some other non-planar nanostructures are also

investigated along the present and following chapters, allowing depicting the underlying growth mechanisms. The obtained results are compared with previous published data on the topic, opening the discussion on whether the polarity influences the growth or the growth conditions are responsible for the observed polarity. The possible influence of intrinsic phase factors (as, for instance, the ionicity) on the grown polarity is carefully studied and discussed. Examples concerning 2D-like nanostructures are presented in Chapter 4, including non-polar nanostructures and polarity inversion domain boundaries (IDBs).

3.2   Polarity Determination in Binary Semiconductor NWs

We have addressed the polarity in the most commonly used III-V and II-VI binary combinations under the NW morphology by means of aberration-corrected STEM techniques, i.e., combining HAADF and ABF [69]. Although only by using HAADF we are able to study most combinations, the ABF is required in order to analyze the nitrides (AlN, GaN and InN) and oxide (ZnO) related cases, where light atoms are involved (specifically, N and O). The compounds have been synthesized by using different growth techniques. III-V NWs were grown either by metal-organic vapor-phase-epitaxy (MOVPE) or by molecular beam epitaxy (MBE), while the growth is plasma-assisted MBE for the nitrides case (PAMBE). In contrast, II-VI nanostructures were synthesized in a vapor transport system. The temperature and precursor fluxes used during the growth are set to be optimal for each material (higher yield), and suitable substrates are chosen.

Note that all the cases considered consist on NWs epitaxially grown on the substrates, involving mismatch limitations. Although some of the examples here considered have been homoepitaxially grown, the vertical growth of NWs can proceed successfully under large mismatches thanks to their aspect ratio. Their morphology allows releasing laterally the mismatch strain over short distances from the interface, allowing the employment of other substrates, as Silicon. It is worth to mention the beneficial contribution of an amorphous thin layer coating the substrate surface in most cases. For instance, in the case of nitrides, during the plasma-assisted MBE (PAMBE) synthesis, the epitaxial growth takes place mediated by an amorphous Si_xN_y epilayer created on the Si substrate. The absence of such a layer avoids the NWs formation and its presence does not affect the alignment with the underlying Si [124]. Similarly, the GaAs NW growth is also mediated by the presence of an amorphous SiO_2 layer, allowing the epitaxy with the underlaying substrate if the oxide is thin enough, thanks to the so-called pinhole mechanism. [111].

Apart from the conventional epitaxial growth mode reached by the MBE or MOVPE
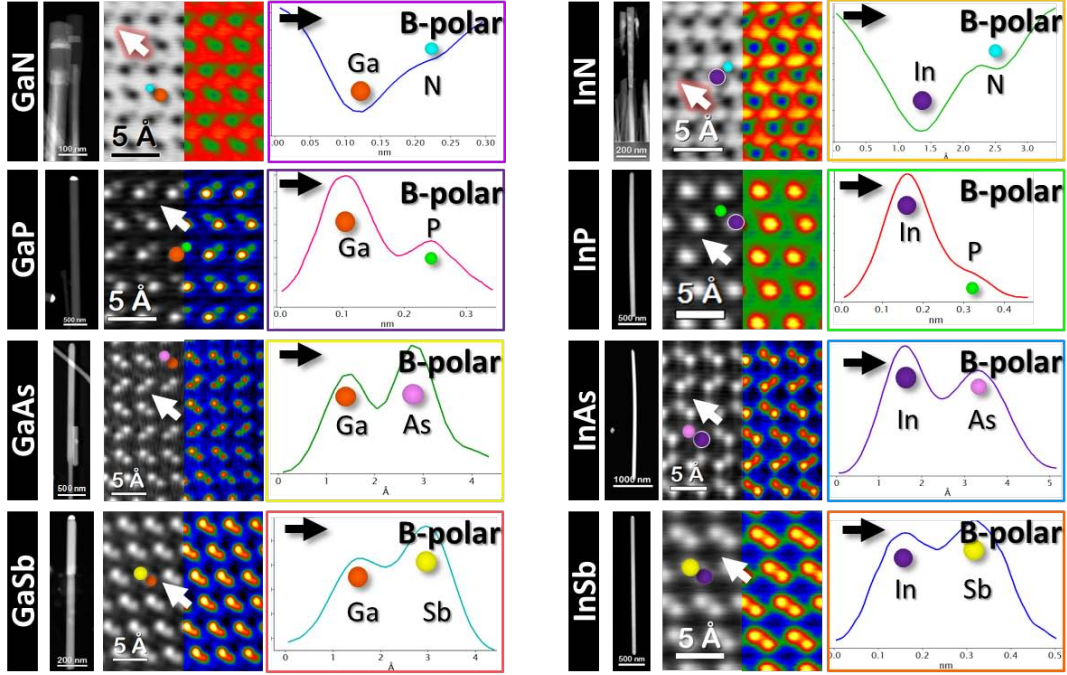
Figure 3.2: GaX and InX (X = N, P, As, Sb) NWs along with atomic resolution HAADF(/ABF for the nitrides) images of their structures. Right side of the atomic resolution images is false colored to enhance the differences among dumbbell constituents. The right side of each panel includes intensity profiles along the dumbbells, following the arrow direction shown in the images.

procedures, the vapor transport growth method here employed proceeds via van der Waals epitaxy, meaning that only van der Waals bonds are established between the substrate and the growing material [125, 126]. In order to avoid the formation of actual bonds across the interface, inert substrates lacking dangling bonds are required (for instance, muscovite mica), regardless their mismatch with the material. In fact, this strategy has been classified as an incommensurate epitaxial growth mode since the alignment with the substrate is reached mediated by van der Waals forces but not actual bonding, overcoming the mismatch limitation [127] and related problems. Remarkably important to us is the fact that by using non-polar substrates (e.g., silicon or mica) we cannot induce any preferential polarity to the growing material as it occurs, for instance, in homoepitaxial growth conditions.

Among all possible III-V combinations, we have characterized GaX and InX NWs, where X = N, P, As or Sb. AlX compounds (X=N or As), have not been considered since such materials are not commonly used to synthesize individual NWs, being mainly used as barriers in other NW heterostructures. This former reason is why we do not study NWs with AlAs or AlN main composition. Nevertheless, it is important to comment at this point that all the AlX barriers studied in III-V NW heterostructures have

been always found to follow the B polarity, in accordance to the main NW core polarity
(GaAs or GaN). Low magnification pictures for the different wires, atomic resolution
images of their structure and intensity profiles along dumbbells in each binary com-
bination are included in Fig. 3.2. It is easily seen that all the III-V NWs analyzed
grow along a B-polar direction, irrespectively of their crystalline phase. Note that both,
GaX and InX tend to present cubic structure when moving down along the group V
row in the periodic table. So, GaN and InN show pure WZ structure along the entire
length of the NWs while the antimonide counterparts are purely ZB. Phosphide NWs
mainly show WZ structure. However, when approaching the tip of the wires (see Fig.
3.3), where the growth conditions are presumably different, cubic insertions show up.
Similarly, GaAs and InAs NWs are mainly WZ although some twinned areas could be
found near the NW tip. Some intrinsic properties of the elements composing the binary
compounds studied, such as the ionicity or atomic radii, may influence the final crys-
tallization and polarity of the NWs. In addition, some other extrinsic parameters can
also favour one certain polarity over the other. In this way, the NW diameter or the
particle supersaturation in vapor-liquid-solid (VLS) synthesis strongly affect the final
phase obtained: the thinner the wire and the higher the supersaturation, the larger the
WZ fraction contained by the resulting structures [128,129]. It is worth mentioning that
a total control on the obtained phase is possible [95, 130, 131], although is out of the
scope of the present study since we are focused on addressing the polarity, irrespectively
of the final polytypic structure presented.

All the NWs here studied belonging to any III-V combination grow along either
$[000\bar{1}]$ in hexagonal systems or any $\langle 111 \rangle$B if the material has cubic structure. Such
result is not surprising for most of the compounds analyzed and, in fact, there is a
general belief supporting that the preferential NW growth direction follows an anionic
polarity [132]. Most III-V compounds, as GaAs, have been observed to grow only along
B-polar directions. Even though, many attempts of reversing the polar growth by using
A-polar substrates, just suppress the NW growth, while other substrate orientations
lead to the formation of tilted NWs, following one $\langle 111 \rangle$B directions [111]. However,
InP and GaN do not seem to follow the rule. GaN is among the most controversial
material in this sense and, indeed, there are researchers supporting Ga-polar directed
growth of GaN elongated nanostructures [133–135], while some works claim the irre-
vocably N-polar nature of spontaneously formed NWs [136]. Interestingly, even mixed
polarities have been reported within the same batch of grown GaN NWs [137], although
with the majority (90 %) of the NWs growing along the $[000\bar{1}]$ N-polar direction.

Moving to II-VI combinations, we have determined the polarity in several Zn and
Cd chalcogenides presenting ZB-WZ polytypism, while compounds with other non-polar
phases are excluded from the study (as it is the case of CdO which shows rock-salt struc-
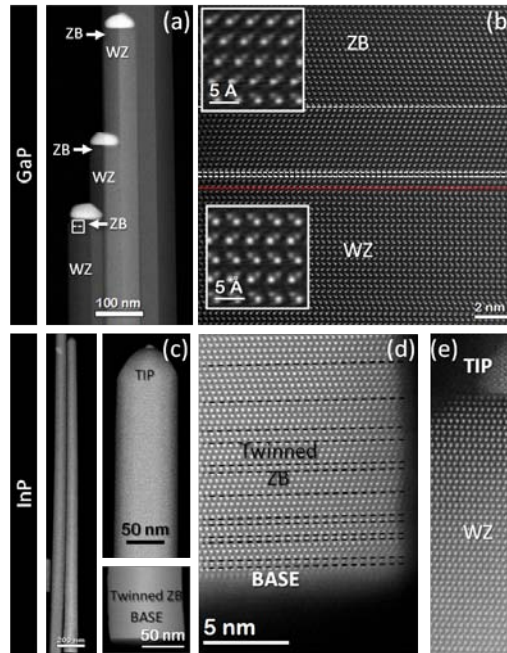
Figure 3.3: (a) Low magnification HAADF image several GaP NWs. (b) Atomic resolution HAADF image of the GaP structure near the tip where the phase changes. (c) Low magnification image of a whole InP NW (left side) and magnified details of its tip and base (right hand). (d) Atomic resolution image of the twinned base and (e) of the pristine WZ tip.

ture). The analyzed II-VI NWs comprise ZnO, ZnTe, CdS, CdSe and CdTe. ZnO, CdS and CdSe were found to be purely WZ; CdTe NWs show polytypism from the base until the tip, with short axial insertions of variable thickness of WZ and ZB, while ZnTe NWs have twinned ZB structure (ZB with highly spaced twin boundaries).

Analogously to Fig. 3.2 for the III-V NWs, Fig. 3.4 summarizes the polarity found in these chalcogenides. Interestingly, ZnO growth is directed by the cationic [0001] direction while the other analyzed chalcogenides follow the most commonly observed anionic growth.

In order to understand the unidirectional polar growth of binary semiconductor NWs, we consider a variety of intrinsic properties of the compound constituents, such as the relative radii or the compound ionicity. The inconclusive results, included in the following section, point out the influence of extrinsic parameters, as those controlled through the synthesis procedure (e.g., temperature, phases present during growth, etc.), referred afterwards (Section 3.2.2).
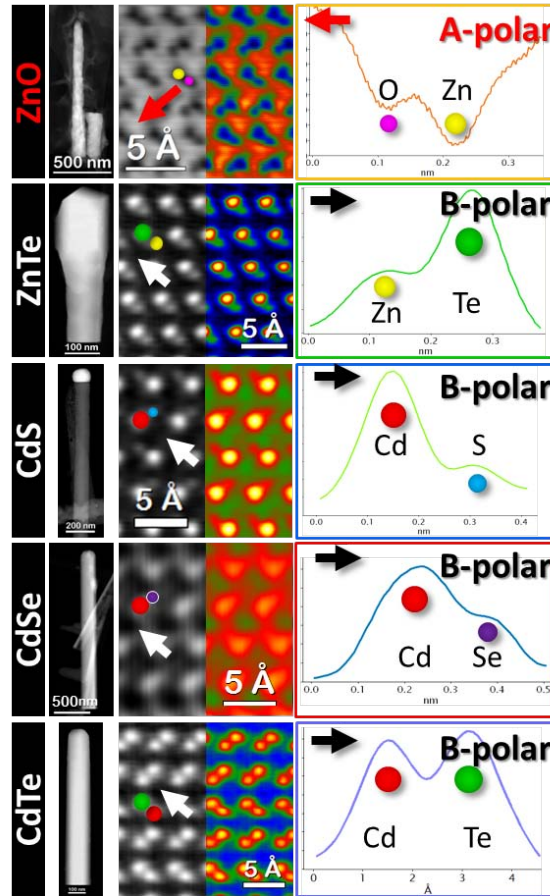
Figure 3.4: Several Zn and Cd chalcogenide NWs along with atomic details of their structures and dumbbell profile integration to address the polarity along the growth direction. The materials concerned are, from top to bottom, ZnO, ZnTe, CdS, CdSe and CdTe. Note that only ZnO grows along cationic direction while the rest does it along B-polar directions.

3.2.1   Intrinsic parameters that may influence the polar growth

Some intrinsic parameters of the constituent atoms of the material are known to affect its crystallinity. For instance, the inonicity is determining in the resulting atomic package, which is a property of the compounds related to the relative electronegativity between the constituents. Also the atomic sizes of the elements conforming the material have an important role on the resulting phase.

The polarity in binary combinations is an extra variable on its crystallinity. We have tried to correlate some atomic parameters of the constituents and geometrical factors of the phases with the experimental observed polarity. Starting by the relative atomic size, no trend is observed explaining the experimental observations. As some compounds are more covalent while others have a stronger ionic character, ionic and covalent radii are also explored. The relative atomic, ionic and covalent size of constituents of the ana-

lyzed compounds are gathered in tables 3.1 and 3.2. The results can be easily compared in Fig. 3.5, where panels (a), (b) and (c) show the ionic, covalent and atomic r_b/r_a relationships in the binary combinations considered. Interestingly, the ratios calculated for ZnO lie always within the lower values range, but the overall trends vary depending on the radii considered. For instance, analyzing the ionic radii ratios, the closer values to the ZnO are found for CdS, CdSe and InN. However, paying attention to the derived covalent relationships, we find out that InN, GaN, AlN and CdS have the closer values to the ZnO. Similarly, for the atomic radii ratios, AlN, GaN and InN show values comparable to that of the ZnO, followed by InP. Regrettably, we could not find a direct connection between the radii relationships and the main polarity observed in non-planar semiconductor nanostructures. Nevertheless, the trend followed by the covalent ratios might be in agreement with the compound tendency to follow both polar options; since those compounds with the lowest relationships, are usually reported in the literature to show ambipolar behavior (e.g., GaN, InN and InP).

Material	ZnO	ZnS	ZnSe	ZnTe	CdS	CdSe	CdTe
Polarity	Zn (**A**)	S (B)	Se (B)	Te (B)	S (B)	Se (B)	Te (B)
r_{b-}/r_{a+}	1.78	2.49	2.58	2.85	1.90	1.97	2.18
$r_{Cov.,b}/r_{Cov.,a}$	0.58	0.82	0.93	1.09	0.69	0.78	0.92
$r_{at.,b}/r_{at.,a}$	0.42	0.71	0.80	0.93	0.64	0.71	0.83

Table 3.1: b/a ratios calculated with the ionic (top row), covalent (middle row) and atomic radii (bottom row) of the compound constituents analyzed, belonging to II-VI binary combinations.

Material	AlN	AlAs	GaN	GaP	GaAs	GaSb	InN	InP	InAs	InSb
Polarity	N(B)	As(B)	N(B)	P(B)	As(B)	Sb(B)	N(B)	P(B)	As(B)	Sb(B)
r_{b-}/r_{a+}	3.35	4.35	2.76	3.42	3.58	3.95	2.11	2.62	2.74	3.02
$r_{Cov,b}/r_{Cov,a}$	0.64	1.02	0.60	0.84	0.95	1.11	0.52	0.74	0.83	0.97
$r_{at.,b}/r_{at.,a}$	0.41	0.73	0.41	0.68	0.73	0.85	0.38	0.62	0.67	0.77

Table 3.2: b/a ratios calculated with the ionic (top row), covalent (middle row) and atomic radii (bottom row) of the compound constituents analyzed, belonging to III-V binary combinations.

Another relevant parameter to consider regards the dangling bonds of the material constituents, considered by some authors [138]. Imposed by the tetrahedral coordination of the constituents within the WZ and ZB crystallographic phases, A and B species at the polar {111} growing planes will have one dangling bond each. In the case of III-V compounds, III-group species (A) have such dangling bonds empty and V-group elements (B) have them occupied by unshared electrons. On one hand, the presence of
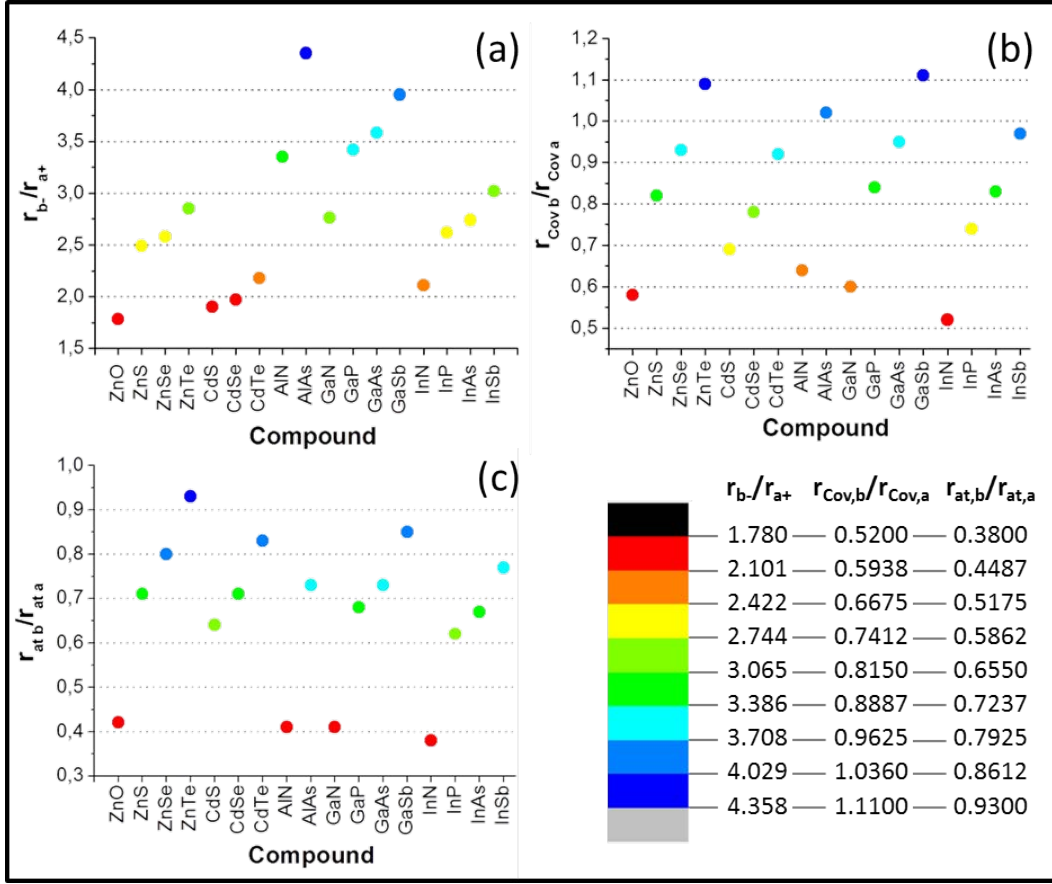
Figure 3.5: r_b/r_a relationships calculated for different binary semiconductors (II-VI and III-V compounds) considering the ionic (a), covalent (b) and atomic radii (a) of the constituents.

unshared electrons preserves the tetrahedral environment (tetrahedral bond geometry) around the B species. On the other hand, the existence of empty dangling bonds around A constituents results in a coordination configuration in between planar and tetrahedral. Based on these arguments, A-polar surfaces should be less favored due to the surface distortion involved and, thus, B-polar directions would be preferred. In the case of II-VI materials, these arguments would be invalidated due to their stronger ionic character, as explained elsewhere [139]. Although useful for the authors to correlate the etching behavior of oppositely polarized surfaces, the prevalence of the ionic character over the atomic configuration imposed by the dangling bonds does not rule the unidirectional polar growth of II-VI compounds, accordingly to our observations.

Related to the previous point analyzed, we try to extract some meaningful information by focusing on the ionic character of the considered compounds, that might affect the polarity. It is usually assumed that compounds showing a electronegativity difference ($\Delta\chi = \chi_b - \chi_a$) larger than 1.8 are ionic, while those with differences below 1.2 are covalent. Those compounds with electronegativity differences in between are consid-

ered covalent with a certain ionic character. The degree of ionicity, f_i can be calculated following diverse models. Accordingly to Pauling's definition, the electronegativity of an atom, χ, is its power to attract the electrons to itself when it is forming a chemical bond. Thus, this property is clearly linked to the ionic character of the compound and, in fact, Pauling's expression for the ionicity only relies on this quantity as follows,

$$f_i = 1 - e^{\frac{-(\chi_A - \chi_B)^2}{4}} \tag{3.2}$$

which is usually expressed as a percentage. This simple definition is based on a thermochemical approach, since the charge distributions are extracted from the heats of formation of the chemical bonds. The differences in electronegativities between atomic constituents, $\Delta\chi$, as well as Pauling's ionicities (expressed in %) for the binary compounds studied, are included in Fig. 3.6. Unfortunately, the $\Delta\chi$ or related ionicity does not explain the observed polarity on the NWs. Some of the cases reported to grow under A polarity belong to the combinations with the highest ionicities, as ZnO or GaN, with 55 and 31 % of ionic character on their bonding according to the calculations. However, the InP case, also reported to easily follow cationic directions while growing [107], cannot be explained under this consideration, since its covalent bonds hardly reach a 4 % of ionicity, invalidating any correlation of a favored polarity dependent on the ionic character of the compound.

A+ \ χ	B-	O	N	S	Se	P	As	Te	Sb
	χ	3.44	3.04	2.58	2.55	2.19	2.18	2.10	2.05
Al	1.61	-----------	1.43 40% ionic	-----------	-----------	----------	----------	----------	----------
Zn	1.65	1.79 55% ionic.	-----------	0.93 20% ionic	0.9 18% ionic	----------	----------	0.45 5% ionic	----------
Cd	1.69	1.75 53% ionic	-----------	0.89 18% ionic	0.86 17% ionic	----------	----------	0.41 4% ionic	----------
In	1.78	-----------	1.26 33% ionic	-----------	-----------	0.41 4% ionic	0.40 4% ionic	----------	0.27 2% ionic
Ga	1.81	-----------	1.23 31% ionic	-----------	-----------	0.39 4% ionic	0.37 3% ionic	----------	0.24 1% ionic

Figure 3.6: The electronegativity for each constituent, χ, is included, along with the difference in electronegativity for every considered compound. The theoretical ionicity, calculated following, Pauling's expression (ec. 3.2) is given in % for the different binary combinations.

A more complex approximation for the estimation of the ionicity was developed by Phillips, who used a spectroscopic procedure to define the ionicity, accordingly to the

dielectric constants of the considered materials. Under such considerations, the ionic character of the compounds is significantly different from Pauling's one, as shown in Tables 3.3 and 3.4, where both, Pauling's (calculated from the expression 3.2 and using the χ values included in Table 3.6) and Phillips' (taken from ref. [140]) f_i are included. One more time, f_i seems not to be correlated with the anionic/cationic preferred growth experimentally observed. For instance, it can be seen that among the more ionic compounds in the table, some show a high tendency to grow following anionic directions, as CdSe or ZnTe, while ZnO, also belonging to this group of highly ionic compounds, follows the cationic one. Therefore, unfortunately, we could not find a satisfactory connection among the compound ionicity and the unidirectional polar growth of the materials at the nanoscale. However, as the most ionic compounds following Pauling's definition, are those with higher tendency to grow under A-polar directions (with the only exception of InP), we cannot completely discard the influence of the electronegativity difference of the compound constituents.

Material	ZnO	ZnS	ZnSe	ZnTe	CdS	CdSe	CdTe
Pauling's ionicity	55	20	18	5	18	17	4
Phillips' ionicity	62	62	68	55	69	70	68

Table 3.3: Pauling's and Phillips' (ref. [140]) ionicities for some II-VI compounds, expressed in %.

Material	AlN	GaN	GaP	GaAs	GaSb	InN	InP	InAs	InSb
Pauling's ionicity	40	31	4	3	1	33	4	4	2
Phillips' ionicity	45	50	37	31	26	58	42	36	32

Table 3.4: Pauling's and Phillips' (ref. [140]) ionicities for some II-VI compounds, expressed in %.

So far, we have not been able to establish a clear and unequivocal correlation among the studied intrinsic compound properties, as the crystalline phase (WZ or ZB), the relative constituent size or the ionic character of the material with the polarity shown along the growth direction. To continue our research, along the next section (Section 3.2.2), we evaluate the possible influence of extrinsic parameters tunable experimentally, that might select the polarity of binary NWs based on our own experience, and completed with an extensive bibliography revision on the topic.

3.2.2   Extrinsic parameters and its influence on the polar growth

To better focus on the different growth parameters that may affect the polarity, we separately analyzed the III-V and II-VI compounds, since they follow different growth

procedures. Although all of them are synthesized by means of bottom-up approaches, the III-V NWs are obtained either by MBE or by MOVPE, whereas II-VI wires are produced by a vapor transport procedure in a furnace; and, therefore, they are studied apart in the following.

III-V Nanowires

Importantly, the MBE and MOVPE growth procedures employed to create the NWs rely on the vapor-liquid-solid (VLS) mechanism, firstly reported by Wagner and Ellis to produce Si nanowhiskers, where a liquid gold droplet collects the supplied vapor silicon until supersaturation (exceeding eutectic composition) and resulting on the silicon precipitation [141]. Dealing with compound materials, the growth is more complex since at least two precursors are needed, one for each constituent present on the final product, involving much more complex phase diagrams. Interestingly, in the case of III-V combinations, only the III-group species are found at the droplet when analyzing the post-grown samples, but not V-group species. In fact, no Au-III-V ternary or Au-V binary phases stable below 600ºC have been reported, indicating that only III-group component dissolves significantly in the particle. Moreover, the particle-assisted growth of NWs do not necessarily involves liquid alloys and, depending on the growth conditions and phases related the metal particle may stay solid. Then, the NW growth will proceed by diffusion of III and V species on the solid droplet, being the mechanism known as vapor-solid-solid (VSS). Even if the droplet is liquid during growth, it should be noted that the absence of an eutectic point at the working range invalidates Wagner and Ellis's mechanism, although many reported works on NWs growth wrongly assume it. From here on, we will use the term VLS to refer to the particle-assisted growth, but not the Wagner and Ellis' mechanisms involving eutectic phases.

Unfortunately, there is not a fully-developed model cohesively explaining all types of particle-assisted NW growths, and the role of the droplet during growth is not completely understood. Nevertheless, it is clear that the deposited droplets behave as nucleation seeds, where the particle-wire interface acts as sink for the nucleation. By selecting the growth parameters accurately, it is possible to kinetically hinder further deposition or nucleation of species on the substrate or on the NW side facets, promoting the unidirectional growth along the NW axis. Notice that it is also possible to promote the growth on the lateral facets by simply adjusting the growth conditions (e.g.: changing the III-V ratio and/or the temperature) [43, 44]. Once the nucleation occurs, it is widely accepted that III species are adsorbed at the substrate surface and NW sidewalls and diffuse through the NW growth front. On the other hand, V-group species are directly incorporated at the particle-NW interface or at the droplet surface where they diffuse
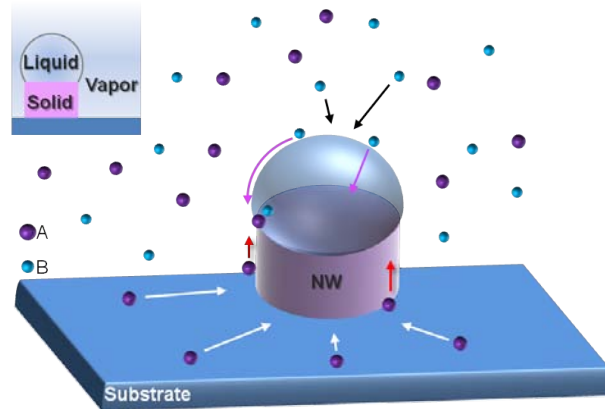
Figure 3.7: While A atoms/precursors (III-group) are absorbed at the substrate surface and/or NW facets to diffuse through the NW-droplet interface, B species (V-group) directly impinge the droplet and diffuse to the interface with the NW.

through the triple phase line to precipitate along with the III-group constituent. Thus, the material formation takes place at the triple phase line, giving rise to the VLS name of the mechanism, and the morphology of the resulting NW will be strongly influenced by the morphology of the liquid-solid interface. In the case of MOVPE growth, the precursor decomposition greatly influences the overall kinetics, limiting the growth at the low temperature regime, unless the droplet catalyzes the decomposition. Similarly, surface diffusion may affect the growth ratio under MBE conditions. A schematic picture of the processes involved in the most general case of particle-assisted NW growth is shown in Fig. 3.7. The VLS mechanism has been widely exploited for growing NWs and it turns out that NWs grown under VLS conditions (particle-assisted growth) tend to exhibit B-polarity, in agreement with our observations, including InP NWs.

InP Nanowires

Apart from our observation of P-polar InP NWs; both, In- and P- polarities are reported in the literature (see table 3.5), but a comprehensive explanation of such bidirectional behavior is missing. Interestingly, the reported P-polar InP NWs grow by using metal seeds [9, 144, 145], so particle-assisted, as it happens in our case. But, whenever the use of a seed droplet is avoided, the preferred growth direction of InP is along a $\langle 111 \rangle$A direction [107, 142, 143], indicating that the resulting NW polarity is governed by the underlying growth dynamics. It must be pointed out that, unfortunately, most of the reported works on InP NWs do not pay attention to the present polarity and in some cited examples we have inferred the NW polarity by assuming that of the substrate, which is energetically favored over a polar inversion. In-polar catalyst-free InP NWs can be grown by selective area growth (SAG) procedures, where the substrate surface is coated with a patterned material, acting as mask. Such a mask will prevent

Material	Polarity	References
InP	A (In)	[107], [142], [143] → SAG
	B (P)	[9], [144], [145] → Particle-assisted
GaN	A (Ga)	[108], [146] → SAG
	B (N)	[136], [147], [148] → Particle-assisted
InN	A (In)	[149] → Spontaneous growth
	B (N)	[150], [151], [149] → Spontaneous growth
ZnO	A (Zn)	[120], [152], [153], [154], [155], [156], [157] → Spontaneous growth [158] → SAG [159] → Particle-assisted
	B (O)	[153] → Spontaneous growth [158] → SAG [152] → Particle-assisted

Table 3.5: Reported polar directions for InP, GaN, InN and ZnO materials, indicating the type of the growth mechanism (spontaneous, selective area (SAG) or particle-assisted growths are distinguished).

the NW nucleation on its top and the material will be deposited only at the patterned un-masked regions. Under MOVPE growth conditions, the precursors diffuse on the mask, SiO_2 for instance, until reaching the patterned holes where the bare substrate is exposed and the precursors are deposited to create the In-polar NW [107]. Selectivity can be controlled by tunning the growth parameters to adequate the precursors diffusion lengths. VLS growth can be performed in a selective way, too; as reported elsewhere [144], showing VLS mechanism under both, selective and non-selective area growth conditions. Dalacu *et al.* reported that both condition sets lead to the formation of B-polar wires, in agreement with the other VLS grown NWs.

In the InP NWs analyzed in the present manuscript (P-polar, see Fig. 3.8(c-g)), the growth is initiated by Au seeds. Consequently, the post-grown wires show the derived droplets attached to the tip, as observed in Fig. 3.8(a,b).

GaN Nanowires

Moving back to the GaN case, it is noteworthy that, the GaN NWs here studied are self-assembled on Si substrates. GaN NWs are catalyst-free grown by PAMBE meaning that N is supplied by a rf-plasma source. The substrate temperature was kept at 775°C, and the growth proceeds under N-rich conditions. As the procedure is catalyst-free, there is no droplet involved, no liquid phase mediates the NW growth and thus, the VLS mechanism is not valid, differing the GaN growth dynamics from the other
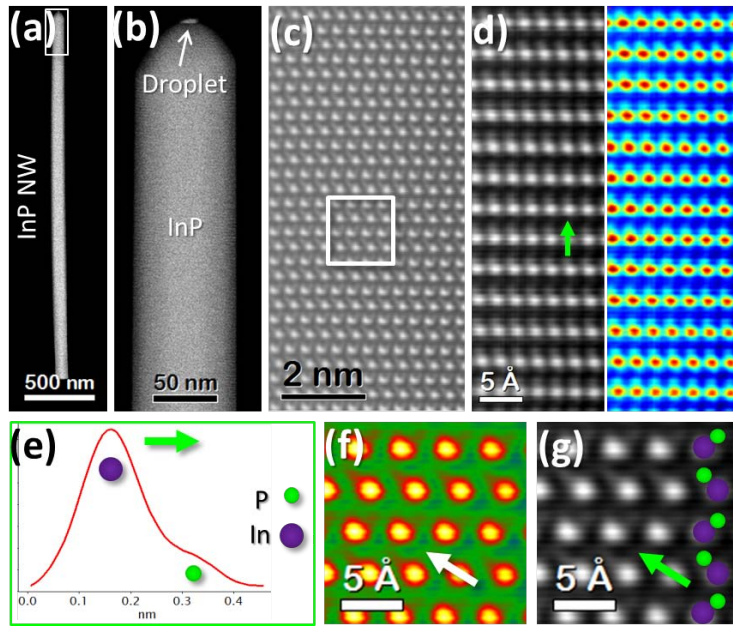
Figure 3.8: Polarity analysis performed on the InP NW shown in (a). The tip shows a small droplet on the tip as consequence of the Au seeds used (b). A closer look to the structure along two perpendicular directions, [11$\bar{2}$0] in (c) and [1$\bar{1}$00] in (d) (also displayed in false color on the right side to enhance the P positions), reveal the dumbbells orientation. The P-polarity is evident from the dumbbell intensity profile in (e) taken along the position pointed in (f) and (g).

compounds presented. Investigations on the PAMBE growth of GaN NWs show that self-assembled NWs formed within this regime are irrevocably N-polar, irrespectively of the substrate polarity [136]: while B-polar substrates leads to the formation of dense N-polar NW arrays, using A-polar substrates sparse N-polar NWs are created on top of Ga-polar pedestals. Note that in the latter case, the GaN nucleation seed must develop an inversion domain boundary between the pedestal and the NW, in order to flip the polar growth from Ga- to N-directed. Moreover, it has been shown that the substrate nature has not noticeable implications on the NWs growth as long as its mismatch ensures a Volmer-Weber nucleation; while its orientation defines the growth direction (inclination) [160], but keeping the B (anionic) polarity.

For instance, changing the substrate to C-diamond (un-polar) and increasing the temperature (930ºC), N-polar GaN NWs are also created, growing in direct contact with the diamond (without any intermediate layer) [148]. However, switching to SAG conditions, by creating a Ti mask on the diamond substrate and using a 890ºC growth temperature, the resulting NWs grown by PAMBE are Ga-polar [108], as shown in Fig. 3.9 (see also table 3.5). Morphological differences in NWs with opposite polar directions cannot be neglected: Ga-polar NWs expose inclined top facets belonging to the {1$\bar{1}$0l} family and have much lower aspect ratio than those NWs growing along

N-polar directions, which in addition have $(000\bar{1})$ horizontal top facets (see Fig. 3.9). This observation is in agreement with previously reported works on Ga-polar and N-polar NWs. Indeed, Ga-polar NWs are usually named nanocolumns, highlighting their shorter and wider shape compared to N-polar NWs. Such morphological differences may be indicative of the different dynamics/kinetics underlying the self-assembled and SAG procedures.
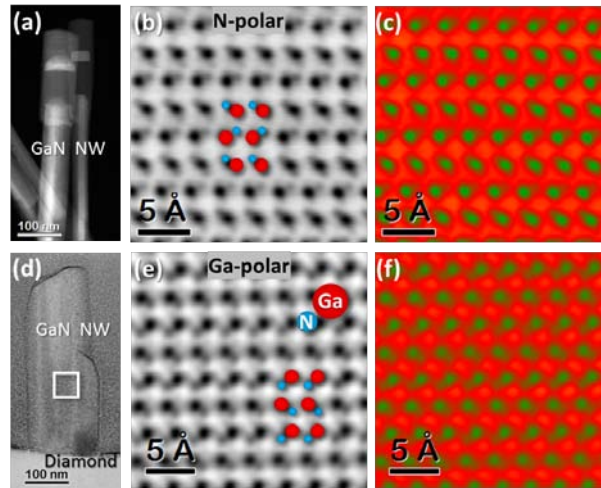

Figure 3.9: (a-c) GaN NWs grown on Si substrate by PAMBE: (a) Low magnification HAADF image of the analyzed GaN NWs (b, c) Atomic-resolution ABF image of the GaN structure (colored in (c)) evidencing the N-polar directed growth. (d-f) GaN NW grown by SAG PAMBE on diamond/Ti (substrate/mask): (d) Low magnification of an entire NW. (e, f) Atomic-resolution ABF images probing the Ga-polarity of the NW.

Both growth modes are reported to be N-limited despite the N-rich conditions [108, 161], since N radicals are only incorporated where they directly impinge; while Ga atoms diffuse on the substrate (or mask, if it is used) and NW sidewalls. SAG successes by exploiting the differences in sticking coefficients between the mask and the substrate. Thus, the growth is governed by the sticking coefficients and diffusion lengths of Ga atoms, which can be tunned by modifying either the substrate temperature or the N-flux supplied. However, the process is neither completely understood yet. Some authors claim that these two parameters have opposed effects on the selectivity since increasing the substrate temperature enhances the Ga diffusion length and desorption on the mask (thus, better selectivity is achieved), while higher N-fluxes raise the probability of the GaN formation on the mask, before the Ga reaches the patterned hole (lost of selectivity) [146, 162]. So, the growth can proceed at different temperatures by properly adjusting the III/V fluxes. Nevertheless, recent works report that the selectivity improves for higher N fluxes [108]. Anyhow, it is clear that the III/V ratio strongly influences the selectivity and the further growth of nanostructures.

SAG experiments varying the patterned nanohole diameter on the mask, result in really different morphologies [146]: large nanoholes (200 nm) result on the formation of GaN pyramids, faceted by $(1\bar{1}02)$ (r-planes), which do not further evolve to NWs; while small nanoholes (50 nm) lead to the formation of NWs with flat top facets (c-plane). Middle size patterns (150 nm) allow the growth of NWs but showing semipolar top facets. Bengoechea-Encabo *et al.* explain such variations attending to the local III-V ratio in the nanohole vicinity: the bigger the hole, the lower Ga adatom density (lower III/V local ratio) and, vice versa, the smaller the hole the higher Ga atom density (higher III/V). Thus, the different local III/V ratio may modify the growth kinetics. Although not reported in this work, we can postulate the Ga-polarity of the pyramids and pointed NWs grown on larger nanoholes from the observed shape, and N-polarity for the GaN NWs created on smaller holes, showing flat top surfaces. As the different shapes are created under different local growth regimes, the growth kinetics may change to allow the development of the various morphologies, which we believe might show opposed polarities, too. A simple but plausible explanation may be that lower III/V ratios would involve more N atoms present in the reactor than Ga ones, increasing the probability of a N atom to firstly impinge the bare substrate surface, resulting in Ga-polar nanostructures. Oppositely, under higher III/V ratios there should be more Ga atoms on the environment, inducing the Ga attachment to the substrate before any N atom could arrive and leading to the formation of N-polar NWs.

InN Nanowires

Many similarities can be found comparing GaN and InN NWs growth, although reports on its actual unidirectional polar growth are scarce (see table 3.5). InN NWs are also mainly synthesized catalyst-free by PAMBE under N-rich conditions but at lower temperatures to prevent InN decomposition. As it occurs in the GaN case, InN NWs grown on N-polar GaN templates are N-polar with flat top facets while using Ga-polar GaN substrates results in In-polar NWs with pyramidal tips [149]. Also as it happens with GaN NWs, the N-polar InN NWs show larger aspect ratio than those In-polar. Therefore, the parallelism between these III-nitrides is obvious, suggesting that they share the growth mechanism as expected from the similar growth procedures employed. Both nitride NWs follow a catalyst-free synthesis route, which *a priori* is expected to exclude the VLS mechanism. Following this trend, GaN NW growth has been depicted attending to the higher sticking coefficients of group-III species on the NW tip relative to the sidewalls [147]. However, in the case of InN NWs, it has been suggested that the growth can be initiated by the self-catalytic effect of In accumulations during the earlier stages of growth [150, 151], similarly to the self-catalytic effect reported for GaAs NWs grown by MBE [58, 111]. In the two cases the growth is mediated by an amorphous layer (SiO_2 and Si_xN_y coatings for the growth of GaAs and InN NWs, respectively)

and the nucleation events, i.e., the metal droplet location on the surface, tend to take place around existing defects. In contrast to the GaAs NWs, where the Ga droplet can be found attached to the NW tip at the end of the growth process, the In particle may be nitridated during/after growth, reason why it is not seen on the tip of post-grown NWs.
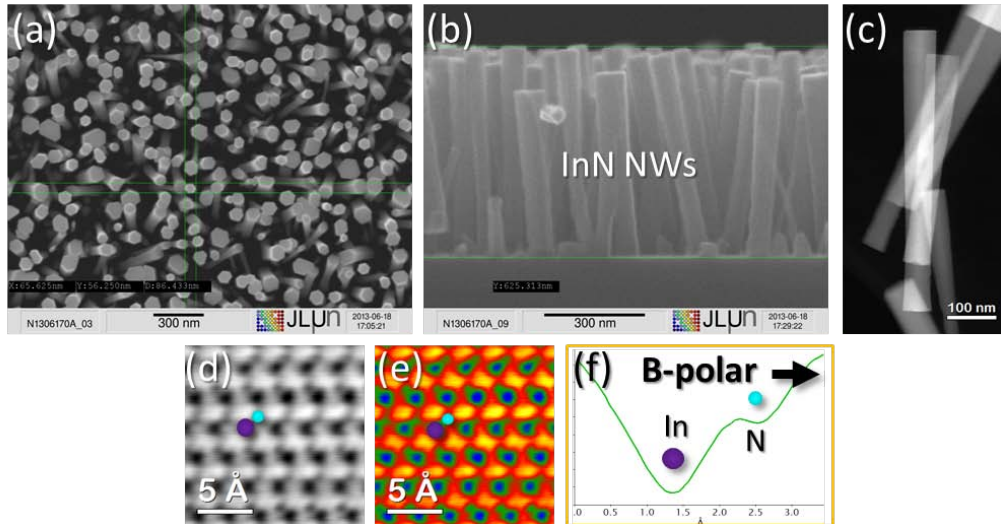

Figure 3.10: SEM images taken at bird view (a) and longitudinal section (b) of the as grown InN NWs analyzed. (c) HAADF image of several InN NWs overlapping. The atomic resolution ABF image, included in (d) in grey scale and in (e) in false colored, evidences the N-polarity of the wires, also clear in the intensity profile included in (f).

Then, based on our results (see Fig. 3.10) and previously reported data, it appears reasonable thinking that the observed polarity in elongated nanostrucutures is a consequence of the growth procedure. Unfortunately, a complete comprehension of the dynamics and kinetics has not been achieved yet. Nevertheless, the growth procedures can be divided in two separated groups, depending on whether the growth is particle-assisted or not. In agreement with the literature and as far as we know, we observe that most of the NWs growing metal droplet mediated, either by a foreign metal or by a material constituent, result on B-polar NWs for the working regimes reported. In absence of droplet, the underlying growth mechanism for the NW formation may be related to the constituents sticking coefficients on the different surfaces available during growth, which is actually quite extended mechanism for the selective area growth. Similar arguments can be used to explain the unidirectional growth of NWs when lacking both, a patterned mask covering the substrate and any metal droplet, but attending to the different sticking coefficients of the precursors on the sidewalls and top facet of the forming NW. Importantly, the local experimental conditions (temperature, III/V ratio, etc.) on the nucleation sites can differ from the overall input conditions, hardening the

understanding of the growth. The issue can be tentatively simplified in terms of the effective limiting and excess reactants, since it might be reasonable that the exceeding specie could reach the growth site before the limiting one, and thus pushing the growth under the limiting reactant polar direction. But the role of other parameters, such as surface energies, phases involved (liquids, solids and/or gases), etc. should not be underestimated at first.

Implications of the droplet composition

Until know, we have mainly commented on the seeded growth of NWs by using either gold or self-catalytic procedures. However, it is important to note that the energy balance, as well as the growth kinetics, may change depending on the droplet composition. Many different metals can be intended for guiding the NW growth, such as Ni, Pd, Pt, Mn, Cu, Ag, Bi or Fe [163]. In fact, the alloy composition of the nucleation droplet offers a playground to engineer the crystallographic growth direction. That is the case, for instance, of GaN NWs grown by metalorganic chemical vapor deposition (MOCVD) using different Au-Ni alloys. The growing GaN NWs follow two different non-polar directions depending on the droplet composition [164]. Ni-rich Au-Ni droplets lead to the formation of [11$\bar{2}$0] NWs, while lowering the Ni concentration the growing wires follow the [1$\bar{1}$00] crystallographic direction.

Also playing with the metallic alloy composition, by mixing In and Au, Wang *et al.* reported the feasibility of switching the growth direction of InP NWs [165]. While In-rich droplets drive the growth along the [100] direction, after the In depletion, the wires redirect their growth along one of the possible [111]B directions.

Interestingly, the nature of the droplet not only induce alternative crystallographic growth directions, but also changes the geometry of the growing structure. Most semiconductor NWs show either hexagonal or circular cross-section, as it is the case of the structures analyzed along the present chapter. This behavior is usually attributed to the energy minimization offered by the developing facets. Nevertheless, triangular cross-section NWs have also been reported when substituting the common Au-seeds by different metals. For instance, GaAs NWs, which are widely known to grow as perfect hexagonal prims, develop triangular cross-sections if replacing the Au or Ga droplet by Sn [166]. Similarly, self-assembled GaN NWs exhibit hexagonal sections but whenever the growth is particle-assisted, the cross-section shape is dependent on the droplet composition and substrate employed. For instance, seeding the GaN NW growth with Au on (111) MgO and (100) $LiAlO_2$, lead to the formation of hexagonal and triangular cross-section wires, respectively [167].

Moreover, the wetting configuration or contact angle of the droplet, tunable, for instance, with the composition or growth temperature, has also a strong impact in the resulting structure. In this context, the faceting of the wires can be explained attending to the droplet configuration [168] and its oscillations during the growth process [9]. And, not only the overall morphology of the growing system, but also the atomic structure of the material (crystalline phase) has been reported to be controllable by tuning the droplet contact angle [95, 169]. Going further, even the growth yield can be optimized by playing around with the wetting configuration of the droplet [170]. It should be pointed that the observed contact angle is a consequence of many parameters, such as the substrate employed, including its phase and orientation, or the already mentioned droplet composition and the growth temperature, whose effects must be carefully evaluated [171].

II-VI Nanowires

ZnO Nanowires

As it happens with the GaN and InP cases among III-V NWs, ZnO NWs within II-VI combinations have been reported to show both, Zn- and O-polarities [152, 153, 172]. Although a huge bibliography exists regarding the ZnO NWs growth, reports showing the actual polarity of those NWs are more scarce. Oppositely to GaN, most of the related bibliography on the polarity of ZnO NWs invokes the cationic faster growth direction for the material [120, 154–156, 159] (see talbe 3.5). In fact, the growth of ZnO NWs is highly favored on A-polar substrates, as can be inferred from reported studies using periodically polarity-inverted substrates [173–175], where the ZnO NW growth only succeeds on the Zn-polar substrate regions. These three cases report Zn-polar NWs by chemical vapor transport and condensation from ZnO powder, using Au particles as nucleation seeds [173] or by a catalyst-free procedure [174, 175]. Changing the synthesis from the chemical vapor transport to metal-organic vapor phase epitaxy (MOVPE), the growth of ZnO NWs on non-polar and B-polar substrates has been achieved. Nevertheless, the spontaneously formed (no catalyst used) NWs also follow the Zn-polar direction [157]. Another example of this preferential cationic polar growth occurs when the ZnO grows on top of GaN NWs (B-polar), forming ZnO/GaN heterostructures. Even in this latter case, when growing the ZnO axially on top of the B-polar GaN firstly grown, the ZnO shows A-polarity [41].

So, on one hand, studies focusing on the substrate influence on the polar growth of ZnO NWs, show their cationic nature, even when using sapphire (non-polar) or O-polar ZnO layers as substrates. The resulting NWs appear on top of pyramids which grow from a ZnO buffer layer in both cases (using sapphire substrates such layer is unin-
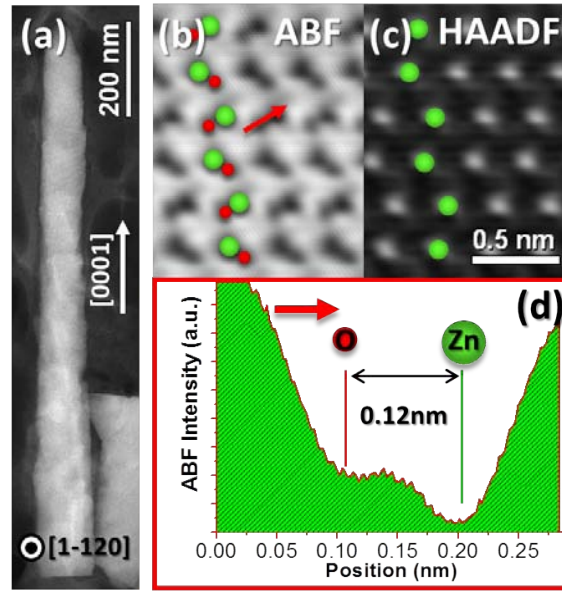
Figure 3.11: Polarity analysis performed in the ZnO NW shown in (a). The atomic resolution images shonwn in (b,c), evidence its WZ structure while the Zn-polarity can be seen only on the ABF image (b), where the intensity profile shown in (d) is acquired, following the direction indicated by the red arrow.

tentionally formed) [157]. Interestingly, the underlying ZnO layers and pyramids are O-polar, while the NWs are Zn-polar, and the polarity inversion takes place through inclined facets at the pyramids-NWs interface rather than basal planes. The inversion can be understood by assuming that both polarities can nucleate; then, O-polar nucleus would laterally expand, while few Zn-polar nucleus would evolve to NWs. The morphology of the inversion domain boundary (IDB) resembles that reported in ZnO doped by trivalent metal ions, M^{3+}. Structurally, the introduction of M^{3+} into the ZnO lattice promotes the formation of ordered MO_6 octahedral units distributed along the $\{1\text{-}21l\}$ planes and (0001) basal plane, creating a zigzag net [176] (see Fig. 3.12). Such distribution of the trivalent metal ions forces the ZnO_4 tetrahedral blocks to be oppositely oriented at both sides of these planes, giving rise to the IDBs since the ZnO polarity is flipped across the boundary [177].

In contrast to what is reported elsewhere [157], Consonni *et al.* [158] have shown that ZnO NWs will follow the substrate polarity if they are selectively grown by chemical bath deposition (CBD), meaning that the Zn- or O- substrate polarity is transferred to the NWs. As the growth proceeds in solution phase, the main interactions to be considered during the growth are quite different from those on vapor phase. The solution growth is mainly governed by the electrostatic interactions of the ions which fill the patterned holes where the underlying ZnO is exposed, but they do not interact with
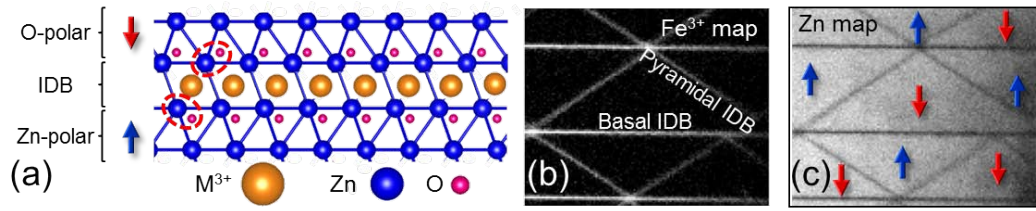
Figure 3.12: (a) Basal IDB in ZnO structure promoted by the incorporation of a trivalent cation, M^{3+}, occupying octahedral positions and forcing the flip of the ZnO_4 tetrahedrons (b,c) Experimental EELS Fe and Zn maps, respectively, evidencing the position of the IDB. Blue arrows point the two different polarities. EELS maps adapted from [177].

the Si_xN_y amorphous mask, driving the selective growth. Similarly, it can be expected that the Zn^{2+} and OH^- arriving precursors will be ordered attending to Coulomb forces and, thus, following the substrate polarity. In agreement with Consonni's work, Guillemin *et al.* [153] have stated that under the specific CBD conditions for the ZnO growth, both polar c-planes are active.

The solution growth procedure carried out on chemically inert substrates, i.e, phlogopite mica, successfully results on vertically aligned ZnO NWs, too [178]. The environmental conditions allow the inhomogeneous wetting of the precursors, resulting in small nucleation events with high anisotropic growth rate along the *c*-axis, which promotes their vertical development. The merging of structures growing close to each other gives rise to the observed ZnO NWs, following a Volmer-Weber mechanism: the initially created ZnO islands on the substrate evolved to coalescence resulting in a unique structure (a NW in this case).

On the other hand, opposite polar directed growth of ZnO NWs have been reported depending on whether the growth is particle-assisted or not, similarly to our observations for III-V combinations, shown in Section 3.2.2. Among other techniques, ZnO can be synthesized by metal-organic chemical vapor deposition (MOCVD) in both fashions, particle-assisted and spontaneous growth modes, by tuning the growth parameters (mainly the O/Zn ratio). The resulting NWs show O-polarity whenever the synthesis is particle-assisted or VLS, and Zn-polarity if they are spontaneously formed [152]. As the Au-Zn phase diagram lacks eutectic point, the arriving Zn atoms or precursors will diffuse into the droplet to the particle-wire interface where the oxidation takes place, since O atoms are believed not to be adsorbed by the gold surface. In presence of a Au droplet, it can be argued that the diffusing Zn atoms from the droplet will be preferentially trapped at the Au-ZnO (O-terminated) surface since it is energetically favored over the Zn-terminated; leading to preferential O-growth. In absence of droplet, when NWs are spontaneously formed along the Zn-polar *c*-direction, several causes have been

proposed to favor the observed polarity as anisotropy of the growth rates, surfactant effect related to Al or Si impurities from the substrate or electric field effects, but non of them provide a universal answer and the question remains opened.

Regarding the other analyzed II-VI compounds, there is not much said about their unidirectional polar growth on the literature. It is generally assumed that the fast growth takes place along B-faced directions [179] but the growth along the opposite direction is also allowed (at least for some compounds), though slower, as we expose in the following.

ZnTe and ZnSe Nanowires

The existence of anisotropic growth rates might explain the formation of NWs presenting both polarities in ZnTe grown by particle-assisted MBE, with the majority of NWs showing Te-polar growth [180]. This anisotropic behavior can be related, for instance, with the formation of stacking faults when growing along the slow A-polar directions, while fault-free structures are created if the growth is B-directed [179]. Accordingly with VLS models proposed for III-V combinations, diffusion contribution to the ZnTe NW formation under MBE conditions should be included to account for the inverse dependence of the length vs diameter (i.e., $L \propto 1/d$). Same observations have been reported for ZnSe NWs grown under similar conditions (Au-assisted growth by MBE) [181]. Neglecting the diffusion-induced mechanism, one would expect inhibition of the NW growth for diameters below a certain threshold due to the drop of the supersaturation for diminishing diameters, as consequence of the Gibbs-Thompson effect and in contrast to experimental observations.

In agreement with most of the compounds, we have found that ZnTe NWs grow following Te-polar $\langle 111 \rangle$ directions. As a proof of fact, Fig. 3.13(b) includes an intensity profile taken across one dumbbell in the HAADF image of the ZnTe structure shown in (a). Contrary to the observations reported in ref. [179], the analyzed B-polar ZnTe NWs show many twin boundaries, especially when growing at high temperatures, as discussed in Section 3.3.1.

ZnS, CdS and CdSe Nanobelts

Polar related-growth has been observed in other 1D morphologies, as elongated nanobelts. The anisotropic growth behavior along opposite $\langle 0001 \rangle$ polar directions has been noticed when growing ZnO [172], ZnS [182], CdS [183] or CdSe [184] nanobelts or nanoribbons by thermal evaporation. In all those studies, the nanobelts grow laterally constricted by $\{000\pm1\}$ planes, which show comb-like or saw-teeth morphologies
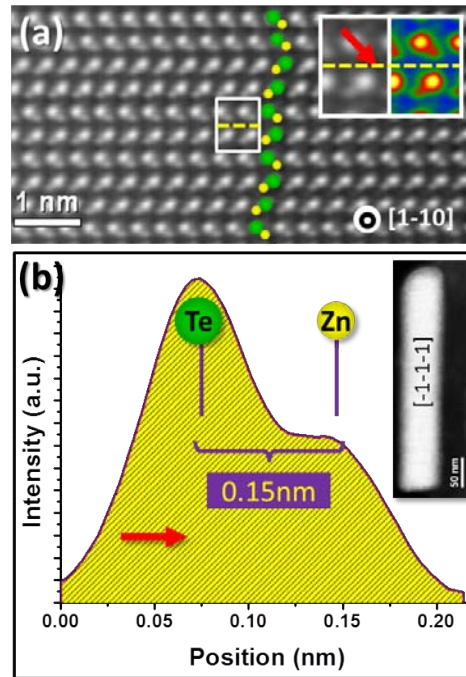
Figure 3.13: (a) Atomic resolution HAADF image of the ZnTe structure of the NW shown as inset in (b). The intensity profile displayed in (b) has been taken along the red arrow in (a), evidencing the Te-polar growth direction of the ZnTe NWs.

asymmetrically developed. The cationic (0001) side tend to show saw/comb-teeth shape while the anionic (000$\bar{1}$) side of the belts is more prone to remain flat. This fact is mainly attributed to the higher reactivity known for the cationic surfaces in contrast with the anionic ones. Based on the observation of Zn enrichment on the growth front, the teeth formation on Zn-(0001) surfaces is believed to follow a self-catalytic process. For the ZnO and CdS cases, formation of nanofingers on the anionic polar side can take place depending on the growth temperature. The nanofingers are shorter and thinner than the saw-teeth and are only formed at the lower temperature regime. Although some of the nanobelts were particle-assisted synthesized, the teeth formation occurs apart from the droplet, thus, through vapor-solid procedure.

Taking into account our experimental observations and previous studies on the topic, it is likely that the polar unidirectional growth at the nanoscale is a consequence of the growth mechanism which is dependent on the synthesis procedure and experimental conditions.

Summing up, we have found that NWs growing at the triple phase line; involving solid, liquid and vapor phases (VLS growth), tend to follow mainly B-polar directions in both, III-V and II-VI compounds. The liquid phase is usually intentionally present

in the medium by using metallic particles which will act as nucleation seeds, but the metallic species supplied during the growth, i.e., III- and II-group species, can result on the formation of liquid droplets with the same effects on the overall procedure (self-catalytic mode). These metallic droplets collect the supplied vapor species which will arrive by diffusion on the substrate and NW sidewalls in the case of metals (III and II species) or by impinging the droplet and diffusing through the interface with the substrate (during the nucleation)/NW (alternatively non metallic species can be directly incorporated at the triple phase line, as in the case of oxygen), for the V and VI elements.

Contrary, it is apparent that those growth mechanisms avoiding the use of metallic droplets, as catalyst-free selective-area growth procedures are more prone to the formation of A-polar NWs. In a very simplistic way we tentatively reduce the problem to the higher probability of one of the constituents (usually A species) to reach the substrate (resulting in B-polar directions pointing the tip), but being aware of the many factors altering such probability. However, a huge control on the experimental conditions and on how they rule the growth is needed, since their modification can switch the growth regime resulting in a different mechanism, and thus, loosing the control over the polarity. Known the feasibility for some materials to grow under both polarities, there might be no reason preventing the cationic growth for the others, if finding the proper growth conditions. It is worth keeping in mind that the requirement to be fulfilled is enhancing one polar growth over the other, making the desirable polar direction being developed faster than the opposite. More work should be done to reach the desirable understanding on the growth, since even for the widely employed VLS procedure a complete comprehension of the process has not been achieved yet.

3.3 Polarity-Driven Growth Mechanisms in Non-Planar Nanostructures

As it has been already mentioned in the chapter introduction (3.1), polymorphism and polarity play the main role on the morphology of the synthesized structures at the nanoscale. For instance, periodically distributed twin boundaries perpendicular to the growth direction in NWs are known to induce the lateral zigzag exhibited by those structures, since the faceting is switched whenever a twin is originated [9,185]. Another example of this fact is the different morphology shown for the same materials growing under opposite polarities, as the previously discussed GaN N-polar NWs or Ga-polar nanocolumns.

A wide variety of morphological structures can be produced nowadays at the nanometer regime, going from the simplest particles, wires and layers to really sophisticated

and complex shapes, as hierarchical trees [186], V-shape nanomembranes [187] or poly-pods [188], to list some of them. But gaining the desirable control making possible the smart design and tailoring the morphology requires a deep understanding on their atomic arrangements, which is only achievable by means of (S)TEM techniques. Accurate analyses of their crystallographic phases, polarity, structural defects, diffusion, etc. pave the basis for depicting the underlying growth mechanisms and allow spreading the control over the synthesized structures.

Along the present section, we inspect various morphologies in order to understand how they are created. Going from differently faceted NWs, to some 2D-like architectures, passing through a variety of branched shapes, we rule the basic aspects of the grown structures in terms of the atomic observations. Our insights are especially focused on the polarity at those systems, and the related implications on the growth mechanisms. The creation of 3D atomic models that mimic the actual shape of the analyzed nanoobject is highly useful for the understanding of their complex morphologies. The presence of structural defects can be incorporated into the models to understand their influence on the analyzed lattices, as well as working to calculate the simulated images.

3.3.1 From Nanowires to Tetrapods: Unveiling the Growth Mechanism

Preferential polar growth and twinning phenomena in binary semiconductors can be exploited to synthesize a wide variety of morphologies with high structural complexity. Along this section, it is shown how the same material, ZnTe, growing under slightly different conditions evolves to different morphologies, which are explained in terms of the observed polymorphism and polarity [189].

The synthesis of ZnTe nanostructures is carried out in a vapor-transport system and using suitable substrates in order to allow a van der Waals epitaxy, such as muscovite mica. Substrates undergoing deionized water exposure for few minutes result in the growth of NWs while untreated mica substrates lead to the formation of branched structures, i.e., tripods and tetrapods, especially at the lower temperature regimes.

Conducting the synthesis at high temperatures results in the formation of cylindrical nanorods, growing perpendicular to the mica surface. Moreover, shape transition in the nanorods is observed according to the central temperature of the furnace. At the higher growth temperature employed, the NWs show the so mentioned cylindrical section but when the growth temperature is lowered down, the resulting NWs have hexagonal faceted cross-section. As the used furnace has a temperature drop from the center to the edges, such temperature dependence was verified by using larger pieces of

mica substrates, extending along different areas of the furnace and thus, growing under different local temperatures. The resulting synthesized NWs are cylindrical at the upstream (central part of the furnace) and hexagonal faceted at the downstream (through the quartz tube ends). In addition, we observe the presence of hybrid NWs, with cylindrical bases and faceted tips when going from the upstream region of the furnace to the downstream, as consequence of the morphological transition with the temperature. The three kind of NWs are shown in Fig. 3.14.
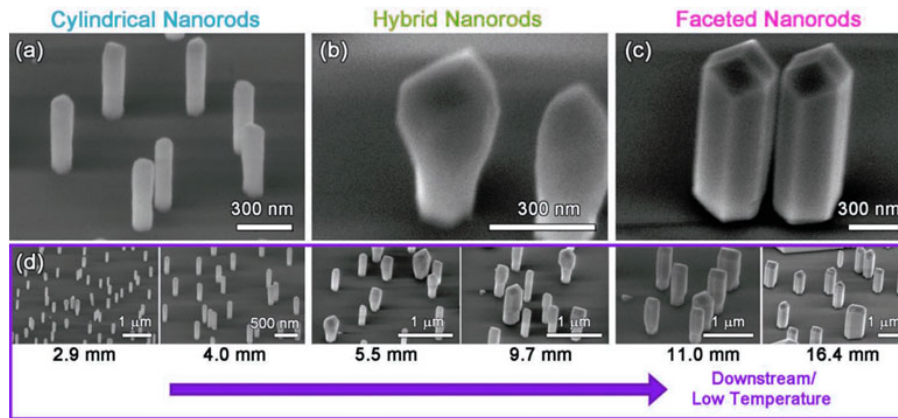
Figure 3.14: SEM images in 45° tilted view of the different nanorod morphologies as grown on the mica substrate, from cylindrical rods (a) to faceted (c), passing through the hybrid ones (b). (d) Lower magnification images taken at different distances respect to the center of the furnace, indicated below each image. Local temperature decreases with increasing distances, as it is pointed by the arrow. Figure from adapted ref. [189].

Morphological transition from cylindrical to hexagonal ZnTe NWs

In order to understand the morphological transition from cylindrical to hexagonal NWs we perform detailed structural characterizations, especially focusing our attention on the hybrid nanorods. As they contain segments of both types of wires, are the ideal candidates to find the driving force of the morphological transition. A variety of (S)TEM related techniques have been used to achieve this goal, covering spectroscopies (EELS and EDX), diffraction studies (SAED analyses) and high resolution imaging, performed in both modes, TEM and aberration-corrected STEM (HAADF).

Starting from the compositional analyses, it is important to check the actual stoichiometry and possible chemical changes in the cylindrical and hexagonal sections which could be correlated to the shape transition. This can be done by EDX or EELS techniques, acquiring spectra along the length of the hybrid nanorods, as shown in Fig. 3.15(c, d). In the figure, the NW morphology is highlighted by the surface plot displayed in (a). The 1:1 Zn:Te relationship is kept constant within the experimental error
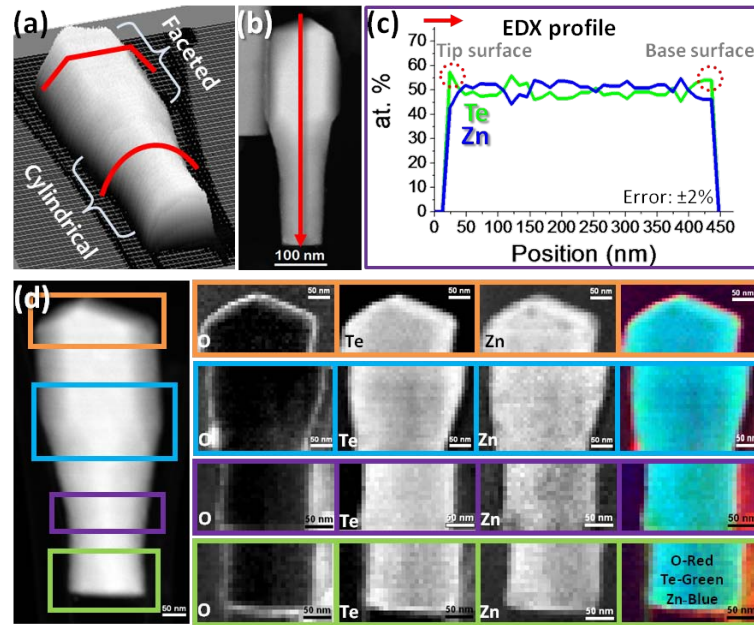
Figure 3.15: Low magnification HAADF images of one hybrid nanorod, displayed as surface plot and raster image in (a) and (b), respectively. (c) EDX profile taken along the length of one hybrid ZnTe nanorod, following the red arrow in (b).(d) O, Te and Zn EELS signals mapped at the sections indicated on the left hand image. The most right panel corresponds to the RGB composition of the O, Te and Zn signals, colored in red, green and blue.

along the entire NW, irrespectively of the cross-section shape, circular (at the base) or hexagonal (at the tip) as evidences the EDX profile plotted in Fig. 3.15(c) and taken along the entire length of the rod shown in (b). Similar results are obtained when analyzing the rods by EELS at different sections from the tip to the base, but pointing out also a slight surface oxidation. Maps of the EELS signals for the found constituents (Zn, Te and O) are included in Fig. 3.15(d) along with the colorful composition of all of them.

Interestingly, both spectroscopic techniques employed reveal a high Te content at the outer surface of the rods, linked to the presence of Te crystalline particles attached to the rod surface. In fact, the presence of such aggregates is also noticeable when analyzing individual ZnTe NWs by Raman scattering spectroscopy, as shown in Fig. 3.16(a, b) [190]. The peaks comprised in the range between -200 and 200 cm^{-1} shifts in the Raman spectra are attributed to the presence of crystalline tellurium. The further inspections performed by atomic resolution HAADF imaging verify the presence of crystalline Te particles aggregated to the NWs surface, as shown Fig. 3.16(c). The metallic Te crystals belong to the $P3_121$ space group, and they are epitaxially attached to the ZnTe ZB, as shown in the projection along the [110] zone axis of both structures.

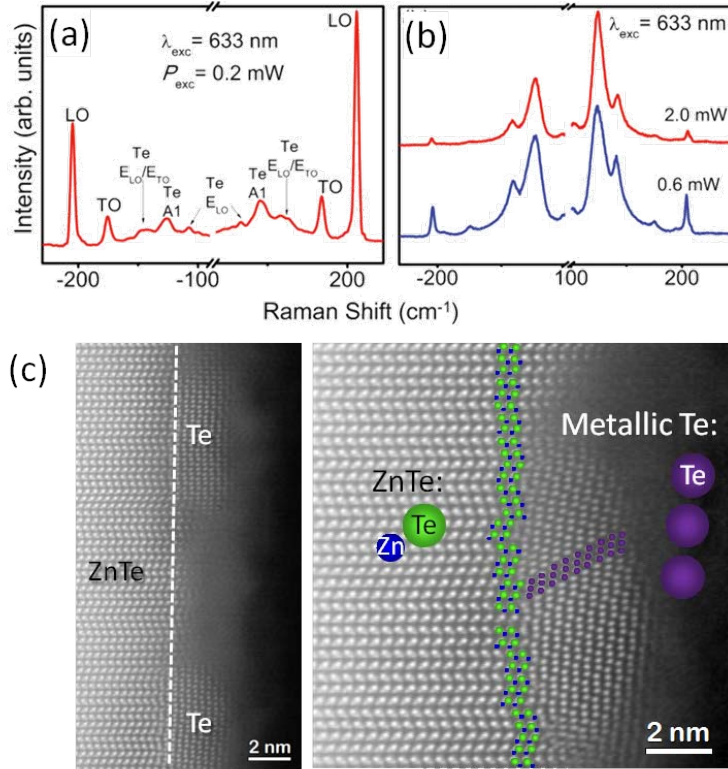So far, we have seen that the observed morphological transition as function of the

Figure 3.16: (a, b) Raman scattering spectra performed on an individual ZnTe NW, by using different laser excitation power. Modes comprised between -200 and 200 cm^{-1} shifts are due to the presence of crystalline Te aggregates [190], attached to the NW surface as shown in the atomic resolution HAADF images in (c).

local growth temperature is not related to any compositional change. However, when moving to the structural characterization of the crystalline lattice, differences appear along the hybrid nanorods. A summary of the structural characteristics can be found in Fig. 3.17. Several experiments were performed to analyze the crystallinity of the ZnTe NWs, again with remarkable emphasis on the hybrid NWs. The analyses are focused on the three main regions distinguishable in the rods: the faceted tip, the cylindrical base and the intermediate area between them, color code framed in orange, blue and green, respectively in the figure. SAED and HRTEM experiments are used to probe the crystalline properties of the wires, while atomic resolution HAADF allows the polarity assignment.

Structural differences from the faceted tip to the cylindrical base are undeniable. Paying attention to the analyses performed near the tip of the NWs, the ZnTe shows ZB structure, with occurrence of spaced twin boundaries. In the SAED pattern orange framed included in Fig. 3.17(c) two sets of ZB spots can be distinguished. By comparison of the experimental SAED pattern with the simulated ones displayed in Fig.
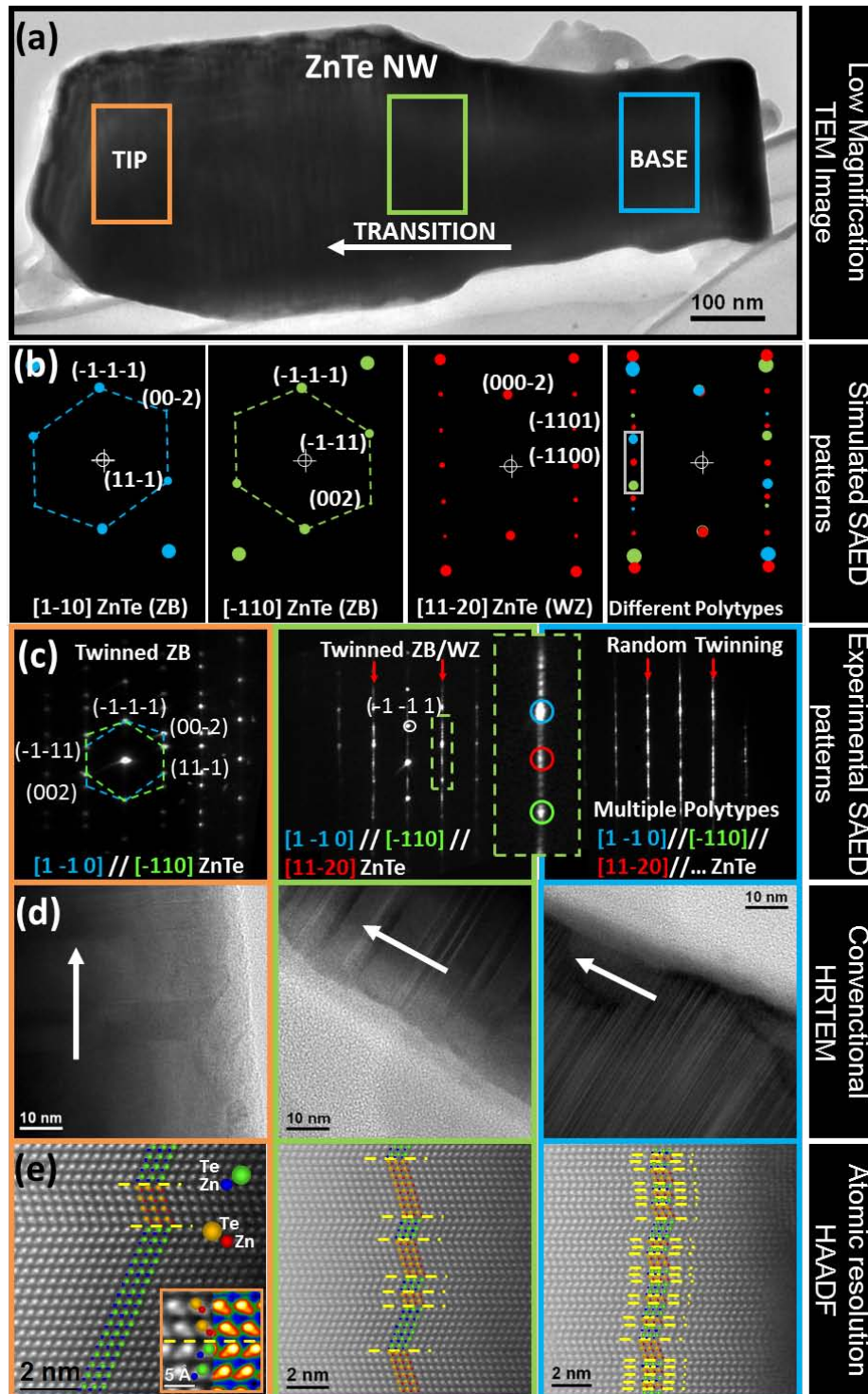
Figure 3.17: (a) Low magnification TEM image of an hybrid ZnTe NW. Colorful rectangles indicate the considered areas analyzed in (c-e): orange frame images correspond to the faceted tip, green frames belong to the transition area between the base and upper part and blue ones to the cylindrical base. (b) Simulated SAED patterns corresponding to some polytypes present in the NWs. (c) Experimental SAED patterns along the NW. (d) Conventional HRTEM at the different regions of the wire. The arrows point to the tip of the NW. (e) Atomic resolution HAADF images. Figure adapted from ref. [189].

3.17(b), the superposition of the ZB lattice under two different orientations, $[1\bar{1}0]$ and $[\bar{1}10]$, related by the presence of twin boundaries (same lattice structure rotated 180º around the growth direction) is clear. The NW tips hexagonally faceted have twinned ZB structure, growing along the $[\overline{111}]$ direction (B-polar). In agreement with the experimental SAED patterns obtained at the tip, the HRTEM images, as the one orange squared in Fig. 3.17(d), show almost pristine ZnTe ZB, with some twin boundaries perpendicular to the growth direction, easily noticeable by the contrast change at every twin (darker and brighter regions perpendicular to the growth). The typical length between twin boundaries is around 10 nm, although we can find some wider twin-free segments (with widths above 30 nm). Twins are better visualized in the HAADF image included in Fig. 3.17(e), where the dumbbells show two different orientations, depending on whether they are projected along the $[1\bar{1}0]$ or $[\bar{1}10]$ directions. Every twin plane is pointed by an horizontal yellow dashed line. Despite the presence of the twins, the ZnTe ZB at the tip grows following one Te-polar direction, i.e., $[\overline{111}]$ and the twin-free ZB regions are wider enough to allow the ZB stacking ($ABCABC...$) being completed. The $(\overline{111})$ plane is the growth plane common to both ZB orientations, and the twin boundaries are occurring along such planes.

Moving to the middle part of the NWs, analyses on the transition area between the faceted tip and cylindrical base reveal the polytypic structure of the ZnTe. There, randomly distributed twin boundaries show up, resulting in an experimental SAED pattern containing reflections from both ZB orientations, hexagonal WZ structure, and some extra aligned reflections related to other twinning periodicities. Among the simulated SAED patterns, we have included a polytypic mixture of twinned ZB and WZ, where the spot multiplicity is remarkably increased compared to the pristine structure. Reflections from these structures can be identified in the experimental data, along with many others less bright (magnified detail presented on the green dashed framed inset in Fig. 3.17(c)). Again, twin boundary locations are highlighted by yellow dashed lines in the HAADF image in (e), which also confirms the non-polar nature of the twins, allowing the polytypic structure growing along the $[\overline{111}]$ preserving the Te-polarity, as occurred at the tip.

Going to the base of the NWs, the ratio of twins is increased, inducing a clear change in the atomic plane stacking and, thus, creating ZnTe polytypic segments. As the twin spacing does not show a regular periodicity, and twins occur every few layers, any polytype might be present. The SAED pattern from this area shows an aligned line of frequencies (pointed by red arrows) due to the high spot multiplicity induced by such amount of non periodic twin boundaries.

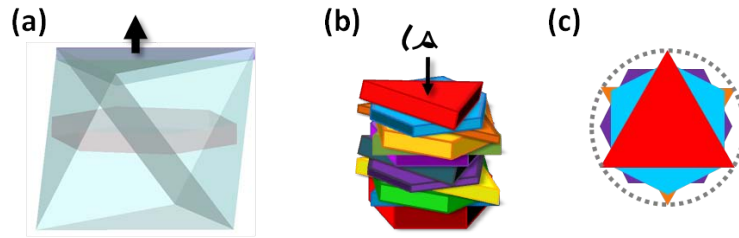Twinning occurrence on the ZnTe phase along the length of the NWs clearly changes

Figure 3.18: (a) 111 faceted octahedron, cut perpendicular to the growth axis (pointed by the arrow) at different heights, creating hexagonal (red) and triangular (purple) cross-section segments. (b) Stacking of different segments like the ones in (a) rotated respected each other as consequence of the twins. (c) View of the different shaped sections piled up perpendicular to the growth axis, resulting in an overall quasi-circular section.

from the base to the tip, allowing establishing a correlation between the morphological transformation observed from the cylindrical structures to the faceted ones from the analyses performed on the hybrid NWs. On one hand, the hexagonally faceted tips and entire NWs developed at the lower growth temperature regime follow the trend of most ZB semiconductor wires [191, 192]. On the other hand, changes in the NW faceting due to presence of twin boundaries have been reported by several authors [9, 193–196], who observed the formation of zigzag sidewalls alternating the facets orientation wherever a twin is located. Since each twin-free segment typically has a truncated octahedron morphology, eightfold faceted by {111} planes [193] (among them, six correspond to the sidewalls), the wires can be seen as an alternating series of octahedral segments stacked along the NW axis sharing the growth plane, as shown in the sketches included in Fig. 3.18. Depending on the exact placement of the twins within the octahedron, the resulting segments may have hexagonal or triangular cross-sections (including also truncated triangles) (see Fig. Fig. 3.18(a)). As the cylindrical structures appear plenty of non-periodic twin boundaries, segments of variable length and different hexagonal/triangular sections rotated by the twin effect on the lattice and piled up along the NW axis, create an overall rounded perimeter, as shown in Fig. 3.18(c).

As we have systematically observed that changes on the local substrate temperature induce the morphological transition, and that accounting for the different twin boundary densities we are able to explain the shape differences of the ZnTe NWs, it seems reasonable that the local temperature directly influences the twin formation. Indeed, the twin boundary formation has been previously reported to be thermodynamically activated, meaning that higher temperatures favor the twin formation [99, 197], in agreement with our observations. In our case, the thermodynamic barrier for the defect formation can be overcome by increasing the temperature: growth proceeding under higher local substrate temperature results in the formation of entirely cylindrical NWs induced by the huge amount of twins presented. Moving away from the center of the furnace and,

thus, reaching a lower temperature substrate area, hybrid NWs appear. Going far away enough, the temperature is even lower and the observed NWs are hexagonal prisms from the base to the tip.

The twinning density can be also related to the NW diameter [195]. For III-V NWs it is known that there is a diameter threshold above which the bigger the diameter, the larger the length of the twin-free segments. Below such diameter threshold (material dependent), other polytypes become more stable than ZB, leading to an increment in the twin density and to the WZ formation [198]. For the analyzed ZnTe NWs, this trend is maintained and the hexagonal faceted structures are wider than those cylindrical, as can be inferred from Figs. 3.14, 3.15 and 3.17.
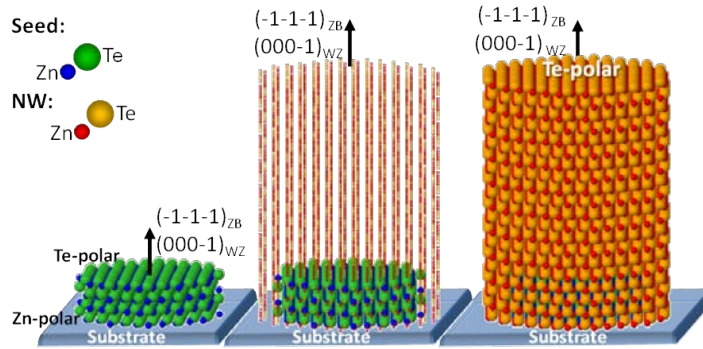

Figure 3.19: 3D atomic models showing the NW growth mechanism: a nucleation seed Te-polarized is first formed to allow the perpendicular growth of the ZnTe NWs. Atoms belonging to the initial nucleation seed are differently colored to the ones forming the remaining NW. Adaptation from ref. [189]. An animated movie of the model can be found at `http://gaen.cat/index.php/research/179`.

Before depicting the growth mechanism of the ZnTe NWs, let's emphasize the fact that no catalyst has been intentionally used during the synthesis. However, as already discussed along Section 3.2, we cannot excluded the possibility of a self-catalytic process mediating the growth. Creation of twin boundaries in III-V NWs is theoretically possible only at the triple phase line [197], supporting the hypothesis of a self-catalytic process undergoing. However, the formation of branched nanostructures, that will be discussed in next sections, is unlikely to follow a VLS process. Therefore, the question of whether the vapor-transport technique employed follows a VLS or VS growth remains unclear. Anyhow, the observed Te-polar directed growth indicates that the anionic polarity drives the unidirectional fast growth of ZnTe under the present synthesis conditions. Thus, at the nucleation stage, the forming seed should be also Te-polar to allow the further growth of the NWs. In Fig. 3.19, the nucleation seed is presented as a circular flake exposing a top $\{\overline{111}\}$ Te-polar surface, perpendicular to the substrate for the simplest cubic ZB phase. Analogously, WZ insertions with hexagonal phase show $\{000\overline{1}\}$ Te-

polar top planes. Once the nucleation seed is formed, the NW growth proceeds by vertical growing perpendicular to the substrate directed by the Te-polar NW axis.

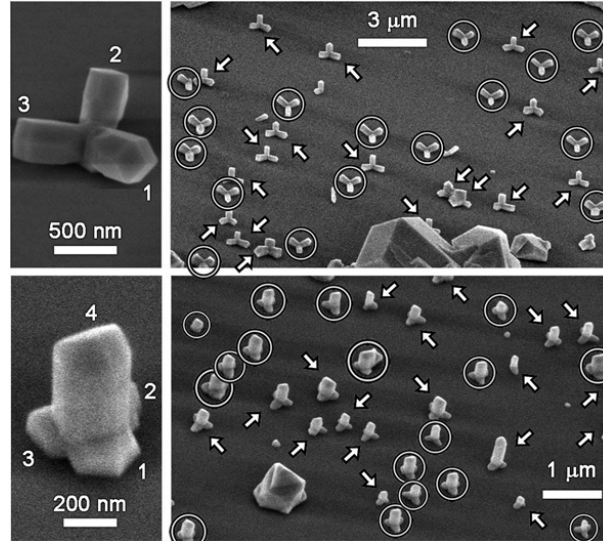**Growth mechanism of tripods and tetrapods**

Figure 3.20: SEM images of the ZnTe tripods (a, b) and tetrapods (c, d) in 45° tilted view. Note that all the tripods (b) and tetrpods (d) are aligned under two possible orientations, pointed either by arrows or by circles. Fig. adapted from [189].

Beside the growth of differently shaped NWs, epitaxial branched structures were synthesized, namely tripods and tetrapods, classified attending to the number of branches or "legs "shown. Some examples can be seen in Fig. 3.20 in 45° tilted view SEM images. Note that all the tripods and tetrapods observed are perfectly aligned with each other, as a consequence of the epitaxial relationship with the substrate. Moreover, both kinds of structures are arranged following two possible orientations, due to the three-fold symmetry of the legs. Both possible orientations are differently indicated in Fig. 3.20 (by arrows or circles). Such in-plane alignment is expected for epitaxial growth , strongly supporting the proposed van der Waals epitaxy mediating the growth. It is worth mentioning that this is the first report of epitaxial growth of tetrapods.

In order to elucidate the growth mechanism promoting the formation of the branched nanostructures, they have been studied under HRTEM and aberration-corrected HAADF techniques to get insights into their structural and polarity characteristics.

The crystal structure of one tripod near the central part of the nanostructure or core is shown in Fig. 3.21, where also two legs or ramifications are partially seen. Interestingly, the visible part of the central core crystallizes under pristine ZB structure, while

the legs show polytypic mixture with predominating existence of WZ. Evidences of the different phases shown by the core and the legs are presented as FFTs of the different parts in Fig. 3.21(b-d). Similar observations of branched nanostructures showing ZB cores and WZ-like legs have been already reported [107, 199, 200]. Despite the changes on the crystal phase between the legs and the core, they are perfectly epitaxied as follows: the legs of the tripod are attached to {111} planes of the core, creating a monocrystal nanostructure as observed when properly orienting the tripods along the $[\bar{1}0\bar{1}]_{core}||[110]_{legs}$ or $[11\bar{2}0]_{legs}$ (depending on the considered phase for the legs, ZB or WZ). The legs grow following the $\langle 0001 \rangle$ direction of the WZ phase branching the structure from the {111}B planes of the ZB core. Epitaxial relationships of the type $\{111\}\langle 101 \rangle_{core}||\{0001\}\langle 11\bar{2}0 \rangle_{legs}$ exist between the core and each leg of the tripod.
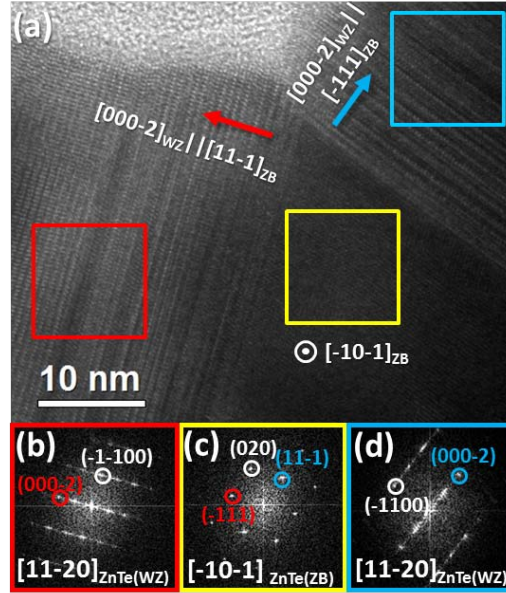

Figure 3.21: (a) HRTEM image of part of one tripod showing the ZB core and two of the polytypic legs. (b-d) FFTs obtained at different parts of the tripod: (b) left leg, (c) central core and (d) right side leg. Modifyed figure from ref. [189].

Further atomic resolution studies performed by means of STEM techniques allow for the polarity assignment on these branched nanostructures, as shown in Fig. 3.22. In this figure, an entire tripod is shown in a low magnification HAADF image (a), along with an atomic resolution image of part of the core and two adjacent legs (b). Magnified details of the leg structure are also presented (c,d) evidencing their Te-polar growth, as expected by similarities with the NWs.

The proposed growth mechanism might start by the formation of a nucleation seed of pure ZB structure. Such seed would be octahedrally limited by {111} planes that
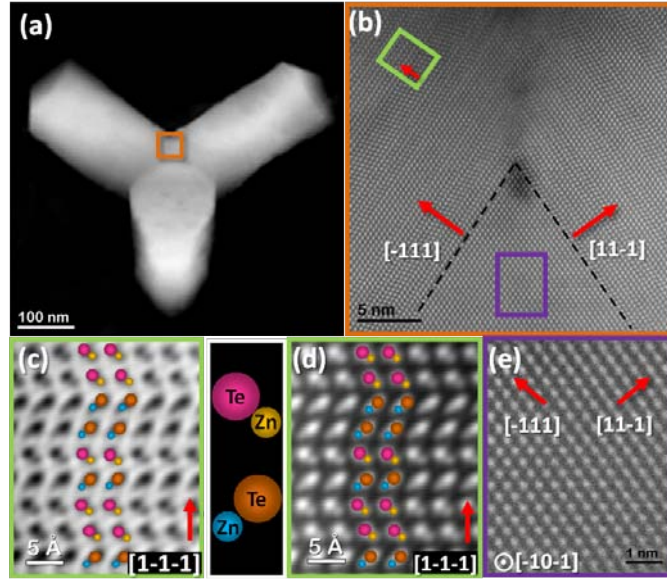
Figure 3.22: (a) Low magnification HAADF image of one entire tripod. (b) Atomic resolution HAADF image partially showing the tripod core and two legs. (c/d) Atomic resolution ABF/HAADF image of the structure at the region green framed in (b), showing the Te-polar growth direction. (e) Atomic resolution HAADF image of the ZB core. Fig. adapted from ref. [189]

will become the body of the tripod. Due to the lattice geometry, half of exposed {111} planes by the seed will be Te-polarized, i.e., $(\bar{1}\bar{1}\bar{1})$, $(11\bar{1})$, $(1\bar{1}1)$ and $(\bar{1}11)$, and the other half Zn-polarized, i.e., (111), $(\bar{1}\bar{1}1)$, $(\bar{1}1\bar{1})$ and $(1\bar{1}\bar{1})$. In order to allow the tripod formation with 3 legs 19.5º upwards the substrate as experimentally observed, the nucleation seed should be necessarily Zn-polar, meaning that shows one of the Zn-polar surfaces on the top while one Te-polar {111} facet is in contact with the substrate, leading to three equivalent {111}-Te directions free, along which the legs of the tripod may grow, forming a projected angle of 120º between adjacent legs. All the explained features are easily seen in Fig. 3.23, where a 3D atomic model of the tripod is presented along with two different views: lateral (a-c) showing the growth outwards the substrate and top view (d-e) where the tripod is projected normal to the substrate.

Once understood the tripod formation, it is straightforward assuming that the same nucleation seed turned upside down (and thus, with the Zn-terminated surface touching the substrate and with one Te-polar on the top), would lead to the formation tetrapods by further growth of the material on the 4 available Te-polar surfaces (Fig. 3.24(a,b)). However, such configuration would correspond to the creation of tetrapods with one leg perpendicular to the substrate, which are not observed experimentally, as shown in Fig. 3.24(c). In fact, all the tetrapods found show one tilted leg growing upwards, suggesting that the growth must not be initiated by a single octahedral seed. Instead, the experimental situation can be successfully explained by considering multiple-order-twinning
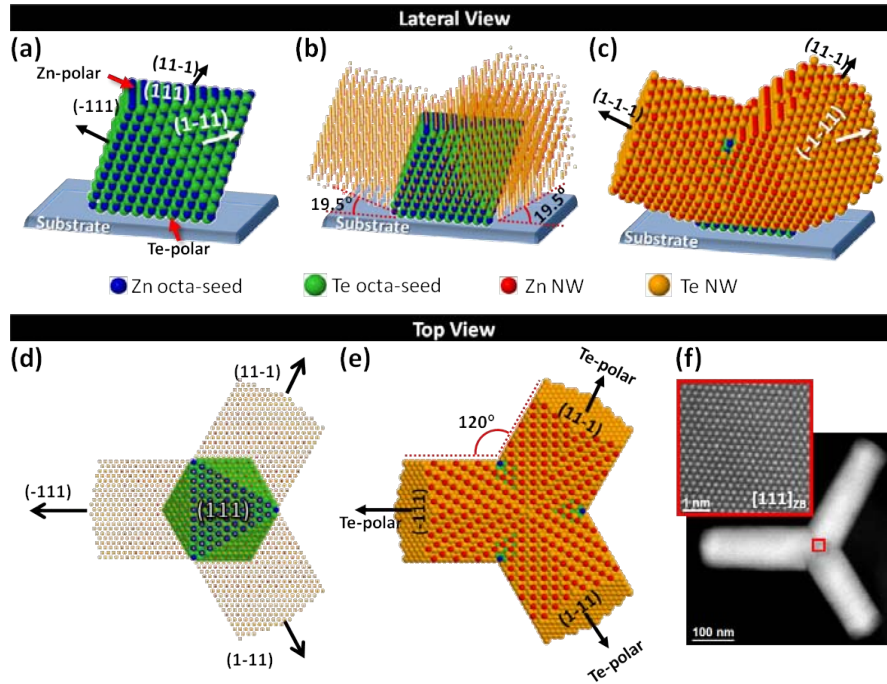
Figure 3.23: Lateral (a-c) and top (d-f) views of the of the tripod atomic 3D model. The Zn-polarized octahedral nucleation seed (a) allows the growth of the legs on the 3 {111} Te-polar facets exposed. Such planes are 19.5° upward from the substrate (b,c), while forming an angle of 120° among them in projection (d,e). An experimental image of the tripod top view along the [111] zone axis is included in (f). Adapted from [189]. An animated movie of the model can be found at `http://gaen.cat/index.php/research/179`.

at the nucleation seeds, similar to the case of tilted GaAs NWs where the growth was initiated after three-dimensional twinning at the seed [201]. Second order seeds can be created on one facet of the initial octahedral seed by the occurrence of a twin, while first order seeds will be in interfacing the underlaying substrate. From SEM observations we found out that at the first growth stages of the tetrapods, the nucleation seeds shown a truncated octahedral morphology. Since the muscovite mica substrate employed is non-polar, orientations other than the $\{111\}_{ZB}$ can be expected, allowing the development of the observed shape of the seeds. Moreover, it is easily noticeable that the tetrapods can be classified into at least two different groups attending to the number of legs interfacing the substrate, differently encircled in red and blue in the SEM image included in Fig. 3.24(c). This fact can be correlated with the different family planes truncating the octahedron and being themselves the basal planes of the first order seeds in contact with the substrate.

The creation of 3D atomic models under the previous assumptions allows us to comprehensively explain the tetrapod growth mechanism for the two observed orientations,
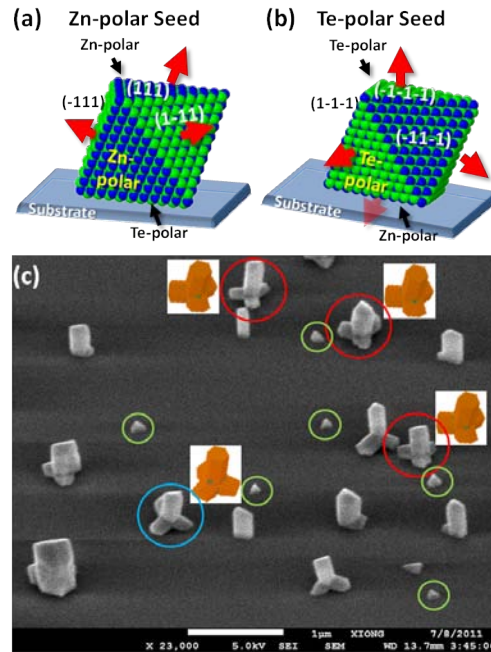
Figure 3.24: 3D atomic models of the Zn-polar (a) and Te-polar (b) ZnTe octahedral nucleation seeds. Seed in (a) leads to the formation of tripods by further growth along the available Te-facets, pointed by red arrows. Turning the same seed upside down, tetrapods with one leg (upwards) perpendicular to the substrate should be created. (c) SEM image of the tetrapods in a 45° tilted view. Two kinds of tetrapods, encircled in red and blue, can be observed attending to the number of legs inferring the substrate. Truncated octahedral seeds are green circled. Fig. adapted from ref. [189].

labeled in the following as type 1 and type 2 (red and blue encircled respectively in Fig. 3.24(c)). In the case of type 1 tetrapods, the first order seed must be cut by a (101) plane, interfacing the substrate and showing {111} faceting to create the truncated octahedron shape (see Fig. 3.25(a)). Then, the occurrence of a twin boundary on one of the facets will allow the formation of an entire octahedron attached to the former, creating the second-order seed. Such seed would have 4 Te-polar {111} facets along which the tetrapod can grow. Among these 4 Te-polar planes one will be the shared facet with the first order seed which eventually become the tetrapod leg interfacing the substrate.

Regarding the type 2 tetrapods, the situation is pretty similar, but starting by the formation of a first order seed truncated by a (121) plane in contact with the substrate (see Fig. 3.25(b)). Again, twinning occurrence on one of the {111} seed facets let the formation of a complete octahedron (second order seed) which can evolve to the creation of a tetrapod along the Te-polar fast growth directions exposed by the second order seed. Due to the orientation of the first order seed, the resulting tetrapod will have two legs interfacing the substrate in contrast to type 1 tetrapods.
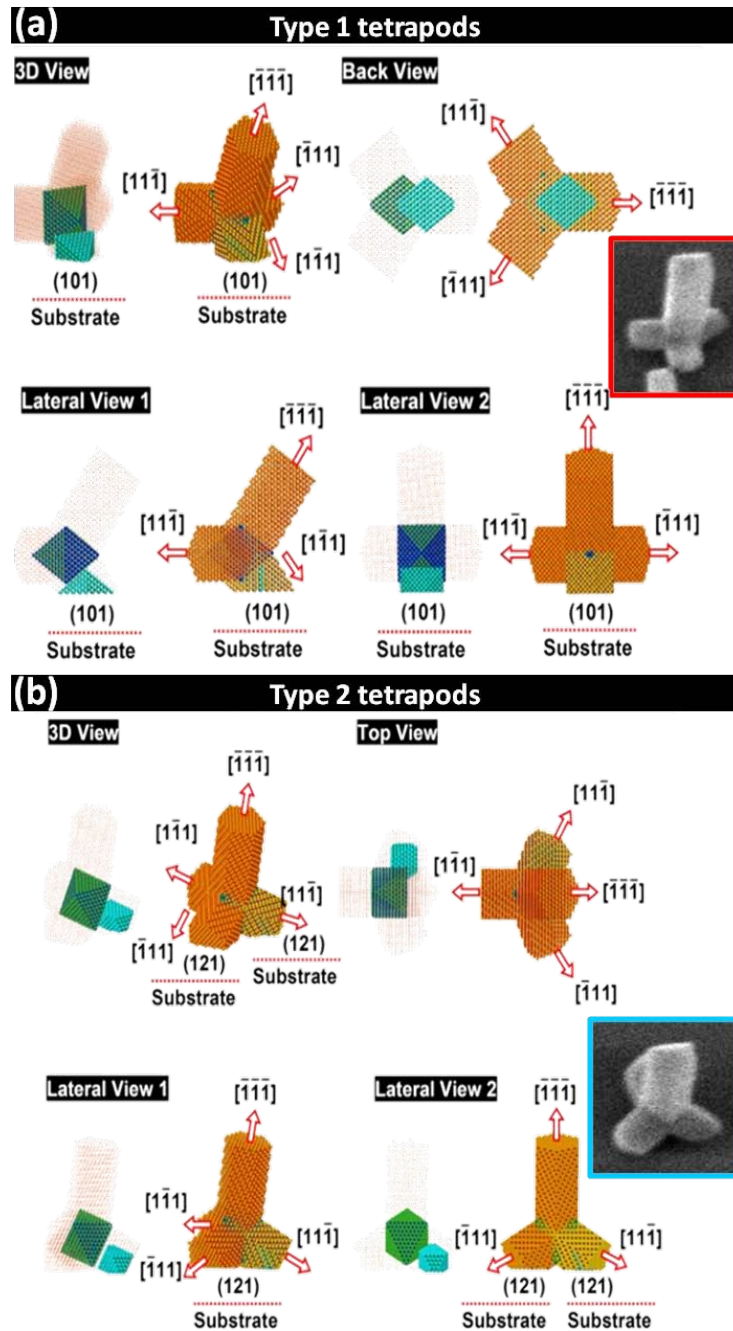
Figure 3.25: (a) 3D atomic model under different views, depicting the growth mechanism of the type 1 tetrapods. First and second order seeds are differently colored to ease the description on the text. (b) Same as (a) but for the type 2 tetrapods. Right side insets displayed type 1 (red framed) and 2 (blue framed) images of the tetrapods. Adapted from ref. [189]. An animated movie of the model can be found at `http://gaen.cat/index.php/research/179`.

Further examples on NWs and tripods formation: the GaN case

Similar to the ZnTe case concerned in the previous sections, other materials can grow under a variety of morphologies. Driven by the most stable polarity under the growth conditions employed, formation of NWs and tripods of different materials can be explained based on similar models to the one proposed above [107, 199, 200, 202].

As extensively discussed on section 3.2.2, GaN directed growth with opposite polar directions, i.e. [0001] and [000$\bar{1}$], can be achieved under different experimental conditions. In the case of Ga-polar propitious growth conditions, we have recently reported the formation of GaN NWs, tripods and nanotubes [108]. The growth procedure employed rely on the SAG growth on diamond properly masked by a Ti layer. Interestingly, by playing around with the experimental parameters, i.e., the size and distribution of the pitches, we can tune the growing structures from NWs to nanotubes. In addition, the growth of tripods can be successfully suppressed by increasing the substrate temperature.

We observe the NWs formation within a temperature window between 810 and 890°C. However, for the lower temperatures tried, the NWs grow on the mask and on the patterned positions at similar rates. In order to reach the desirable selectivity, the substrate temperature has to be increased until 830°C, which represents the lower temperature limit for the GaN SAG on a Ti mask. When analyzing the as grown structures at the intermediate temperature regime studied, we observed the formation of tripods along with the NWs. Again, the resulting tripods are perfectly oriented along two opposite directions, as shown in Fig. 3.26(a, b).

As usually observed, since the unidirectional growth is favored for a certain polarity, NWs and tripods necessarily grow from oppositely polarized nucleation seeds. As previously commented, the SAG procedure here employed favors the elongated growth along Ga-polar directions. In agreement, the polarity study performed on a FIB lamela containing the epitaxed GaN NWs on the diamond substrate, by means of ABF, reveals that the wires crystallize in WZ structure and grow along the Ga-polar [0001] direction. However, the non-polar substrate used, does not prevent nucleation events under both polarities, if choosing the right growth conditions. Thus, whenever the nucleation takes place by the formation of a Ga-polar nuclei, the growing structure will evolve to create a NW perpendicular to the substrate Fig. 3.26(f-h). But, if the forming nuclei exhibits N-polarity, a tripod will be developed instead Fig. 3.26(c-e). We also observe the same polytypic behavior reported for other materials tripods, meaning that the core of the tripods is purely ZB while the legs are WZ. As usually in WZ or highly hexagonal polytypes, the legs grow along one ⟨0001⟩, which in agreement with the growing NWs side
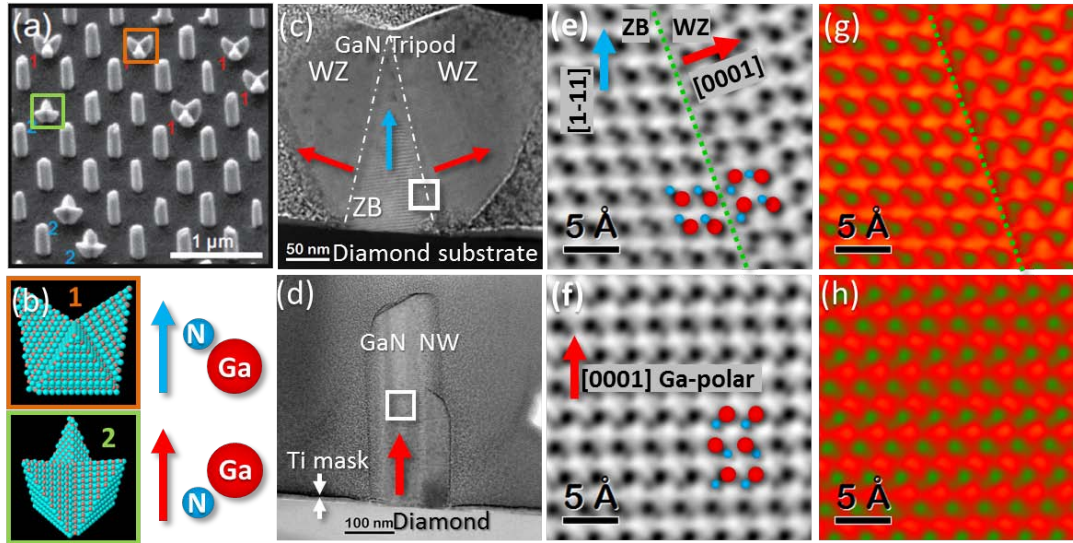
Figure 3.26: . (a) SEM image of the as grown GaN tripods and NWs at 870°C. The two tripod rotation domains are indicated by 1 (orange) and 2 (green). 3D atomic models of the two tripod orientation are included in (b). (c/d) GaN Tripod/NW on the diamond substrate. The colorful arrows follow the code indicated at the upper part of the figure (blue points N-polar direction while red indicates Ga-polar growth). (e/f) ABF images of the atomic structures at the regions white squared in (c/d), respectively. ZB N-polar tripod core and Ga-polar legs and NWs are clearly visible. (g/h) Same images as (e/f) false colored to enhance the N presence. Adapted from ref. [108].

by side to the tripods, follow the Ga-polar option, the [000+1]. The nucleation seeds of the tripods eventually creating the cores are identified as ZB when aligning along the [110] or [11$\bar{2}$0], growing along the N-polar [1$\bar{1}$1]. Lateral twinning on other {111} planes allows the development of the WZ, Ga-polarized.

For a substrate temperature of 890°C, the tripod formation is suppressed (presumably by the reduced possibility of a N-polar seed to nucleate under higher temperatures), and the growth of perpendicular NW arrays with a 100% occupation hole yield is achieved, with successful annihilation of the parasitic growth on the mask surface.

As well as different substrate temperatures, other experimental parameters were systematically modified in order to address their influence on the growth. For instance, by modifying the III/V ratio it was found that the growth is N-limited, even if using N-rich conditions, in agreement with refs. [48, 160, 161]. As a proof of fact, the NW length and diameter are found to increase with the N flux although Ga might be expected to act as limiting reactant. Therefore, the axial and radial growth are N-limited, attributed to the different diffusion behavior of the Ga and N species: while the Ga diffuses on the mask and NW sidewalls, the N is only incorporated where impinges. Otherwise, N radicals easily create N_2 molecules, not contributing the NW growth.
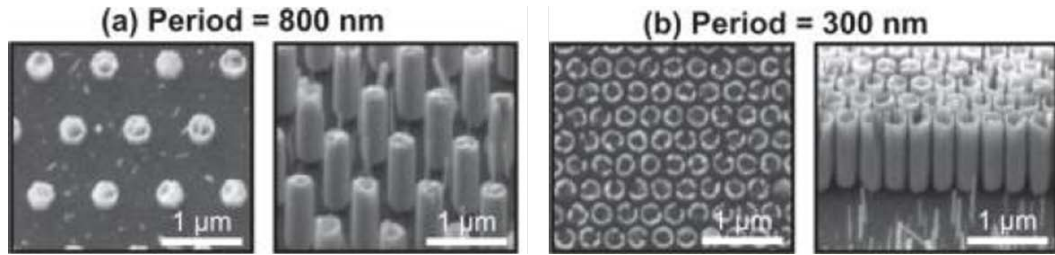
Figure 3.27: SEM images of the GaN nanotubes grown on Ti patterned mask with periods (distance between consecutive patterned holes) of 800 nm (a) and 300 nm (b).

In addition to study the influence of the global III/V ratio, we account for the local one by modifying the mask design, which will affect the Ga diffusion. The period between patterned holes on the mask was varied from 300 to 5000 nm, keeping the growth temperature in all the cases (890ºC). Selectivity was achieved irrespectively of the pattern period, but for the closer holes patterned, inhomogeneities at the top facets appear, indicative of proximity effects. The resulting structures growing under these conditions are hollow tubes instead of solid NWs, as shown in Fig. 3.27. Analyzing the length and diameter of two sets of samples growing at different N pressures, in front of the hole period, reveals that there is a growth saturation at the high periods in both parameters measured, irrespectively of the N flux (Fig. 3.28(a,b)). For the shorter periods, however, there is a drop of the growth when decreasing the distance between holes, associated to a competition for the diffuse Ga adatoms between neighbor NWs. It is found out that especially the incubation time and initial growth stages are affected by the local III/V ratio.

The Ga collection area can be considered as a circle of radius l_{Ga} (Ga diffusion length on the mask), around the hole. If the hole period is smaller than twice l_{Ga}, the collection area saturates inducing the competition for the arriving Ga adatoms. Similar observations of competitive growth regime as function of the inter-hole distance in SAG procedure are reported elsewhere [187]. This effect is illustrated in Fig. 3.28(c). The design of masks with patterned holes displayed in small periods and with large sizes allows inducing a highly competitive growth regime. Vertical nanostructure arrays are obtained when using 100 nm holes with 300 and 800 nm periods. While the larger period used allows the formation of the expected NWs, the smaller hole spacing drives to the formation of nanotubes instead, due to an increasing overlap of the Ga collection area when reducing the period. As-grown nanotubes on the substrates for holes with periods of 800 and 300 nm are shown in Fig. 3.27(a) and (b), respectively. Different hole diameters are explored at the smaller period pattern, allowing tailoring the growth from NWs to hollow nanotubes. If the mask design induce small Ga collection areas,
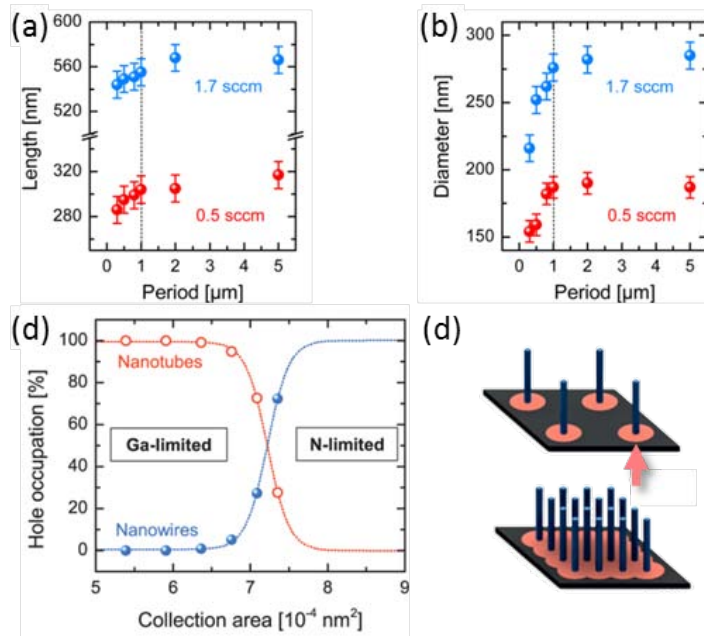
Figure 3.28: Length (a) and diameter (b) dependence on the mask period for two different N fluxes. Saturation is reached above 1 μm, corresponding to a 500 nm l_{Ga}. (c) Sketches representing the NW formation when Ga collection areas are apart from each other (top), while their overlapping induce the formation of nanotubes (bottom). (d) % of the holes on the mask occupied by NWs (blue curve) or nanotubes (red curve) as function of the Ga collection area. Fig. adapted from ref. [108]

100% yield of nanotubes is achieved, but larger Ga collection areas lead to the formation of NWs occupying 100% of the patterned holes, as shown in Fig. 3.28(d). A continuous transition from one to the other is identified, due to the change from N-limited to Ga-limited growth conditions achieved by a rational tailoring of the patterned masks.

In this way, the SAG is a versatile tool for the growth of a variety of GaN nanostructures with excellent crystallinity; which shape, distribution and size can be highly controlled through experimental parameters. The influence of the mask design on the Ga diffusion length is probed, and by rational tailoring of the hole distribution, the formation of regular GaN nanotubes arrays by SAG could be achieved, to the best of our knowledge for the first time.

3.4   Conclusions

Atomic resolution STEM techniques allow the direct and straightforward polarity iden-
tification in binary nanostructures. Combining both, HAADF and ABF techniques
simultaneously, we established a tandem methodology to distinguish the dumbbell con-
stituents in binary semiconductors. HAADF is highly useful for medium and high
atomic number constituents, but it fails for light elements (especially if they are to-
gether with heavier ones). While HAADF signal is Z-dependent resulting in atomic
chemical contrast, the simultaneous acquisition of the ABF signal permits the dumb-
bell recognition for oxides and nitrides by comparing with the HAADF, where only the
heavier constituent is visible. Trying to shed light over the unidirectional polar growth
at the nanoscale, we employ such methodology to determine the polarity in the most
commonly synthesized and used III-V and II-VI NWs. Despite of finding that the vast
majority of the wires follow anionic-polar directions, the observation of materials with
ambipolar behavior can not be neglected (e.g., GaN, InP, ZnO).

Different material intrinsic parameters have been compared in the search for a
rule describing the polarity preference during the growth of non-planar nanostructures.
Among the checked properties, we analyze the radii ratio of the compound constituents,
accounting for the ionic, atomic and covalent radii of the species involved. We also
evaluate the compound ionicity by considering two different definitions, Pauling's and
Phillips'. Unfortunately, we could not find a direct connection among those ratios and
the preferential polar growth, although the covalent radii relationship follows a suitable
trend, but not explaining all the cases. Similarly, the ionicity inspections do not directly
correlate the compound ionicity with the observed polar growth, and we only could no-
tice that those compounds with the higher electronegativity difference are prone to show
ambipolar behaviours (i.e., they have been reported to grow under both polarities).

Nevertheless, it is noteworthy that in those systems, the growth procedures leading
to opposed polar growths are governed by different thermodynamics and/or kinetics.
Thus, we took an overview of the extrinsic parameters tunable during the growth and
how do they influence the polar growth at the nanoscale. Comparing our experimental
results with the reports in the literature, it is likely the local conditions on the vicinity
of the growing event strongly influence the resulting structure, and they may differ from
the overall input conditions, hampering more the understanding.

In addition, the preferred polar growth found for different materials growing under
a variety of conditions, allow the understanding of their formation. In this context,
we depict the formation mechanisms for several nanostructures, going from nanorods
(with different cross-sections, i.e., circular or hexagonal) to tetrapods by passing through

tripods. Polytypism, twinning and polarity are the key parameters to understand their growth.